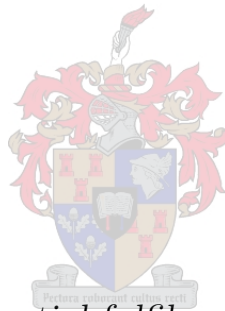# Beamforming Techniques for a Quad-Mode Antenna Array

by

Geomarr van Tonder

Thesis presented in partial fulfilment of the requirements for the degree of Master of Engineering in the Faculty of Engineering at Stellenbosch University

Supervisor: Prof P. Meyer

March 2017

Declaration

By submitting this thesis electronically, I declare that the entirety of the work contained therein is my own, original work, that I am the sole author thereof (save to the extent explicitly otherwise stated), that reproduction and publication thereof by Stellenbosch University will not infringe any third party rights and that I have not previously in its entirety or in part submitted it for obtaining any qualification.

Date: . . . . March 2017 . . . .

Signature: . . . .
G. van Tonder

Abstract

Beamforming Techniques for a Quad-Mode Antenna Array

G. van Tonder

Department of Electrical and Electronic Engineering,
University of Stellenbosch,
Private Bag X1, Matieland 7602, South Africa.

Thesis: MEng (Electronic)

March 2017

This thesis is based on a quad-mode antenna, designed by a group of researchers from the University of Stellenbosch. The antenna is designed using two co-located dipoles and a cylindrical monopole antenna folded back towards the ground plane. By exciting each dipole arm with a quadraxial feed line, four fundamental transverse electromagnetic propagating modes, also known as multi-modes, are observed. Using array theory and combining the multi-mode response, a unique radiation pattern is observed. Further research expands into effectively obtaining a combinational response which illustrates characteristics of an isotropic radiator. This is accomplished by using optimization techniques such as the genetic algorithm and the Nelder-Mead simplex algorithm.

The four fundamental multi-modes can be fully characterized by their equivalent single-ended mode excitations. A network terminated with single-ended excitations is obtained through a linear combination of the multi-mode excitations by implementing the generalized scattering matrix transformation technique. The focus of the thesis shifts towards the design of a feed network using this set of optimal excitations. Initially the feed network is designed in ADS Agilent. From there it is integrated into the quad-mode antenna design and simulated using CST Microwave Studio®.

Research further extended into the field of beamforming by placing the quad-mode antenna in a 2×2 array configuration with an interelement spacing of a half-wavelength. Using the embedded element pattern, which includes the active reflection coefficient, the array's beam pattern is steered towards a desired observation point. This is achieved by solving the maximum-gain beamforming theorem and conjugate field matching condition. The maximum gain over a hemispheric field-of-view coverage is configured, and an overall gain variation of 2.7 dBi is obtained. Furthermore, by optimizing this set of multi-mode response patterns in an array configuration, a set of multi-mode excitations are obtained with a maximum gain variation over the hemisphere of 2.3 dBi, when simulated using the embedded element pattern.

Uittreksel

Bundelvorming Tegniek vir 'n Multimodale Antenna Samestelling

G. van Tonder

Departement Elektriese en Elektroniese Ingenieurswese,
Universiteit van Stellenbosch,
Privaatsak X1, Matieland 7602, Suid Afrika.

Tesis: MIng (Elektroniese)

Maart 2017

Hierdie tesis is gebaseer op 'n multimodus antenna ontwerp, deur 'n groep navorsers van die Universiteit van Stellenbosch. Die antenna is ontwerp met twee mede-geleë dipole en 'n silindriese monopool antenna, wat terug na die grond vlak gevou is. Deur elke dipool arm aan te dryf met 'n kwadraksiale voerlyn word vier fundamentele ortogonale elektromagnetiese modus, ook bekend as multimodus waargeneem. 'n Unieke stralingspatroon word waargeneem deur die verskeie multimodus reaksies te kombineer. Navorsing is verder uitgebrei om 'n stralingspatroon met isotropiese kenmerke te verkry. Dit word gedoen deur die gebruik van optimeringstegnieke soos die genetiese algoritme en die Nelder-Mead simpleks algoritme.

Die vier fundamentele multimodusse kan ten volle gekenmerk word deur hul ekwivalente enkel geëindigde opwekking. 'n Netwerk, met enkele terminasies word verkry deur die lineêre kombinasie van die multimodusse opwekkings deur gebruik te maak van die algemene verstrooiing matriks transformasie tegniek. Die fokus van die proefskrif skuif na die ontwerp van 'n voernetwerk wat gebruik maak van 'n stel optimale opwekkings as die uitset metode. Die voernetwerk is ontwerp en geïntegreer in die multimodus antenna in ADS Agilent en gesimuleer met behulp van CST Microwave Studio®.

Verdere ondersoek word in werking gestel om die antenna in 'n 2×2 samestelling te plaas met 'n spasiëring van 'n half-golflengte. Die skikking se bundel patroon word gestuur na 'n gewenste waarnemingspunt met behulp van die ingeboude elementpatroon, wat die aktiewe weerkaatskoëffisiënt insluit. Dit word bereik deur die oplossing van beide die maksimum-aanwins bundelvorming stelling en die toegevoegde veldaanpassing voorwaarde. Die maksimum aanwins oor 'n hemisferiese dekking is ingestel in 'n skikking, en 'n wins variasie van 2.7 dBi word uitgebeeld. Verder, deur die optimering van hierdie stel multimodus patrone in 'n skikking word 'n stel multimodus opwekkings verkry met 'n maksimum aanwins variasie oor die halfrond van 2.3 dBi, gesimuleer met behulp van die ingeboude elementpatroon.

Acknowledgements

I would like to express my sincere gratitude to the following people.

- My supervisor, Prof Petrie Meyer, for his advice and guidance throughout the duration of my Master. I would like to express my appreciation for his support, encouragement and diligence throughout my thesis. I have learned allot during the term of my studies and will forever be grateful for the opportunity he gave me.

- Prof David B. Davidson, thank you for providing the funding for this project.

- Dr. Jacki Gilmore, for providing me advice on dense aperture array beamforming implementation.

- Dr. David S. Prinsloo, for advising me throughout this project on the quad-mode antenna.

- My friends and colleagues for their advice and support throughout the project.

- My cousins, Marietjie Geldenhuys, Amanda Marais and Jay-Dee Geldenhuys, for their love and support.

- My parents, Jacques and Naomi van Tonder, for their unconditional love and support throughout the execution of this project.

- My sister, Vereesé van Tonder, my right-hand woman for whom I have great respect and admiration. I am grateful to her for thoroughly reading through my Masters. Also want to thank her for advising and guiding me during the execution of this project.

- Wim G. C. Temmerman, for encouraging me, guiding me and believing in me in my time of need. Further, I am grateful for his assistance in proofreading my thesis.

Dedications

I dedicate this thesis to my parents, Jacques and Naomi van Tonder.

Contents

CONTENTS   vii

List of Figures

List of Tables

Nomenclature

Acronyms

SKA	Square Kilometre Array
LNA	Low Noise Amplifier
AA	Aperature Array
LOFAR	LOw Frequency ARray
MWA	Murchison Widefield Array
LWA	Long Wavelength Array
SKALA	SKA Log-periodic Antenna
FoV	Field of view
TEM	Transverse ElectroMagnetic
FR-4	Dielectric substrate
EMBRACE	Electronic Multi Beam Radio Astronomy Concept
GA	Genetic Algorithm
MM_n	Multi-Mode radiation pattern
SE_n	Single-Ended mode radiation pattern

Constants

$$c = 2.998 \quad [\text{m/s}]$$
$$\pi = 3.141592654$$
$$\mu_0 = 4\pi \times 10^{-7} \quad [\text{henry/m}]$$
$$\epsilon_0 = 8.854 \times 10^{-12} \quad [\text{farad/m}]$$

Notations

G	Gain
G^R	Realized Gain
AF	Array factor
d	Interelement spacing
D	Directivity
$\mathbf{F}$	Electric field
$\mathbf{W}_0$	Power density
ϵ_0	Permittivity of free-space
μ_0	Permeability of free-space
ω	Angular frequency

r	Radius
e_{cd}	Antenna radiation efficiency
e_0	Total efficiency of an antenna
e_r	The reflection, mismatch efficiency of an antenna
e_c	Conduction efficiency
e_d	dielectric efficiency
f	Frequency
h	Height
k_0	Propagation constant of free-space
ℓ	Length
n	Element index
N	Number of elements
N_{acc}	Number of accumulations
P_{in}	Input Power
P_{rad}	Radiated Power
$\mathbf{S}^{mm}$	Multi-mode network scattering matrix
$\mathbf{S}^{se}$	Single-ended network scattering matrix
U	Radiation Intensity
$\mathbf{w}$	Weight vector
$\mathbf{I}$	Identity matrix
x	Rectangular coordinate
y	Rectangular coordinate
z	Rectangular coordinate
β_y	Phase
β_x	Phase
θ	Theta
ϕ	Phi
λ	Wavelength
Ω	Solid angle
Γ	Reflection coefficient
^{H}	Hermitian transpose
*	Complex conjugate
ϵ_r	Relative permittivity
ϵ_{eff}	Effective dielectric constant
W	Width
β	Propagation constant
v_p	Phase velocity
t	Thickness
Z_0	Characteristic impedance
C	Capacitance
L	Inductance

Z	Impedance
$S_{m,n}$	Scattering parameters of the m, n^{th} port
P_n	Power at n-port
V_n	Voltage at n-port
I_n	Current at n-port
Z_n	Impedance at n-port
k_p	Power ratio
E_ℓ	Electric length
a	Incident power wave
b	Reflected power wave
P_L	Power deliver to the load
$\mathbf{M}$	Transformation matrix
G^A	Gain of the array
U^A	Radiation intensity of the array
P_{in}^A	Input power of the array
F_{itness}	Fitness value
v	Beamformer output singal

Chapter 1

Introduction

1.1   Background

Since the first radio waves were discovered by Karl Jansky, astronomers have been using radio telescopes to explore the universe. As radio astronomers keep pushing observational capabilities, new state-of-the-art technology is being developed. At the moment, the Square Kilometre Array (SKA) is at the forefront of the latest technologies helping radio astronomers discover more about the universe. The SKA will be a distributed interferometer array, with a collecting area of a square kilometre. Thousands of dishes and millions of antenna elements will be placed around Africa and Australia. Three uniquely designed telescopes will be constructed in order to cover a radio frequency range of 50 MHz up to 20 GHz. The project is split into two development phases.

Phase one includes the high frequency dish arrays, such as the Meer-Karoo Array Telescope (MeerKAT) situated in South Africa and the Australian SKA Pathfinder (ASKAP). Phase two will use advanced technologies such as wide band aperture arrays for both the low- and mid-frequency bands. Phased array antennas are referred to as aperture arrays in radio astronomy. The lower and mid-frequency bands will consist of sparse and dense aperture arrays respectively.

Electronic beamforming techniques will effectively allow these fixed closely spaced antenna elements to survey the sky. Beamforming is achieved by delaying a signal of each individual element and then summing their output to form a coherent beam in a specific direction. This is an attractive solution to the challenge posed by mechanically moving the element when observing at lower frequencies. Institutions worldwide are demonstrating the viability of aperture array technology. An example of this is the tapered slot Vivaldi antenna, developed by ASTRON in the Netherlands, for the Electronic Multi Beam Radio Astronomy Concept (EMBRACE) pathfinder for the SKA, in Figure 1.1. The Vivaldi antenna is excited through a microstrip to slot line, acting as a balun feed. Furthermore, other successful demonstrators of sparse aperture arrays include the LOw Frequency ARray (LOFAR), Long Wavelength Array (LWA), Murchison Widefield Array (MWA), and the more recent Aperture Array Verification System 0.5 (AAVS 0.5). LOFAR, a well known demonstrator for the SKA constructed in northern Netherlands and across Europe, employs the concept of electronically steering an omnidirectional antenna array. LOFAR consists of two stations: one which covers a frequency range of 10 MHz to 90 MHz consisting of 48 densely spaced Low Band Antenna (LBA) elements and the other station that covers a frequency range of 110 MHz to 270 MHz consisting of 96 sparsely placed High Band Antenna (HBA) elements. Figure 1.2 shows the LOFAR
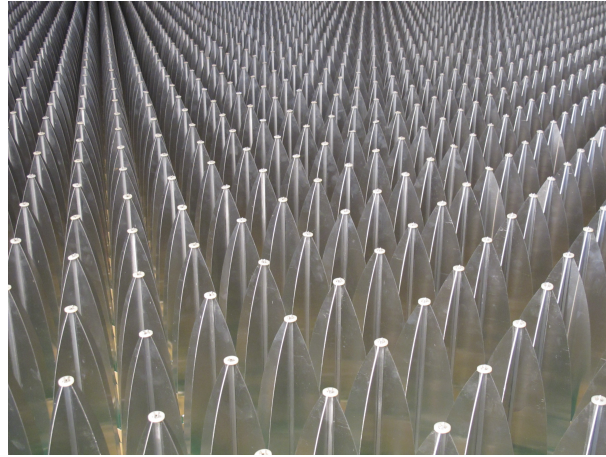
Figure 1.1: The EMBRACE aperture array.

Figure 1.2: LOFAR station at Onsala Space Observatory in Sweden[1].

station at Onsala Space observatory. The LWA antenna consists of two co-located dipole antennas. The antennas are fed by an active balun that converts the balanced dipole to an unbalanced 50 Ω impedance which is connected to a coaxial transmission line. Due to these precursor arrays having differentially fed antenna elements, a balun is used to convert differential signals at the antenna's feed to unbalanced signals, which add noise. Antennas with hemispherical FoV coverage and good polarimetric performance in broadside are of great importance to the large multi radio telescope project, the SKA. The combination of high-speed sky coverage and a large FoV, with a scanned angle of 60° from zenith, will allow astronomers to observe large areas of the sky at once, thereby making it the fastest radio telescope in its class. Current aperture array demonstrators illustrate a scanned angle of ±45° from zenith, which does not satisfy the SKA specification of 60° from zenith.

A group of researchers from the University of Stellenbosch has realized an antenna that demonstrates a broad hemispherical FoV coverage. The researchers developed the quad-mode antenna presented in [5].

The quad-mode antenna consists of two orthogonal dipoles and a ground shield folded back into a monopole element. The four dipole arms are fed by a quadraxial transmission line. The quad-mode antenna utilises all four of the Transverse ElectroMagnetic (TEM) modes, also known as multi-mode excitations present in a quadraxial feed. The propagation on this transmission line can be described by an infinite number of multi-mode sets. By varying the combinational set of complex beamforming weights a different beam pattern is illustrated by the antenna every time.

To fully characterize the multi-mode excitations, a transformation technique has been demonstrated by authors in [3] in order to obtain its equivalent single-ended network.

The quad-mode antenna is being considered to be placed in a large aperture array of

closely spaced fixed elements. In [2] 96 quad-mode antenna elements were configured in an irregular sparse array layout. The four fundamental multi-mode excitations presented on a quadraxial feed line are solved for maximum gain over a hemispheric FoV coverage using the maximum-gain beamforming theorem. Manufacturing costs are high when the antenna is excited by all four multi-mode excitations. In order to lower the manufacturing costs, a combinational set of complex multi-mode excitation weights will need to be obtained that achieves an optimal hemispherical FoV coverage.

1.2 Objectives

The purpose of this thesis is to investigate beamforming techniques which will allow for the design of aperture array antennas which utilize the quad-mode antenna element. Various algorithms for calculating optimal modal and antenna weights are proposed and compared to one another, ranging from sixteen multi-mode excitation weights for a 2×2 array of quad-mode elements, to only four. The aim in all cases is to optimize the gain in any given direction, over a full hemisphere.

The following concepts will be considered in this thesis:

- A single quad-mode antenna will be optimized for a hemispheric FoV coverage. This is achieved by obtaining a set of multi-mode excitations that will produce a hemispheric beam pattern. The multi-mode set of excitations will be transformed to its equivalent single-ended set of excitations, by employing the transformation technique in [3].

- A feed network will be designed and integrated into the quad-mode antenna. The output of the feed network will consist of the transformed single-ended excitations.

- A 2×2 array configuration will be investigated and a 2×2 quad-mode antenna array will be designed. The beam pattern will be steered to a desired observation point.

- Optimization techniques and the maximum-gain theorem, will be used and an optimal set of multi-mode excitations will be obtained when the quad-mode antenna is configured in an array.

- The maximum-gain beamforming theorem will solve the complex conjugate weighting functions that will achieve a maximum gain at each scanned angle over a FoV coverage. The weighting scheme used will satisfy the conjugate-field matching condition, discussed in [6]. Furthermore, the complex beamforming weighting functions will be optimized using the genetic algorithm and the Nelder-Mead simplex algorithm.

- Different algorithms will be investigated and implemented in Chapter 6.

By employing this procedure the quad-mode antenna will radiate a hemispheric beam pattern which satisfies the SKA specification of 60° from zenith. When placed in an array configuration a broad scanned angle will be illustrated.

1.3   Layout

The thesis initially discusses the theoretical background required for the scope of this thesis in Chapter 2.

The quad-mode antenna pattern will be optimized for a hemispheric beam pattern, this is accomplished by employing the optimization techniques discussed in Chapter 3. This chapter will also explain the implementation process of MATLAB's optimization toolbox.

The quad-mode antenna with an operating frequency of 2 GHz will be discussed in Chapter 4. This chapter will also demonstrate the optimization of the quad-mode antenna beam pattern. The optimized beam pattern will be compared with the Short-Circuit Quadrifilar Helix Antenna, with broadside radiation and circularly-polarized waves. This chapter will conclude by presenting the transformation techniques used by authors in [3] to convert a network terminated by four multi-mode ports to a network terminated by four single-ended mode ports.

Chapter 5 will design a feed network that will be integrated with the quad-mode antenna. In Chapter 6 the quad-mode antenna will be placed in a 2×2 array configuration and beamformed using the optimal set of multi-mode excitations. Other optimization techniques will also be employed in this chapter in order to obtain a set of multi-mode excitations that produce a hemispheric FoV coverage for the quad-mode antenna.

Chapter 7 will conclude by giving a brief overview on what has been done throughout the duration of this thesis.

Chapter 2

Theoretical Framework

2.1   Introduction

This chapter presents the theoretical framework necessary for the scope of this thesis. Section 2.2 will discuss the basic concepts of antenna theory. The basic definitions and relevant theory of microwave network analysis will be presented in Section 2.3. The following Section 2.4 discusses the design and implementation of a 2×2 planar array. The purpose of this antenna array is to electronically steer the radiated power towards a desired angular direction. This is realized by designing the array parameters, which are: the number of antennas in the array, the array geometry and the relative amplitude and phases of the antennas. Once the array is designed, a set of weighting functions can be applied to achieve a specific goal. In this chapter the array will be weighted to maximize the gain pattern of an array over a hemispheric FoV coverage. The maximum-gain beamforming theorem will be implemented in Section 2.5, which applies conjugate-field matching techniques [6].

2.2   Basic Antenna Theory

The radiation pattern of an antenna is represented by the power flux density, radiation intensity, field strength, directivity, phase, and polarization. The total far-field pattern of a single antenna in free space is given in [7] as follows,

$$\mathbf{F}(r, \theta, \phi) = \frac{e^{(-jk_0 r)}}{r}[f^\theta(\theta, \phi)\hat{\mathbf{a}}_\theta + f^\phi(\theta, \phi)\hat{\mathbf{a}}_\phi], \qquad (2.2.1)$$

where $f^{\theta,\phi}(\theta, \phi)$ are the electric field components and k_0 is the propagation constant in free space given by,

$$k_0 = \sqrt{\mu_0 \epsilon_0} = \omega/c_0 = 2\pi/\lambda, \qquad (2.2.2)$$

where the speed of light in a vacuum is $c_0 \simeq 3 \times 10^8$ ms^{-1}. The radiation intensity is a far-field parameter and is defined as follows,

$$U(\theta, \phi) = \frac{1}{2\eta}\big[|f^\theta(\theta, \phi)|^2 + |f^\phi(\theta, \phi)|^2\big]. \qquad (2.2.3)$$

where η is the intrinsic impedance of the medium. The total radiated power of an antenna element is given by,

$$P_{rad} = \int_0^{2\pi} \int_0^\pi U(\theta, \phi) \sin\theta \, d\theta \, d\phi. \qquad (2.2.4)$$

The input power of an antenna can be expressed in terms of the total radiated power and is given as,

$$P_{in} = \frac{P_{rad}}{e_{cd}}, \tag{2.2.5}$$

where e_{cd} is the efficiency factor of the antenna. For an ideal lossless case, the antenna efficiency is $e_{cd} = 1$ and the total radiated power equals the total input power, and Equation (2.2.5) reduces to $P_{rad} = P_{in}$. The efficiency factor will be discussed in more detail in Subsection 2.2.2.

2.2.1 Isotropic Radiator

An isotropic antenna is commonly used in practice as a reference source to evaluate the directivity of actual antennas. It acts as a good reference source because it radiates with equal amplitude in all directions. The total radiated power for an isotropic antenna is given in [7] as follows,

$$P_{rad} = 4\pi r^2 W_0. \tag{2.2.6}$$

The power density is independent of the spherical coordinate angles θ and ϕ, thus it can be written as,

$$\mathbf{W}_0 = W_0 \hat{\mathbf{a}}_r = \left(\frac{P_{rad}}{4\pi r^2}\right)\hat{\mathbf{a}}_r. \tag{2.2.7}$$

The radiation intensity of an isotropic antenna is given by,

$$U_0 = \left(\frac{P_{rad}}{4\pi}\right), \tag{2.2.8}$$

which allows for a uniform distribution.

2.2.2 Directivity, Gain and Realized Gain

The gain of an antenna is an important performance metric for microwave network analysis. Gain takes into account the efficiency and directional capabilities of an antenna. However, according to the IEEE standards [8], gain does not include losses arising from impedance mismatch Γ or polarization mismatches. Therefore two gain equations will be defined and discussed within this subsection. Figure 2.1 depicts the antenna losses and shows how the gain calculations are evaluated. Gain is given by,

$$\begin{aligned} G(\theta, \phi) &= 4\pi \frac{\text{radiation intensity per solid angle in a given direction}}{\text{total input power}}, \\ &= 4\pi \frac{U(\theta, \phi)}{P_{in}}, \end{aligned} \tag{2.2.9}$$

where P_{in} is the total input power. However, the realized gain is less than the gain defined in Equation (2.2.9). This is because realized gain accounts for the reflection losses at the input terminal which are caused by the mismatch between the transmission line and the antenna. It also takes into account the conduction and dielectric losses I^2R which vary depending on the antenna structure. The efficiency of an antenna is given in [7] as follows,

$$\boxed{e_0 = e_r e_c e_d}, \tag{2.2.10}$$
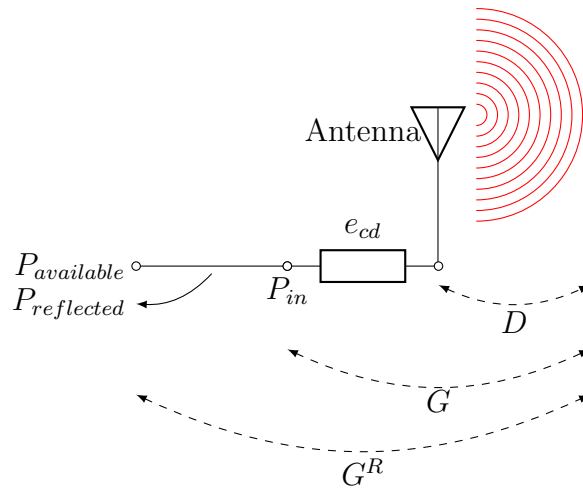
Figure 2.1: Diagram of the performance metrics and losses of an antenna.

with

$e_0 = $ the total efficiency

$e_r = $ the reflection, mismatch, efficiency $= (1 - |\Gamma|^2)$

$e_c = $ conduction efficiency

$e_d = $ dielectric efficiency

$\Gamma = $ reflection coefficient at the input terminal of the antenna

$$\Gamma = \frac{Z_{in} - Z_0}{Z_{in} + Z_0}. \tag{2.2.11}$$

The conduction and dielectric losses are difficult to compute but can be determined experimentally. Therefore, it is more convenient to write Equation (2.2.10) as follows,

$$e_0 = e_r e_{cd} = e_{cd}(1 - |\Gamma|^2), \tag{2.2.12}$$

where e_{cd} is the antenna radiation efficiency and is used to relate the gain and directivity. Directivity is controlled by the antenna pattern and is given by the radiation intensity in a direction over the total radiated power divided by 4π. In mathematical form it is expressed as,

$$D(\theta, \phi) = 4\pi \frac{U(\theta, \phi)}{P_{rad}}, \tag{2.2.13}$$

where the total radiated power is related to the input power according to Equation (2.2.5). The gain defined in Equation (2.2.9) is related to directivity by,

$$G(\theta, \phi) = e_{cd} D(\theta, \phi). \tag{2.2.14}$$

The realized gain of an antenna accounts for the reflection and mismatches losses and is defined as follows,

$$G^R(\theta, \phi) = e_r G(\theta, \phi). \tag{2.2.15}$$

Realized gain can also be expressed in terms of gain and directivity as follows,

$$\begin{aligned} G^R(\theta, \phi) &= e_r G(\theta, \phi) = (1 - |\Gamma|^2)G(\theta, \phi), \\ &= e_r e_{cd} D(\theta, \phi) = e_0 D(\theta, \phi). \end{aligned} \tag{2.2.16}$$
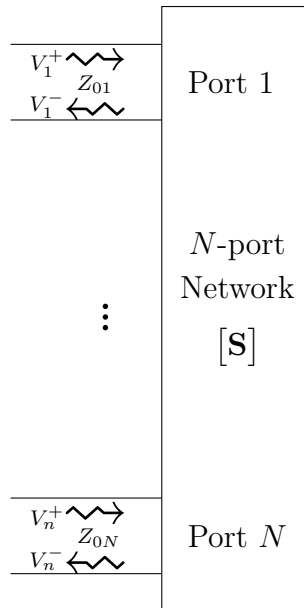
Figure 2.2: N-port network

Furthermore in decibels,

$$G^R(\theta, \phi) = 10 \log\big(|e_0 D(\theta, \phi)|\big) = 10 \log\big(|G^R(\theta, \phi)|\big) \quad \big[dB\big]. \qquad (2.2.17)$$

The gain for an isotropic antenna is unity or $0\ dBi$. The gain or the power pattern of an antenna is a good performance parameter and will be used throughout this thesis to analytically verify the obtained results.

2.3 Basic Network Definitions

The network theory discussed in this section is adapted from [9].

At microwave frequencies the determination of voltages and currents on a transmission line becomes more complex. This is because at higher frequencies inductance and capacitance values of components decrease and lumped-circuit analysis becomes impractical. When frequencies start approaching the microwave range the electrical wavelength on the transmission line is comparable to its length and basic network theory can be applied. Basic network theory entails the determination of the reflected, incident, and transmitted waves. An N-port network, as shown in Figure 2.2, will be characterized by the scattering parameters also known as the S-parameters. The scattering parameters are determined by the incident and reflected waves at each port.

2.3.1 Generalized Scattering Parameters and Power Waves

An N-port network, as shown in Figure 2.2, depicts the incident voltage wave V_n^+ and reflected voltage wave V_n^-. The scattering matrix at the m, n^{th} element are defined as,

$$S_{m,n} = \frac{V_m^-}{V_n^+}\Big|_{V_k^+ = 0 \text{ for } k \neq n} \qquad . \qquad (2.3.1)$$

This means that the m, n^{th} scattering element is found, by activating port n with an incident voltage wave V_n^+ and determining the reflected wave V_m^- seen on port m, where all other port incident voltages are zeroed. When all ports are terminated with a matched load, the reflection coefficient of the mth port is given by $S_{m,n}$ and can be calculated using Equation (2.3.1).

The S-matrix can be defined in terms of the impedance and admittance matrices. The total voltage and current at port n is given by,

$$
\begin{aligned}
V_n &= V_n^+ + V_n^-, \\
I_n &= I_n^+ - I_n^- = V_n^+ - V_n^-.
\end{aligned}
\tag{2.3.2}
$$

with a normalized characteristic impedance, $Z_{0n} = 1$. Using network analysis, the impedance matrix is related to the port voltages and currents as follows $\mathbf{V} = [\mathbf{Z}][\mathbf{I}]$, and Equation (2.3.2) can be given in matrix notation by,

$$
[\mathbf{Z}][\mathbf{I}] = [\mathbf{Z}][\mathbf{V}^+] - [\mathbf{Z}][\mathbf{V}^-] = [\mathbf{V}] = [\mathbf{Z}] + [\mathbf{V}^+],
\tag{2.3.3}
$$

which can be rewritten as follows,

$$
([\mathbf{Z}] - [\mathbf{I}])[\mathbf{V}^+] = ([\mathbf{Z}] + [\mathbf{I}])[\mathbf{V}^-],
\tag{2.3.4}
$$

where $\mathbf{I}$ is a diagonal identity matrix. By substituting Equation (2.3.4) into Equation (2.3.1) and rewriting the equation the S-matrix can be calculated as,

$$
[\mathbf{S}] = ([\mathbf{Z}] + [\mathbf{I}])^{-1}([\mathbf{Z}] - [\mathbf{I}]).
\tag{2.3.5}
$$

The travelling waves used in transmission line theory can be defined in terms of power waves, which makes power transfer calculations from the generator to load much simpler. The incident a and reflected b power wave equation is given in terms of the total voltage and current as follows,

$$
\begin{aligned}
a &= \frac{V + Z_R I}{2\sqrt{R_R}}, \\
b &= \frac{V - Z_R^* I}{2\sqrt{R_R}},
\end{aligned}
\tag{2.3.6}
$$

where $Z_R = R_R + jX_R$ is a complex reference impedance and with V and I being the total voltages and currents on a transmission line given in Equation (2.3.2). The power delivered to the load is defined as,

$$
P_L = \frac{1}{2}\mathrm{Re}\{VI^*\},
\tag{2.3.7}
$$

which is the normal power definition. Equation (2.3.6) can be rewritten such that the total voltage and current are given in terms of the power waves as follows,

$$
\begin{aligned}
V &= \frac{Z_R^* a + Z_R b}{\sqrt{R_R}}, \\
I &= \frac{a - b}{\sqrt{R_R}}.
\end{aligned}
\tag{2.3.8}
$$

Equation (2.3.7) can then be calculated and is given in [4] by,

$$
P_L = \frac{1}{2}[|a|^2 - |b|^2],
\tag{2.3.9}
$$

where the total power delivered to the load is the difference between the incident and reflected power waves on the line.
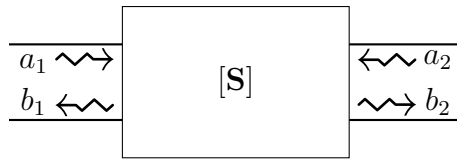
Figure 2.3: A 2-port network representation.

2.3.2 Single-ended Scattering Parameters

The scattering parameters are used to describe the power waves at the input and output ports when properly terminated. Furthermore, authors in [10] show that microwave circuits can be treated as single-ended and the scattering parameters can be obtained for a 2-port network, as shown in Figure 2.3. A 2-port network can be mathematically represented in matrix form as follows,

$$
\begin{bmatrix} b_1 \\ b_2 \end{bmatrix} = \begin{bmatrix} S_{11} & S_{12} \\ S_{21} & S_{22} \end{bmatrix} \begin{bmatrix} a_1 \\ a_2 \end{bmatrix}.
\tag{2.3.10}
$$

The S-parameters are defined as,

$$
\begin{aligned}
\text{The reflected power at port 1} \quad S_{11} &= \tfrac{b_1}{a_1}\big|_{a_2=0}, \\
\text{The reverse voltage gain} \quad S_{12} &= \tfrac{b_1}{a_2}\big|_{a_1=0}, \\
\text{The forward voltage gain} \quad S_{21} &= \tfrac{b_2}{a_1}\big|_{a_2=0}, \\
\text{The reflected power at port 2} \quad S_{22} &= \tfrac{b_2}{a_2}\big|_{a_1=0}.
\end{aligned}
\tag{2.3.11}
$$

2.3.3 Mixed-Mode Scattering Parameters

Mixed-mode scattering parameters can be derived using two single-ended networks that are the differential- and common-mode networks. The mixed-mode scattering parameters are given in [11] in matrix form as follows,

$$
\begin{bmatrix} b_{d1} \\ b_{d2} \\ b_{c1} \\ b_{c2} \end{bmatrix} = \begin{bmatrix} \begin{bmatrix} S_{dd11} & S_{dd12} \\ S_{dd21} & S_{dd22} \end{bmatrix} & \begin{bmatrix} S_{dc11} & S_{dc12} \\ S_{dc21} & S_{dc22} \end{bmatrix} \\ \begin{bmatrix} S_{cd11} & S_{cd12} \\ S_{cd21} & S_{cd22} \end{bmatrix} & \begin{bmatrix} S_{cc11} & S_{cc12} \\ S_{cc21} & S_{cc22} \end{bmatrix} \end{bmatrix} \begin{bmatrix} a_{d1} \\ a_{d2} \\ a_{c1} \\ a_{c2} \end{bmatrix},
\tag{2.3.12}
$$

where a_{cn}, a_{dn}, b_{cn}, and b_{dn} are the common and differential mode incident and reflected power waves at port n. The S-matrix submatrices are defined as; S_{dd} the differential-mode, S_{dc} mode conversion of common to differential, S_{cd} mode conversion of differential to common mode and S_{cc} the common-mode.

2.3.4 Single-Ended to Mixed-Mode Conversion

The simplest way to measure mixed-mode scattering parameters on a vector network analyser is to obtain the single-ended port voltage, current and impedance at each port

and obtaining the mixed-mode parameters as outlined in [10] as follows,

$$
\begin{aligned}
V_{dn} &= V_{2n-1} - V_{2n} \quad V_{cn} = \frac{V_{2n-1} + V_{2n}}{2}, \\
I_{dn} &= \frac{I_{2n-1} - I_{2n}}{2} \quad I_{cn} = V_{2n-1} - V_{2n}, \\
Z_d &= \frac{V_d}{I_d} = 2Z_{oo} \quad Z_c = \frac{V_c}{I_c} = \frac{Z_{eo}}{2}.
\end{aligned}
\tag{2.3.13}
$$

The differential- and common-mode incident and reflected power waves are computed using Equation (2.3.6) as follows,

$$
\begin{aligned}
a_{dn} &= \frac{1}{2\sqrt{Z_{dn}}}(V_{dn} + Z_{dn}I_{dn}), \\
a_{cn} &= \frac{1}{2\sqrt{Z_{cn}}}(V_{cn} + Z_{cn}I_{cn}), \\
b_{dn} &= \frac{1}{2\sqrt{Z_{dn}}}(V_{dn} - Z_{dn}I_{dn}), \\
b_{cn} &= \frac{1}{2\sqrt{Z_{dn}}}(V_{cn} - Z_{cn}I_{cn}).
\end{aligned}
\tag{2.3.14}
$$

The single-ended voltages and currents at port n can be rewritten in terms of the incident and reflected voltages as,

$$
\begin{aligned}
V_n &= \sqrt{Z_0}(a_n + b_n), \\
I_n &= \frac{1}{\sqrt{Z_0}}(a_n - b_n),
\end{aligned}
\tag{2.3.15}
$$

Equations (2.3.13) – (2.3.15) can be substituted into Equation (2.3.14) in order to calculate the mixed-mode power waves in terms of the single-ended power waves, which are given by [10] as,

$$
\begin{aligned}
a_{dn} &= \frac{a_{2n-1} - a_{2n}}{\sqrt{2}} \quad a_{cn} = \frac{a_{2n-1} + a_{2n}}{\sqrt{2}}, \\
b_{dn} &= \frac{b_{2n-1} - b_{2n}}{\sqrt{2}} \quad b_{cn} = \frac{b_{2n-1} + b_{2n}}{\sqrt{2}}.
\end{aligned}
\tag{2.3.16}
$$

By inserting Equation (2.3.16) into Equation (2.3.12) the following conversion is obtained,

$$
\mathbf{S}^{mm} = [\mathbf{M}][\mathbf{S}][\mathbf{M}]^{-1},
\tag{2.3.17}
$$

where $\mathbf{S}^{mm}$ is the mixed-mode scattering matrix, $\mathbf{S}^{se}$ the single-ended mode scattering matrix and $\mathbf{M}$ is the transformation matrix, which is given by,

$$
\mathbf{M} = \begin{bmatrix} 1 & -1 & 0 & 0 \\ 0 & 0 & 1 & -1 \\ 1 & -1 & 0 & 0 \\ 0 & 0 & 1 & 1 \end{bmatrix}.
\tag{2.3.18}
$$

This conversion is only valid when the characteristic impedances are equal $Z_{oo} = Z_{oe} = Z_0$ between the common- and differential-mode ports. This means that there is no coupling between the differential signals. Authors in [12] have introduced coupling terms k_{oo} and k_{oe} in order to include the common- and differential-mode impedances. The above equation can therefore be newly defined by inserting $Z_{oo} = k_{oo}Z_0$ and $Z_{oe} = k_{oe}Z_0$ into Equation (2.3.16) as follows,

$$
\begin{aligned}
a_{dn} &= \frac{(1+k_{oo})(a_{2n-1} - a_{2n}) + (1-k_{oo})(b_{2n-1} - b_{2n})}{2\sqrt{2k_{oo}}}, \\
a_{cn} &= \frac{(1+k_{oe})(a_{2n-1} + a_{2n}) + (1-k_{oe})(b_{2n-1} - b_{2n})}{2\sqrt{2k_{oe}}}, \\
b_{dn} &= \frac{(1+k_{oo})(b_{2n-1} - b_{2n}) + (1-k_{oo})(a_{2n-1} - a_{2n})}{2\sqrt{2k_{oo}}}, \\
b_{cn} &= \frac{(1+k_{oe})(b_{2n-1} + b_{2n}) + (1-k_{oe})(a_{2n-1} - a_{2n})}{2\sqrt{2k_{oe}}}.
\end{aligned}
\tag{2.3.19}
$$

Additionally Equation (2.3.17) becomes,

$$
\mathbf{S}^{mm} = ([\mathbf{M}_1][\mathbf{S}^{se}] + [\mathbf{M}_2])([\mathbf{M}_1] + [\mathbf{M}_2][\mathbf{S}^{se}])^{-1},
\tag{2.3.20}
$$

where the mixed-mode transformation matrices, $\mathbf{M}_1$ and $\mathbf{M}_2$, are given by,

$$
\mathbf{M}_1 = \begin{bmatrix}
\frac{1+k_{oo}}{2\sqrt{2k_{oo}}} & -\frac{1+k_{oo}}{2\sqrt{2k_{oo}}} & 0 & 0 \\
0 & 0 & \frac{1+k_{oo}}{2\sqrt{2k_{oo}}} & -\frac{1+k_{oo}}{2\sqrt{2k_{oo}}} \\
\frac{1+k_{oe}}{2\sqrt{2k_{oe}}} & -\frac{1+k_{oe}}{2\sqrt{2k_{oe}}} & 0 & 0 \\
0 & 0 & \frac{1+k_{oe}}{2\sqrt{2k_{oe}}} & \frac{1+k_{oe}}{2\sqrt{2k_{oe}}}
\end{bmatrix},
\tag{2.3.21}
$$

$$
\mathbf{M}_2 = \begin{bmatrix}
\frac{1-k_{oo}}{2\sqrt{2k_{oo}}} & -\frac{1-k_{oo}}{2\sqrt{2k_{oo}}} & 0 & 0 \\
0 & 0 & \frac{1-k_{oe}}{2\sqrt{2k_{oe}}} & \frac{1-k_{oe}}{2\sqrt{2k_{oe}}} \\
\frac{1-k_{oo}}{2\sqrt{2k_{oo}}} & -\frac{1-k_{oo}}{2\sqrt{2k_{oo}}} & 0 & 0 \\
0 & 0 & \frac{1-k_{oe}}{2\sqrt{2k_{oe}}} & \frac{1-k_{oe}}{2\sqrt{2k_{oe}}}
\end{bmatrix}.
\tag{2.3.22}
$$

2.4 Basic Antenna Array Theory Components

A uniform planar array configuration, as shown in Figure 2.4, will be used to discuss the array theory components. The elements are spaced a distance d_y along the y-axis and d_x along the x-axis. The array configuration has identical antenna elements which are fed with an excitation of identical magnitude and a linear progressive phase delay. Figure 2.4 shows a planar array with elements positioned on a rectangular grid, spaced a distance $d = \lambda/2$ apart. The radiation pattern of an array in the far-field is derived by superimposing each individual element's field pattern with its relative phase shift, where the radiated field intensity of a single antenna element is given in Equation (2.2.1). The far-field radiated pattern, for a 2×2 planar array, with identical antenna elements and an interelement spacing of $d_x = d_y = \lambda/2$ is given by,

$$
\mathbf{F}_{array} = \mathbf{F}(\theta, \phi) AF(\theta, \phi),
\tag{2.4.1}
$$
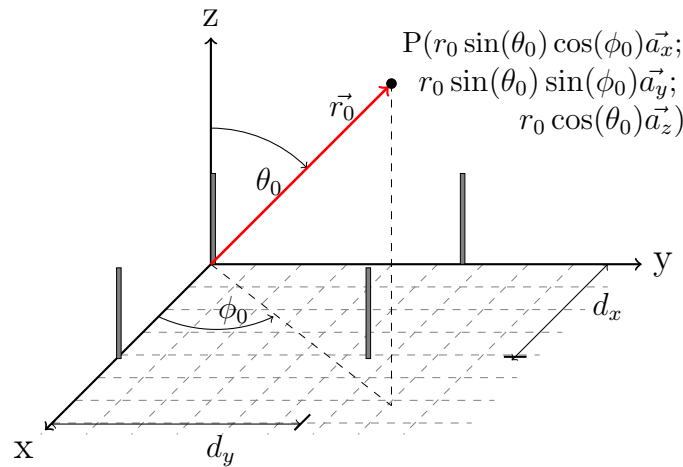
Figure 2.4: 2×2 Uniform Planar Array

where the matrix $\mathbf{F}(\theta, \phi)$ is the electrical field distribution of a single antenna element, given in Equation (2.2.1). The array factor, $AF(\theta, \phi)$, for a 2×2 array is given in [7] as follows,

$$AF(\theta, \phi) = \sum_{n=1}^{2} \sum_{m=1}^{2} w_{m,n} \; e^{jk_0 \frac{\lambda}{2}(m-1)(\sin\theta\cos\theta - \beta_x) + jk_0 \frac{\lambda}{2}(n-1)(\sin\theta\sin\theta - \beta_y)}. \tag{2.4.2}$$

where k_0 is the propagation constant defined in Equation (2.2.2) and $w_{m,n}$ is the complex weighting function that will be discussed in Section 2.5. The beam pattern of the array can be steered towards a desired angular direction θ_0, ϕ_0 by applying a linear progressive phase shift to each element within the array. The necessary linear progressive phase shift is given by,

$$\beta_y = -\sin\theta_0 \sin\phi_0, \quad \beta_x = -\sin\theta_0 \cos\phi_0. \tag{2.4.3}$$

Assuming all elements are identical and perfectly matched, the array power gain pattern can be calculated using the principle of pattern multiplication. The principle of pattern multiplication is discussed in [7] and is given by,

$$\begin{aligned}
G^A(\theta, \phi) &= G(\theta, \phi)|AF(\theta, \phi)|^2, \\
U^A(\theta, \phi) &= U(\theta, \phi)|AF(\theta, \phi)|^2,
\end{aligned} \tag{2.4.4}$$

where $G(\theta, \phi)$ is the gain, given in Equation (2.2.14) and $U(\theta, \phi)$ is the radiation intensity of a single antenna element.

2.4.1   Array Pattern Multiplication of The Embedded Element Pattern

Figure 2.5 shows the geometry of an N-element linear array, where each element is identical and mutual coupling effects are neglected. Figure 2.6 depicts the geometry of an N-element linear array where one element has been excited and all other elements are terminated with a matched load. The excited element in Figure 2.6 will radiate differently than the isolated element in Figure 2.5, as mentioned above, and the pattern obtained is known as the embedded element pattern. The embedded element pattern accounts for the

mutual coupling effects in the antenna and also for the possibility of scanned blindnesses, as discussed in [13]. Furthermore, the author in [9] shows that for an infinite array the embedded element pattern for each antenna can be approximated as being equal. Therefore the property of pattern multiplication can be applied and the array gain obtained. The gain characteristics will differ from that of an isolated element, due to mutual coupling effects that cause additional current modes when steering the array to a specific direction.
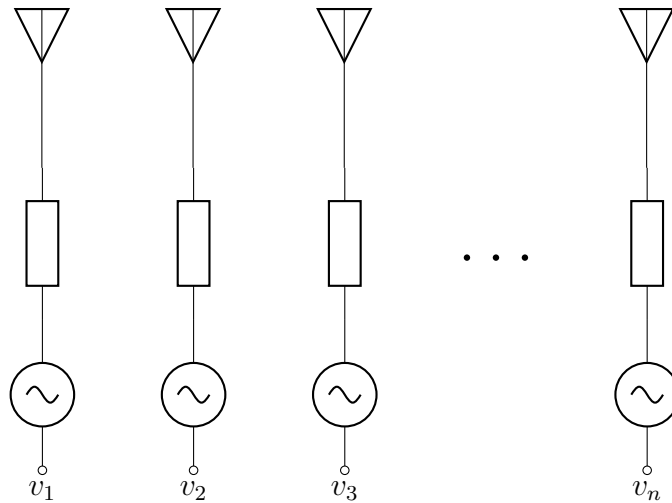
Figure 2.5: Geometry of a uniform N-element linear array.
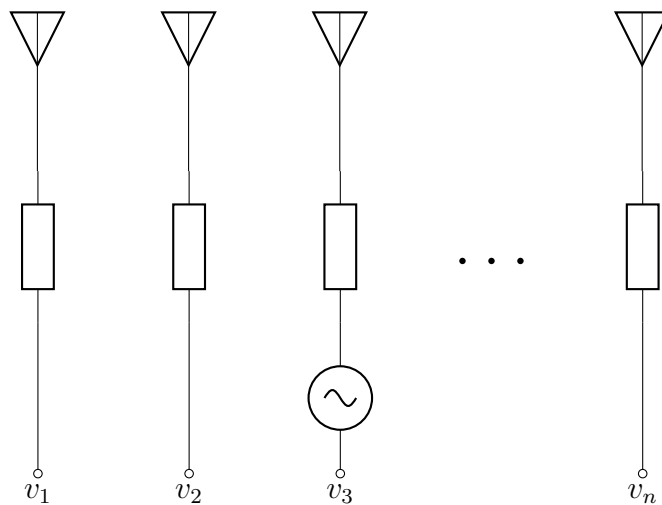
Figure 2.6: Geometry of an EEP within a N-element linear array.

2.4.2   Active Reflection Coefficient

The active reflection coefficient is the input reflection coefficient of the embedded element pattern. When scanning the beam of an N-element array as shown in Figure 2.6 to an angle θ_0 the reflection coefficient changes and the resulting reflection coefficient is called the active reflection coefficient. This is due to the adjacent elements radiating power

which is caused by mutual coupling effects. The incident voltage at the nth terminal port is given by,

$$V_n^+ = V_0 e^{-jknd\sin\theta_0},$$

(2.4.5)

where V_0 is the terminal voltage. Rewriting Equation (2.3.1) and equating the reflected wave to the scanned incident voltages and the S-matrix, the reflected wave at m^{th} element is given by,

$$V_m^- = \sum_{n=1}^{N} S_{mn} V_n^+$$

(2.4.6)

The active reflection coefficient can then be determined from substituting Equation (2.4.5) into Equation (2.4.6) as follows,

$$\Gamma_m(\theta_0) = \frac{V_m^-}{V_m^+} = \mathrm{e}^{jkmd\sin\theta_0} \sum_{n=1}^{N} S_{mn} \, \mathrm{e}^{-jknd\sin\theta_0}.$$

(2.4.7)

The active reflection coefficient depends on the scanned angle θ_0 unless there is no mutual coupling and $S_{mn} = 0$ for $m \neq n$.

2.5 Beamforming Implementation

Obtaining a set of parameters that maximizes a certain performance metric is a common engineering problem. This is a recurring problem for discrete systems where parameters only have significance at discrete values. For example, the maximization of the directive gain of an antenna array can be solved using the theorem presented in [14].

2.5.1 Steering Vector

Figure 2.7 illustrates an N element linear array beamformer. If the input signal from the nth element is given in vector notation as,

$$\mathbf{F}(\theta, \phi) = f_n^\theta(\theta, \phi)\hat{\boldsymbol{\theta}} + f_n^\phi(\theta, \phi)\hat{\boldsymbol{\phi}}.$$

(2.5.1)

To maximize the received power a weighting scheme is considered that satisfies the conjugate-field matching condition [6]. The complex conjugate beamformer weights are given as $\mathbf{w}^H = [w_1^*, \ldots, w_n^*]$ with the superscript ^{H} denoting the Hermitian transpose vector and the asterisk * denoting the complex vector. The beamformer output signal vector is obtained by adding the weighted received signals, given as

$$v = \sum_{n=1}^{N} w_n^* f_n^{\theta,\phi},$$

$$= \mathbf{w}^H \mathbf{F}.$$

(2.5.2)

When the angle of observation is (θ_0, ϕ_0) the beamformer input signal can be expressed in an $[N \times 2]$ matrix as,

$$\mathbf{F} = \begin{bmatrix} f_1^\theta(\theta_0, \phi_0) & f_1^\phi(\theta_0, \phi_0) \\ & \vdots & \\ f_n^\theta(\theta_0, \phi_0) & f_n^\phi(\theta_0, \phi_0) \end{bmatrix}.$$

(2.5.3)
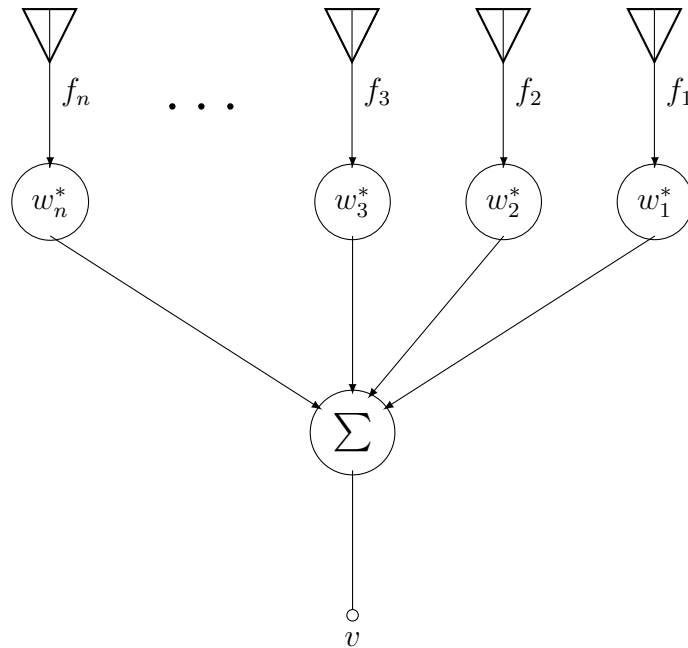
Figure 2.7: An ideal beamformer system.

2.5.2   General Formulation for Maximum-Gain Algorithm

In order to steer the beam pattern of the above mentioned array, the maximum-gain beamforming theorem is applied and a maximum radiation pattern can be obtained. This is done by maximizing the gain given in Equation (2.2.9) for a given direction. Using Equation (2.5.2) the beamformer output power can be written as $vv^* = \left(\mathbf{w}^H \mathbf{F}\right)\left(\mathbf{w}^H \mathbf{F}\right)^*$. The total radiation intensity given Equation (2.2.3) is calculated as,

$$
\begin{aligned}
U(\theta, \phi) &= \frac{1}{2\eta}\left(\mathbf{w}^H \mathbf{F}\right)\left(\mathbf{w}^H \mathbf{F}\right)^*, \\
&= \frac{1}{2\eta}\left(\mathbf{w}^H \mathbf{F}\mathbf{F}^H \mathbf{w}\right).
\end{aligned}
\tag{2.5.4}
$$

The total radiated power can be calculated in terms of the incident and reflected waves, $\mathbf{w}$ and $\mathbf{b}$, respectively as,

$$
\begin{aligned}
P_{rad} &= P_{max} - P_{reflected} \\
&= \sum_n^N (|w_n|^2) - (|b_n|^2) \\
&= \mathbf{w}^H \mathbf{w} - \mathbf{b}^H \mathbf{b} \\
&= \mathbf{w}^H \mathbf{w} - \mathbf{w}^H \mathbf{S}^H \mathbf{S} \mathbf{w} \\
&= \mathbf{w}^H [\mathbf{I} - \mathbf{S}^H \mathbf{S}] \mathbf{w},
\end{aligned}
\tag{2.5.5}
$$

where $\mathbf{B}$ is an $N \times N$ square matrix given as $\mathbf{B} = [\mathbf{I} - \mathbf{S}^H \mathbf{S}]$ and for an ideal beamformer the incident wave is used to as the complex beamformer weight vector. The gain is expressed as follows,

$$
G(\theta, \phi) = \frac{4\pi}{\eta} \frac{\mathbf{w}^H \mathbf{F} \mathbf{F}^H \mathbf{w}}{\mathbf{w}^H \mathbf{B} \mathbf{w}}.
\tag{2.5.6}
$$

Taking the partial derivative of Equation (2.5.6) with respect to $\mathbf{w}^H$ and equating the result to zero as,

$$\frac{\partial G(\theta, \phi)}{\partial \mathbf{w}^H} = \frac{\mathbf{w}^H [\mathbf{B}] \mathbf{w} \mathbf{F} \mathbf{F}^H \mathbf{w} - \mathbf{w}^H \mathbf{F} \mathbf{F}^H \mathbf{w} [\mathbf{B}] \mathbf{w}}{[\mathbf{w}^H [\mathbf{B}] \mathbf{w}]^2} = 0,$$

$$\therefore \mathbf{w}^H [\mathbf{B}] \mathbf{w} \mathbf{F} \mathbf{F}^H \mathbf{w} = \mathbf{w}^H \mathbf{F} \mathbf{F}^H \mathbf{w} [\mathbf{B}] \mathbf{w},$$

$$\mathbf{F} \mathbf{F}^H \mathbf{w} = \left[\frac{\mathbf{w}^H \mathbf{F} \mathbf{F}^H \mathbf{w}}{\mathbf{w}^H [\mathbf{B}] \mathbf{w}} \right] [\mathbf{B}] \mathbf{w},$$

$$\mathbf{F} \mathbf{F}^H \mathbf{w} = \frac{\eta}{4\pi} G(\theta, \phi) [\mathbf{B}] \mathbf{w}. \tag{2.5.7}$$

Setting $\mathbf{A} = \mathbf{F} \mathbf{F}^H$, two $N \times N$ square matrices are defined and the problem can be solved as a generalized eigenvalue problem. The characteristic equation is defined as follows [14],

$$\mathbf{A} \mathbf{w} = \lambda \mathbf{B} \mathbf{w}, \tag{2.5.8}$$

where λ is the eigenvalue and $\mathbf{w}$ the eigenvector and the roots can be obtained by taking the determinant of,

$$\det(\mathbf{A} - \lambda \mathbf{B}) \mathbf{w} = 0. \tag{2.5.9}$$

When solving for the largest eigenvalue of Equation (2.5.6) the complex beamforming weights are obtained that result in maximum gain for all desired angles.

2.6   Conclusion

This chapter discussed the basic concepts of antennas which are used throughout this thesis. This chapter also discussed network and transmission line theory which is used later in this thesis for the design and implementation of a feed network. Furthermore, the basic components used in array theory were discussed and an example was given of a 2×2 planar array configuration. The last section discussed the basic components used in Chapter 6. This section explains how radiators are weighted in order to achieve a maximum radiation pattern towards a desired observation point. This chapter explained and discussed the necessary tools which will be implemented in this thesis.

Chapter 3

Optimization Techniques

3.1 Introduction

This chapter will discuss different optimization techniques such as the local searches and a global search algorithm, which are FMINSEARCH and the Genetic Algorithm (GA), MATLAB optimization toolboxes, respectively. Most optimizations are based on finding an optimum set of solutions, each solution set is evaluated through the fitness, cost or objective function.

Section 3.2 will discuss the basic concept of optimization and give a few examples of optimization solvers.

A fitness function will evaluate the fitness values for each solution found in the search space, the function will be discussed in Section 3.3.

Section 3.4 will give a brief introduction to evolutionary computation and the GA will be explained in Subsection 3.4.1. Subsection 3.4.2 will implement the GA solver based on the scope of this thesis.

The FMINSEARCH toolbox in MATLAB is based on the Nedler-Mead algorithm which will be discussed in Section 3.5 and Subsection 3.5.1 will show how MATLAB implements the algorithm's search space.

Section 3.6 will conclude this chapter.

This thesis will use the discussed optimization solvers in order to maximize the quad-mode antenna gain pattern for a hemispheric FoV coverage. The antenna will be placed in a 2×2 planar array configuration and the array beam pattern will be maximized towards a desired direction. This will be done through using the optimization techniques that will be discussed in this chapter. This chapter will explain how to set up the optimization solvers in MATLAB in order to achieve feasible solutions to the defined problem.

3.2 Introduction to Global and Local Optimization

The basic principle of optimization is to find a solution that will give you the best performance regarding the problem. A problem can be solved by defining a function that will help to make the task easier, the function is known as the fitness function. The type of optimization algorithm used, will determine how the fitness function is defined. The fitness function has no mathematical restrictions regarding the optimization algorithm. When the data supplied to the fitness function is continuous data, as opposed to discrete data, an efficient local optimization would be faster to implement, for instance a gradient based or Hessian (Newton's method) optimization methods.

There are a few criteria used to classify optimization algorithms. For example determining whether or not a problem is continuous or discrete, unconstrained or constrained, and sequential or parallel. It is easy to distinguish a discrete problem from a continuous one, but you can also make use of a continuous optimization tool to solve a discrete problem. This is the same for parallel and sequential optimization techniques. Parallel algorithms are mostly used to speed up processing, but cases exist where it is more efficient to use parallel rather than sequential optimization techniques. These cases include, among others, cases in which there is a high probability of each individual search to get stuck in a local optima.

Optimization methods can also be classified into deterministic or non-deterministic, and global or local methods. The difference between global and local optimizers depends on their search space. A global optimizer will be more likely to find a global minimum, whereas a local optimizer might converge to a local minimum, due to the initial set of values. An optimizer finds a solution based on the basin of attractions of the starting point. The basin of attraction is the search space over which the function will iterate and evolve to a particular solution. Global optimizers run through multiple sets of basins, they can use local optimizers to find the optimum in the basins of attraction of starting points.

For example by considering the genetic algorithm, which is a stochastic algorithm where randomness plays an essential role in the optimization of the problem. The algorithm is robust, and has the ability to perform consistently. Almost all conventional optimization techniques search from a single point but the GA operates on a whole population of points. The GA uses a probabilistic transition operator rather than deterministic transition for continuous optimization problems. There is no definite difference between local and global optima other than the continuous convex problem, which is a small set of problems. The only way of validating that a global optimum has been reached, is to evaluate all possible solutions to the problem. This is where using the GA algorithm proves to be useful. The GA algorithm improves a set of solutions to an optimum and at the end of a run it will show whether the solution is a global or local optimum.

In this chapter two MATLAB optimization toolboxes will be discussed, the GA and the FMINSEARCH solvers. The GA solver generates multiple sets of starting points, known as the population. The solver iterates through the population and generates a new population with a better set of solutions. The FMINSEARCH solver is a local optimizer that sets the basin of attraction based on the user-supplied initial starting point. This solver searches for a minimum and terminates when a solution is found. Therefore the function will converge quicker by setting the initial value close to a local minimum point.

3.3 Fitness Function

The fitness function is used to assign a cost value to an individual of the set of solutions. This determines the feasibility of the individual set of solutions. The fitness function is defined by the optimization problem and is also considered to be the only relation between the problem and the actual optimization.

Using the global optimization toolkit in MATLAB, the function will expect a vector $\mathbf{x}$ of length n and return a scalar value known as the fitness value. For example finding the minimum of the function $F(\mathbf{x}) = (x_1 - x_2)^2 + (1 - x_1)^2$. The function accepts two variables and a scalar value is returned $F = \min F(\mathbf{x})$. The solver minimizes the fitness value F by varying the two variables. This is repeated until the stopping criterion is met and a

solution set of variables is found.

The fitness function can be vectorized which will speed up the process by evaluating a set of points and returning a vector **y** with a set of values. For example consider solving a matrix **x** of 5 rows and 2 columns. Using the previous fitness function $F(x) = (x_1 - x_2)^2 + (1 - x_1)^2$ with two variables, the vectorized function will accept the matrix x and evaluate the 5 rows. The fitness function will return a vector **y** with 5 rows.

3.4 Evolutionary Computation

Evolutionary computation can be best described by Charles Darwin's theory of natural evolution in *On the Origin of Species*, *"survival of the fittest"*, as discussed in [15]. Evolutionary computation techniques abstract evolutionary principles such as selection, mutation and reproduction into algorithms that may be used to search for the optimal solution. The process begins by randomly initialising an individual population. New solutions are generated by applying "genetic" operations that form a separate new population to replace the previous population. The selection criteria by which individuals become part of the genetic operations, are evaluated by a performance metric known as the fitness measure. This process cycles through a number of "generations" until a previously specified maximum number of generations has been met or a solution is found.

There are four well known concepts based on evolutionary computation, these are: genetic algorithms (Holland, 1975), genetic programming (Koza, 1992, 1994), evolutionary strategies (Recheuberg, 1973), and evolutionary programming (Forgel et al., 1966).

3.4.1 Genetic Algorithms

The genetic algorithm was first used by Holland in 1975, as explained in [16], but officially formalized by De Jong in 1975 as a functional optimization. Holland's GA method moves from one population of chromosomes, which is implemented as a string of bits, to a new population by using natural selection together with genetics-inspired operations of crossover, mutation and inversion. A GA population can be implemented by an array of data or a string of bits known as chromosomes. For each optimization problem one is looking for the best solution out of all possible solutions. All feasible solutions can be placed in a search space. Each chromosome or solution within this search space can be marked by its fitness value, where the fitness value depends on the problem at hand. Each string of chromosomes consists of "genes" or bits of ones and zeros or floating point numbers. Holland's GA method originally presents genes as bit strings, however the author in [17] shows that the solution can be found more accurately when implementing the real-valued GA. It saves on CPU time and serves as a more natural selection process.

A set of new solutions is formed or reproduced by using the selection operators together with their fitness value. The GA solver successfully replaces a population of chromosomes by enforcing the natural selection processes, thereby improving the fitness of the population. Figure 3.1 presents a block diagram of the GA that works as follows:

- The algorithm starts by randomly generating a set of population of chromosomes (possible solutions).

- The fitness value F of each chromosome x in the population n is calculated.

- A new population set is formed by using the GA operators and this process is repeated until n offspring have been created.

- The selection operator in GA is where a pair of parent chromosomes is selected from the current population by means of an increasing function of fitness. The same chromosome can be selected more than once.

- The crossover operation in GA chooses two chromosomes out of the population and randomly exchanges the sequence of their genes. The crossover happens with a crossover probability P_c at a randomly chosen point (mostly chosen with uniform probability) to form two offspring. If no crossover takes place the offspring are identical to their parents.

- The mutation operation in GA is where two offspring are created by mutating their genes within a chromosome with a mutation probability P_m. The resulting chromosomes are then placed in a new set of population. When n is an odd number one new set of population can be discarded at random.

- The last step is where the old population is replaced by the new one and the whole process repeats itself until a set number of generations (each iteration) has been reached or the solution has been found.

The most common application of the GA is its optimization function. The function goal is to obtain a set of parameters that maximizes or minimize the fitness value. Using the GA solver in optimization search strategies, a set of trial solutions will evolve towards an optimal set of solution under the genetic process.

3.4.2   Matlab Implementation of Genetic Algorithms Toolbox

To use the GA toolkit in MATLAB the solver is set to predefine the function before the optimization implementation. The following settings are defined for the GA optimization in order to minimize the defined fitness function. When the optimization problem's set of parameters are in a continuous domain, a floating representation serves as a better option, as proven in [18]. To minimize the fitness function, given in Section 3.3, a fitness function handle is passed with the specified number of variables given and the option arguments, that the solver uses, are set before execution. The problem is constrained to a vector of boundaries that is defined in the GA options. For global search algorithms, setting the boundary of the set of variables is crucial. It limits the scattered-searching and makes sure that the solver maintains a feasible solution in every iteration.

The following operations are set in MATLAB before the GA optimization process is carried out.

- 20 individuals are created for the initial population, this is set by using the GACREATIONNONLINEARFEASIBLE function option for the GA. This option will create a feasible population by including all constraints and will initialize the set with respect to the boundary constraints condition specified.

- The population type is set to doubleVector, as mentioned above, this is done in order to obtain a reasonable set of results, as the individuals supplied to the solver are variables that are defined as a type double.
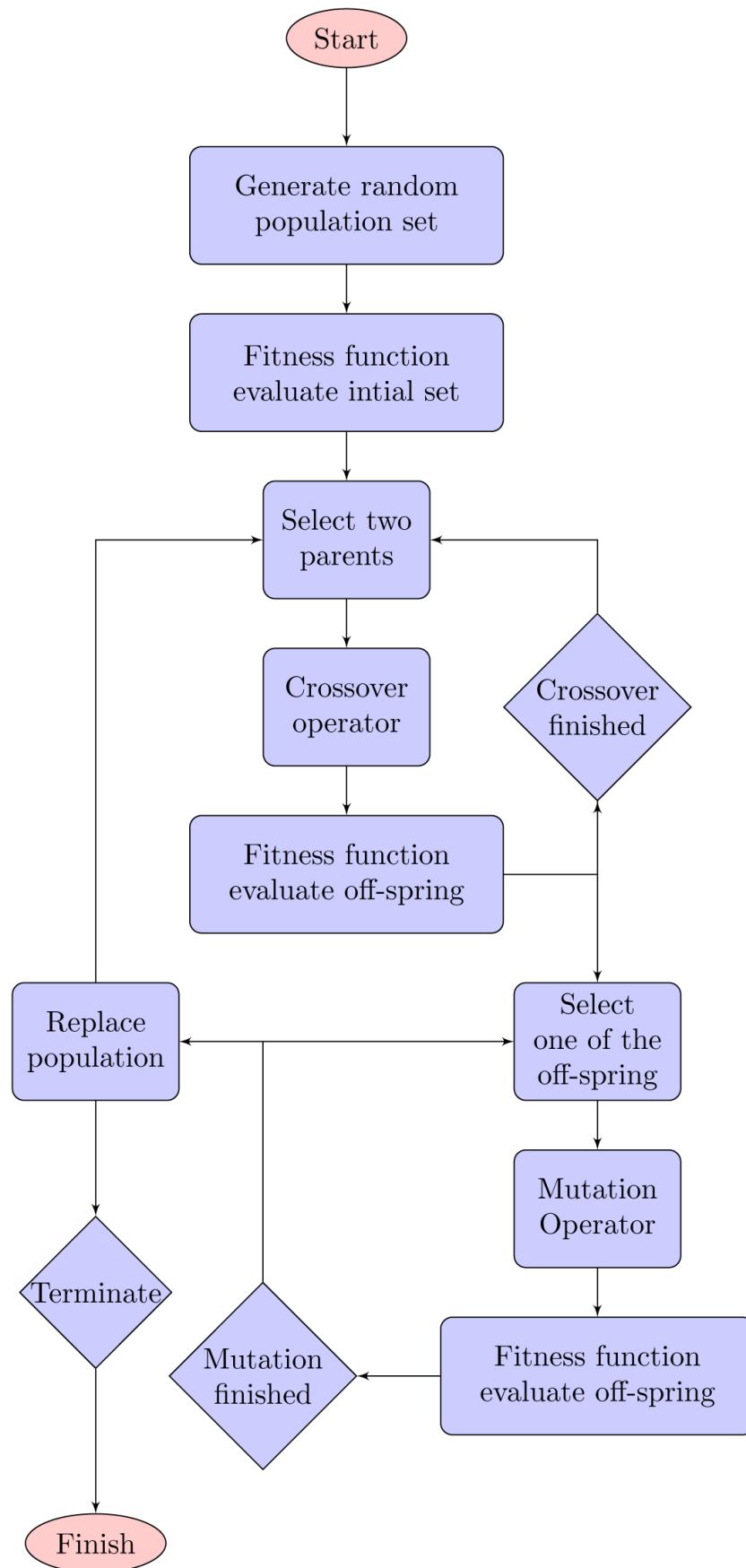
Figure 3.1: Block diagram representation of the GA

- Before the GA operators execute and generate a new generation, the current generation's fitness value will be scaled to a range that is suitable for the selection process. The algorithm will scale the fitness value by rank of n which is $\propto 1/\sqrt{n}$, the rank of each individual is the position that it is stored as. Therefore the rank of the best individual will be 1.

- A new generation is implemented based on the scaled fitness rank of the current generation. The selected parents are obtained by setting the selection function as a stochastic uniform layer. This function will lay out a line, that will consist of each parent within the population, which forms part of a section of the line that corresponds to each parent's fitness value. For the mutation and crossover, the selection function will randomly land on a section of the line and allocate the individual as a parent.

- The elite option is set to 2, which means that out of the current generation 2 elite parents will be set to the new generation, this is based on their fitness scaling.

- After the 2 elite children have been selected, the algorithm performs a crossover based on the crossover fraction, which is 0,8. This means that 80 % of the current population is specified to the crossover function. The new individual is obtained based on the CROSSOVERSCATTERED function in MATLAB's options. This is where a binary vector is created. The first parent's genes are taken where the vector is an '1' representation and the second parent's genes are selected when the vector is a '0'. The two parents genes are then combined into one and a new individual is created.

- Each individual parent is mutated through the random mutation fraction that is chosen from a Gaussian distribution function. The final set of population is not mutated, this is implemented by specifying the shrink option for the GA. Mutation allows for diversity in the population, this increases the likelihood of the next generation of individuals to obtain a better fitness value.

- The function will stop as soon as the stopping criterion is reached, there are a few options for the GA solver. If the generation size is set to 50, the algorithm terminates when the number of generations is reached. If the function tolerance is set to 10^{-6}, the algorithm terminates when the average relative change in the fitness function of the current generation is less than the fitness tolerance.

The limitation of the algorithm is that when a solution is found, it is unclear if the solver has converged to the optimum.

3.5   The FMINSEARCH Algorithm

The FMINSEARCH algorithm is an iterative process that searches for a local minimum of the fitness function. The FMINSEARCH function uses the Nelder-Mead simplex algorithm

given in [19] to determine the search space. This is classified as a deterministic search, which does not use analytical or numerical gradients to form the search space.

The simplex will consist of $n + 1$ points, where there are n-dimensions in the solution vector x. For example, when the problem is a 2-D problem a triangular simplex will be used. For a 3-D problem the simplex will be shaped as a pyramid.

The next subsection will explain how MATLAB implements the simplex algorithm in the FMINSEARCH algorithm.

3.5.1 Matlab Implementation of FMINSEARCH Toolbox

The FMINSEARCH solver defined in MATLAB's optimization toolbox forms a search space based on the simplex algorithm, as discussed in [20]. The algorithm will form a simplex with the initial points and generate a new point by adding 5% to the initial values. If the initial set x_1 is a vector of n dimensions then the algorithm will add 5% to each component in x_i where $i = 1, \ldots, n+1$. The algorithm will find a solution by modifying the initial set of functions until the simplex diameter is less than the specified tolerance. A simplex is implemented by restructuring the point from lowest function value $f(x_1)$ to highest function value $f(x_{n+1})$. The function will discard one of the parameters in the set and generate a new point into the simplex. This is done by exploring the multidimensional landscape through four basic operations which are reflection, expansion, contraction and shrink. Figure 3.2 presents the simplices for a 2-D problem.

The operations are implemented in the following way. The average centroid of n points, for all the vertices except for x_{n+1}, are calculated as follows,

$$x_m = \sum_{i=1}^{n} \frac{x_i}{n}. \tag{3.5.1}$$

Each cycle will generate a reflected point x_r given by,

$$x_r = 2x_m - x_{n+1}, \tag{3.5.2}$$

Terminate the iteration if $f(x_1) \leq f(x_r) \leq f(x_n)$ holds true for all x accept for x_r. If $f(x_r) \leq f(x_1)$ holds true, calculate the expansion point x_e as follows,

$$x_e = x_m + 2(x_m - x_{n+1}). \tag{3.5.3}$$

Terminate the expansion operator if $f(x_e) < f(x_r)$ holds true for all x accept for x_e. Otherwise, terminate the reflect operator if $f(x_e) \geq f(x_r)$ holds true for all x accept for x_r.

If $f(x_r) \geq f(x_n)$, perform the contraction operator between x_m and x_{n+1} or x_r depending on which point is better, evaluated as follows $f(x_r) \geq f(x_n + 1)$. The outside contraction point x_c is calculated as follows,

$$x_c = x_m + \frac{x_r - x_m}{2}. \tag{3.5.4}$$

Terminate the outside contraction operator if $f(x_c) < f(x_r)$ holds true for all x accept the point x_c.

If $f(x_r) \leq f(x_{n+1})$ then the simplex will contract inside and the contraction point x_{cc} is calculated as follows,

$$x_{cc} = x_m + \frac{x_{n+1} - x_m}{2}. \tag{3.5.5}$$

(a) Reflect Operator

(b) Expansion Operator

(c) Contract Outside Operator

(d) Contract Inside Operator

(e) Shrink Operator
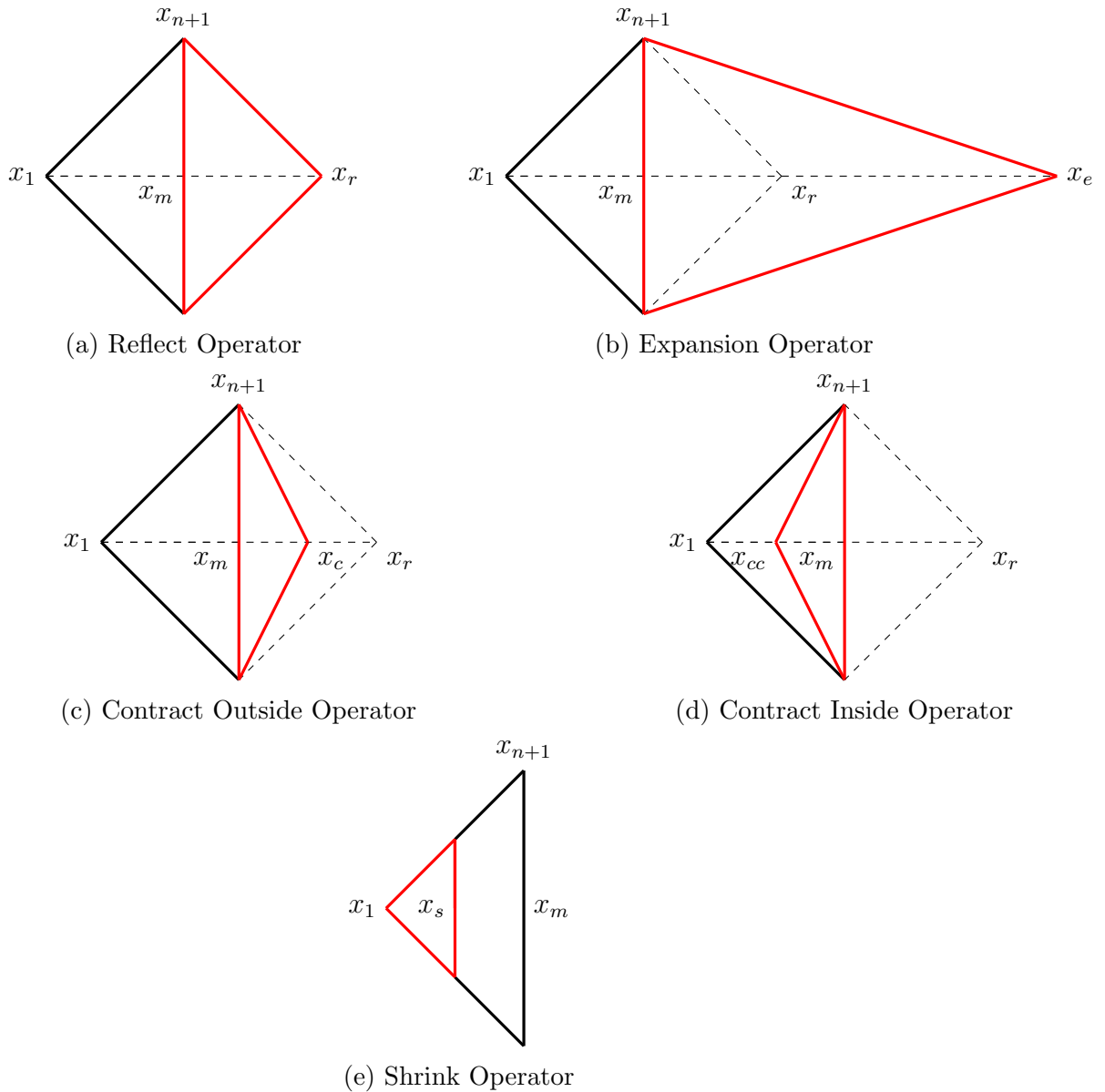
Figure 3.2: The Nelder-Mead simplices, the original simplex is in black and the red simplex represents each operation.

If $f(x_{cc}) < f(x_{n+1})$ then the x_{cc} point is accepted and the inside contraction operation is terminated.

The simplex will compute the shrink operator by calculating n points, which is given as,

$$v_i = x_1 + \frac{x_i - x_1}{2} \qquad \forall i = 2, \ldots, n + 1, \tag{3.5.6}$$

and the new simplex will be given by $x_1, v_2, \ldots, v_{n+1}$.

3.6   Conclusion

The different conventional optimization techniques were discussed in Section 3.2. The fitness function was discussed in Section 3.3, which is used in order to find a fitness value for the solution set.

The GA solver and FMINSEARCH solver were discussed in Section 3.4 and in Section 3.5. The GA solver was implemented in MATLAB, as discussed in Subsection 3.4.2. In Subsection 3.5.1 the FMINSEARCH algorithm was explained.

The GA searches for a global solution to the defined problem whereas it is possible for the FMINSEARCH function to terminate on a local solution. The FMINSEARCH algorithm however obtains a solution set faster than the GA and therefore serves as a better option when the solution set is close to the initial set.

Chapter 4

Multi-Mode Antennas

4.1   Introduction

This chapter discusses the basic concepts of multi-mode antenna systems. A hemispheric radiation pattern can be realized for the quad-mode antenna by effectively utilizing the differential and common mode excitations of the antennas.

Section 4.2 will discuss the quad-mode antenna and the calculation of the antenna's combined gain will be given in Subsection 4.2.3. The simulated radiation patterns of the quad-mode antenna will be presented in Subsection 4.2.1 for the isolated quad-mode antenna and in Subsection 4.2.2 the embedded element pattern will be presented.

Through effectively utilizing each of the four orthogonal excitation modes present on a quadraxial feed-line, a multi-mode network can be obtained that demonstrates an ultra-wide hemispheric FoV coverage for the quad-mode antenna. The optimization and beam-forming techniques used to achieve this will be discussed in Section 4.3.

Section 4.4 compares the quad-mode antenna to another wide-band device, the Short-Circuit Quadrifilar Helix Antenna (S-C QHA), with broadside radiation and circularly-polarized waves. Subsection 4.4.1 introduces the S-C QHA design, and the radiation characteristics and performance are discussed in Subsection 4.4.2.

The chapter will conclude by presenting the transformation techniques used by authors in [3] to convert a network terminated by four multi-mode ports, to a network terminated by four single-ended mode ports, discussed in Section 4.5.

4.2   The Quad-Mode Antenna

The quad-mode antenna was designed by authors in [5] as a possible candidate for the SKA mid or low frequency aperture array. The quad-mode antenna was initially designed with an operating frequency of 1.25 GHz. As the available measuring facility operates effectively above 2 GHz the antenna was redesigned to resonate at 2 GHz and Table (4.1) summarizes the corresponding parameters.

The quad-mode antenna consists of two orthogonal dipoles and a ground shield folded back into a monopole element, as shown in Figure 4.1. Each of the four dipole arms are connected to one of the centre conductors of the quadraxial transmission line. A y-axis cross-sectional representation of the quad-mode antenna and the quadraxial feed line can be observed in Figure 4.2.

As discussed previously, a feeding scheme will be designed in order to excite the quad-

27
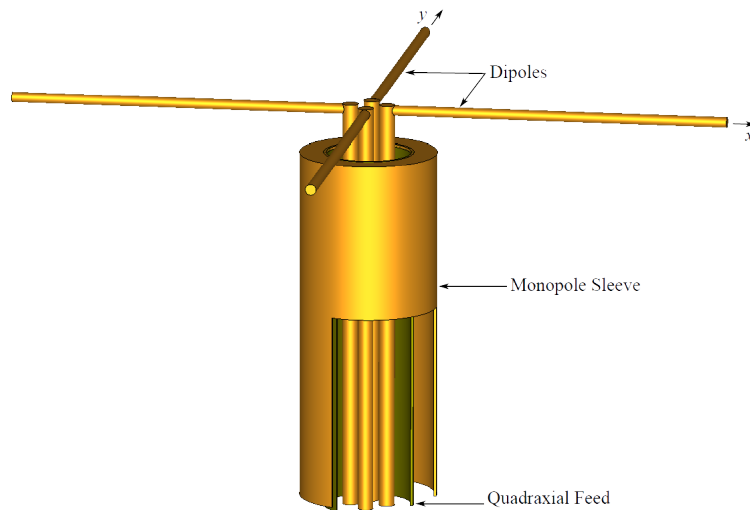
Figure 4.1: 3-D representation of the quad-mode antenna with two orthogonal dipoles and an integrated monopole sleeve [2].
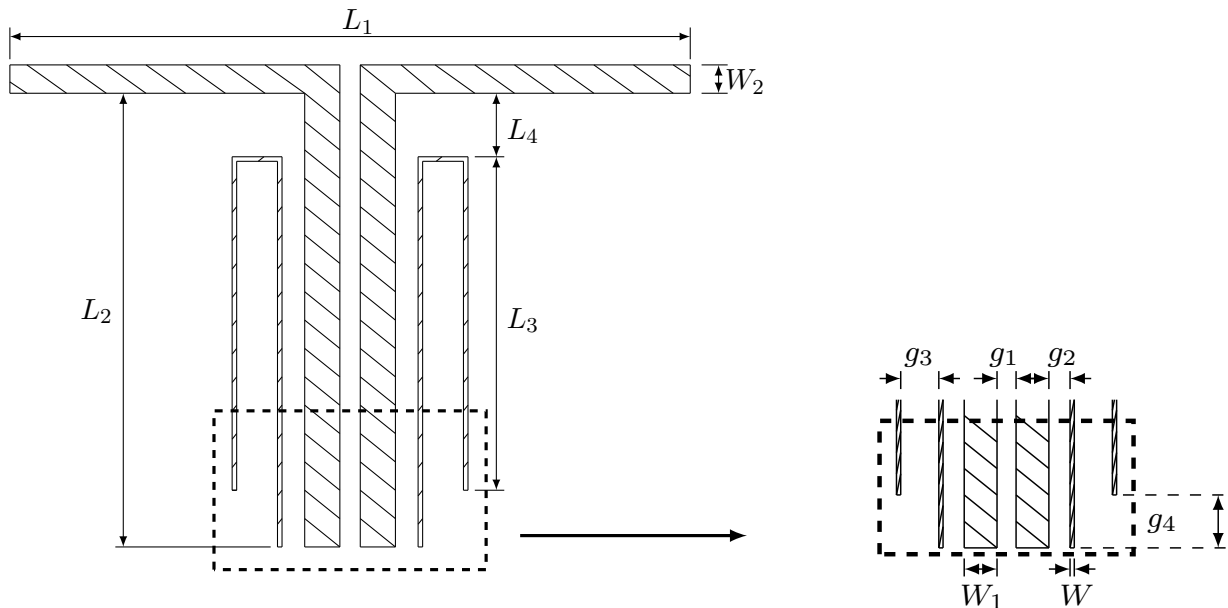
Figure 4.2: 1-D cross-sectional cut of the quad-mode antenna, the corresponding parameter set given in Table 4.1.

mode antenna with one LNA connected to the output. This will be accomplished by obtaining a desirable set of combinational multi-mode excitations that allows for a hemispheric FoV coverage radiation pattern.

These multi-mode excitation sets are of high interest to antenna designers due to the fact that they radiate power independently of one another. The different TEM modes propagate orthogonally on a transmission line and therefore radiate their power independently. In order to fully characterize these multi-mode excitations, a linear superposition of the single-ended mode excitations should be performed.

Parameters	Values [mm]	Description
L_1	78	Dipole length
L_2	40.75	Dipole height above ground
L_3	33	Monopole length
L_4	7	Separation between monopole and dipole
W_1	3	Antenna feed line diameter
W_2	2	Dipole height above ground
W_3	14.5	Ground shield inner diameter
W_4	15.5	Ground shield outer diameter
W_5	23.5	Monopole inner diameter
W_6	24.5	Monopole outer diameter
g_1	2.5	Antenna feed line separation
g_2	3	Separation between antenna feed line and ground shield
g_3	4	Separation between ground shield and monopole
g_4	2	Separation between ground plane and monopole

Table 4.1: The quad-mode antenna design parameters at 2 GHz

4.2.1 Simulation Characteristics of The Isolated Element Pattern

The quad-mode antenna is simulated in CST over an infinite ground plane and the quadraxial feed line is realized by using the multi-pin waveguide port in CST. This is done by correctly defining each multi-mode set of potentials, as shown in Figure 4.3. The figure also depicts the corresponding far-field radiation patterns for the isolated quad-mode antenna.

When excited in the differential modes, as shown in Figures 4.3b to 4.3d, no net current is realized on the monopole and only the two orthogonal dipole radiation patterns are observed, which are denoted as mm_1 and mm_2. A common mode radiation pattern, mm_3, is realized by exciting all four dipole arms in phase, as shown in Figure 4.3f. Figure 4.3h depicts the radiation pattern of the fourth mode mm_4, where the power radiates diagonally to the orientation of the dipole arms.

The simulated multi-mode reflection coefficients for the isolated quad-mode antenna are shown in Figure 4.5b. The differential mode and common mode are well matched at the operating frequency of 2 GHz, whereas for the fourth mode mm_4, has a large mismatch. Furthermore, from this figure the symmetry of the structure on the x- and y-axis can be seen by observing that the return losses of the two crossed dipole excitation sets are the same.

The antenna structure is modelled and optimized in terms of its multi-mode sets. In order to fully characterize the multi-mode network the corresponding single-ended network needs to be derived. This will be discussed in Section 4.5. The single-ended ports are simulated in CST using four single-ended excitation modes, given in Figure 4.4. Also depicted in Figure 4.4 are the corresponding far-field distributions for the isolated quad-mode antenna.

(a) mm_1 Port

(b) mm_1

(c) mm_2 Port

(d) mm_2

(e) mm_3 Port

(f) mm_3

(g) mm_4 Port

(h) mm_4

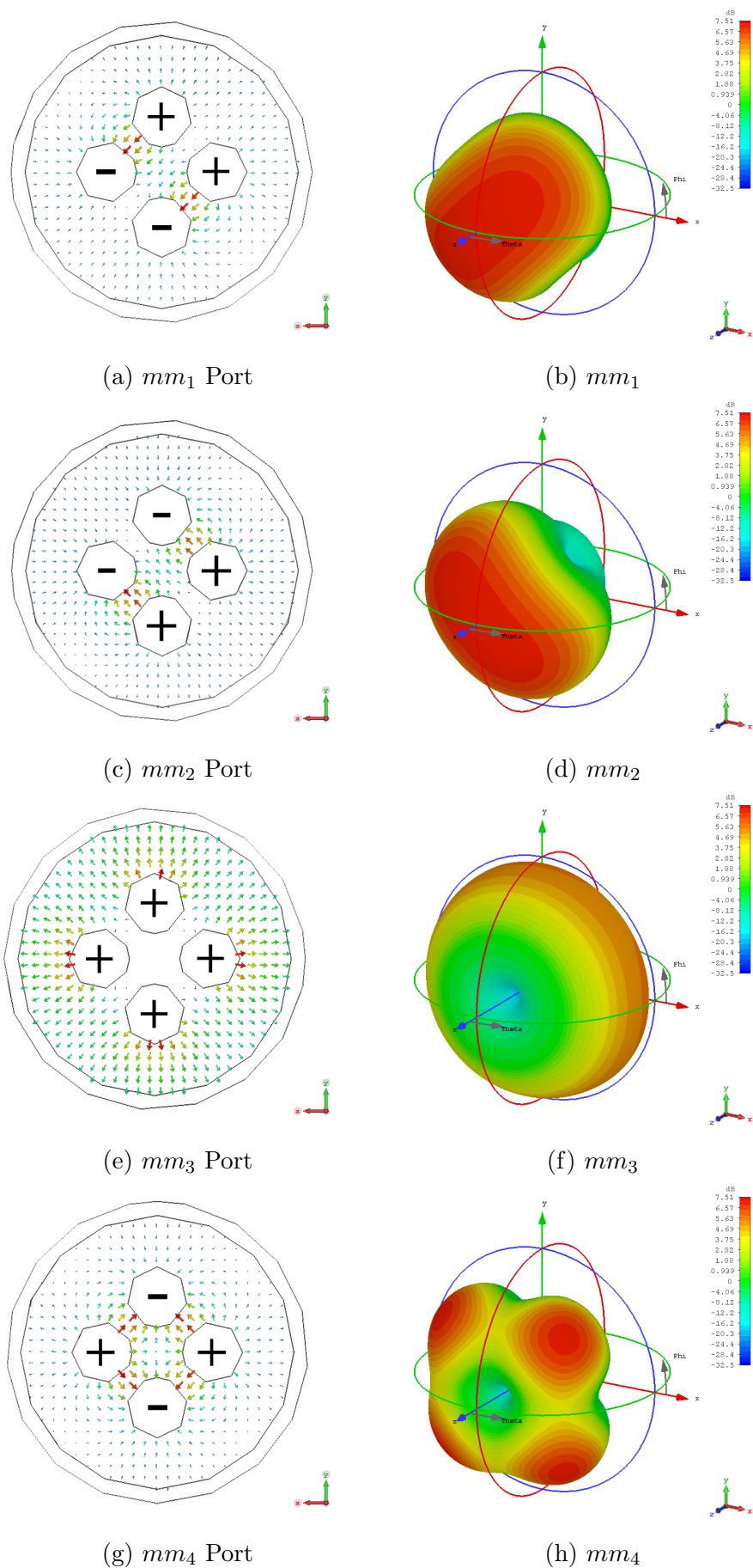Figure 4.3: The multi-mode far-field radiation pattern and electric field distributions of each port modes; mm_1 and mm_2, mm_3 and mm_4.

(a) se_1 Port

(b) se_1

(c) se_2 Port

(d) se_2
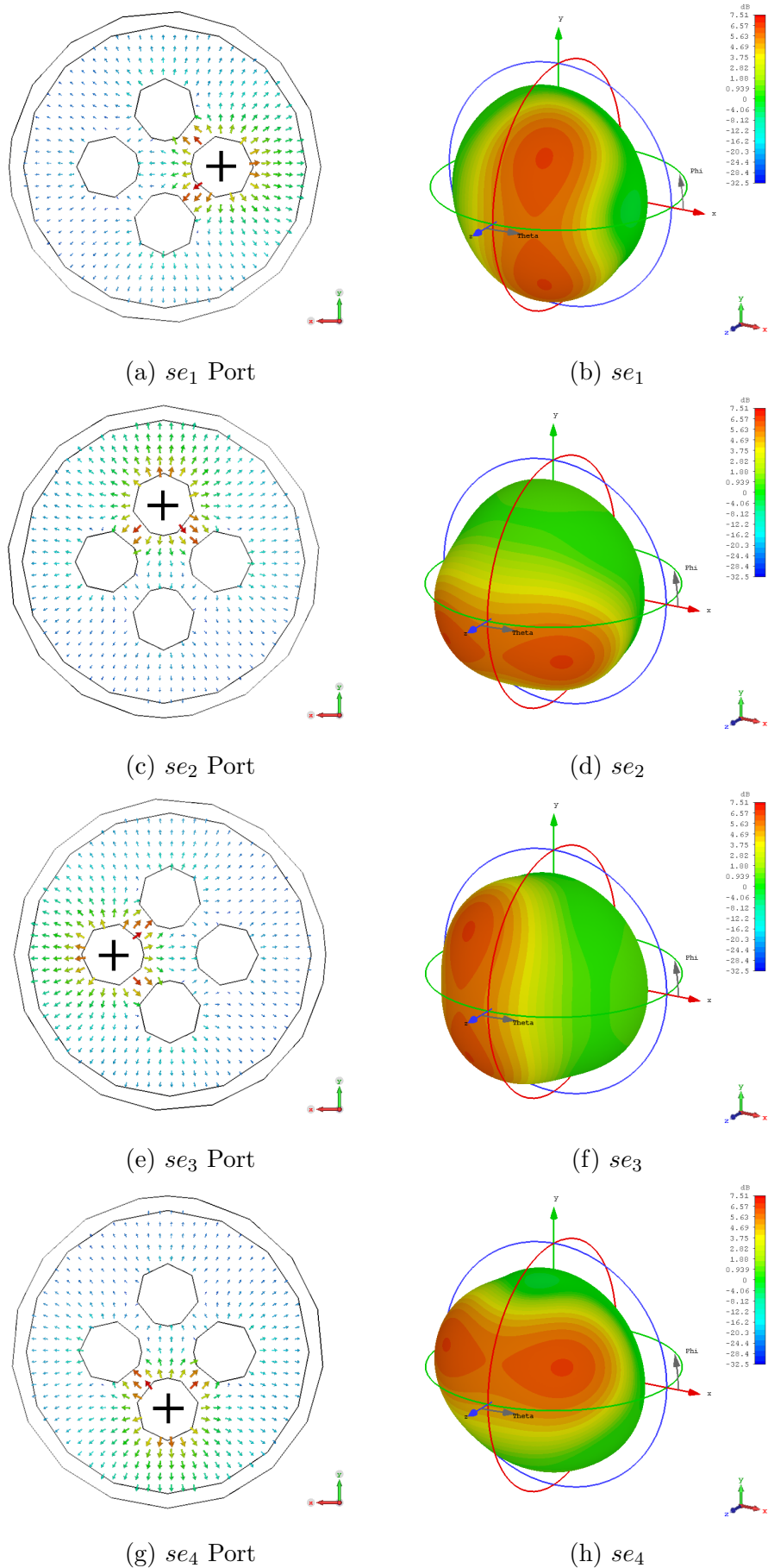
(e) se_3 Port

(f) se_3

(g) se_4 Port

(h) se_4

Figure 4.4: The single-ended far-field radiation pattern and electric field distributions of each port modes; se_1, se_2, se_3 and se_4.

(a) The embedded element pattern
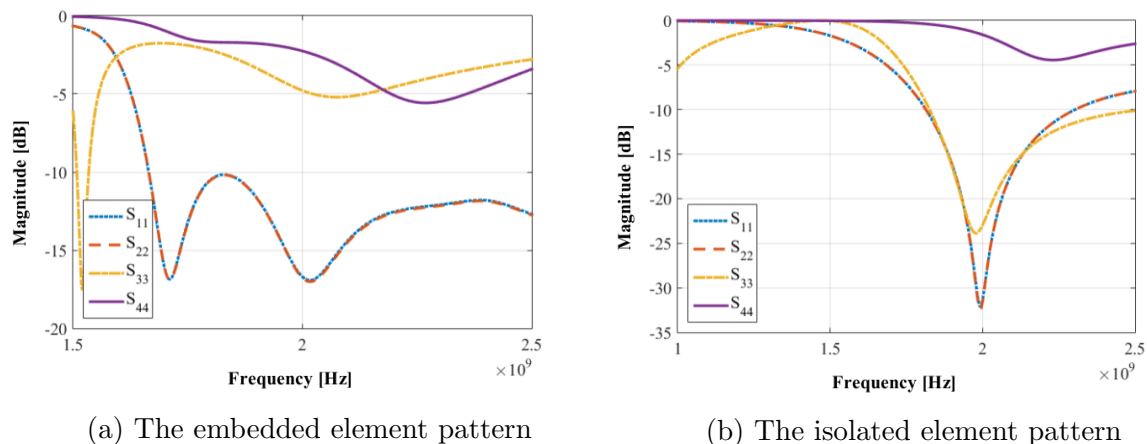
(b) The isolated element pattern

Figure 4.5: The S-parameters of the multi-mode ports for; (a) the embedded element pattern and (b) the isolated element pattern.

4.2.2 Simulation Characteristics of The Embedded Element Pattern

The embedded element or active element pattern is an important characteristic that needs to be considered when designing a phased array system, and is not applicable to a single antenna element. The embedded element pattern, as defined in Chapter 2, is the radiation pattern of an array element when all other elements have been terminated with a matched load.

The quad-mode antenna will be placed in a 2×2 phased array configuration and optimized for maximum gain at each scanned angle over the hemisphere, which is discussed in Chapter 6. When the quad-mode antenna is placed in an array configuration, high parasitic conditions are shown in CSTs far-field array application. The far-field array calculates an approximation of the entire array using the pattern multiplication property. The application rescales the array far-field pattern by setting the array radiation efficiency equal to the radiation efficiency of a single antenna. When significant rescaling occurs, the array indicates strong mutual coupling effects between the elements and especially between similar modal excitations. Therefore the embedded element pattern is simulated in CST and used for calculating the array radiation pattern in Chapter 6.

The embedded element pattern is simulated in CST using the periodic boundary conditions application. The periodic boundary condition application in CST simulates a periodic expansion of the antenna element with a defined phase shift between each new element. The radiation pattern of an antenna element within an array configuration changes as the beam is scanned over the entire FoV. Therefore when scanning the beam pattern of the array, the scanned angle property is set in the periodic boundary condition application. The simulated antenna model calculates the nearby field effects that are caused by the neighbouring elements. The antenna is therefore simulated as if it has been placed in an infinitely large array and the extracted radiation pattern is known as the embedded element pattern. It is important to note that in a 2×2 array configuration all four antennas are edge-elements, and using the embedded element array within this configuration only an approximation of the actual array pattern is obtained.

Figure 4.6 illustrates the far-field embedded element patterns of the four multi-mode excitations as, mm_1^E, mm_2^E, mm_3^E and mm_4^E simulated in CST at 2 GHz, over an infinite ground plane. Also shown in Figure 4.6 are the far-field embedded element patterns of

the four single-ended modes, se_1^E, se_2^E, se_3^E and se_4^E.

The author in [9] discusses that the embedded element pattern includes the parasitic effect that is caused by neighbouring elements. Therefore the embedded element pattern is a more accurate model for the purposes of conducting array scanning analysis compared to the isolated element pattern. Figure 4.5a depicts that the active reflection coefficient for the embedded element pattern is not matched well for the different modal excitations of the quad-mode antenna, especially the common mode excitation and the fourth mode excitation.

The coupling effects between elements will be considered but not compensated for.

4.2.3   The Element Combined Gain Calculation

The quad-mode antenna can be considered as a four element array, where each multi-mode set is modelled as a separate, but co-located, array element. Therefore array theory can be applied and the quad-mode antenna combined gain can be computed. The far-field radiation patterns of the four modes are extracted from CST in spherical coordinates as $rf_{mm_n}^\theta$ and $rf_{mm_n}^\phi$, with RMS-values given as V_{RMS}/m. The total combined electric fields of the quad-mode antenna can be calculated by summing the weighted four multi-modes. The total spherical electric field θ- and ϕ- components are calculated using vector notation as follows,

$$\mathbf{F}(\theta, \phi) = \sum_{n=1}^{4} f_{mm_n}^\theta(\theta, \phi) w_{mm_n} + \sum_{n=1}^{4} f_{mm_n}^\phi(\theta, \phi) w_{mm_n}. \tag{4.2.1}$$

After the set of weights, $\mathbf{w} = [w_{mm_1}, \ldots, w_{mm_4}]^T$, are applied to each set of multi-mode electric field $f_{mm_n}^\theta$ and $f_{mm_n}^\phi$ components. The radiation intensity, given in Equation (2.2.3), is calculated for the quad-mode antenna in free space as,

$$\mathrm{U}(\theta, \phi) = \frac{1}{\eta} \sum_{n=1}^{4} \left[|f_{mm_n}^\theta(\theta, \phi) w_{mm_n}|^2 + |f_{mm_n}^\phi(\theta, \phi) w_{mm_n}|^2 \right], \tag{4.2.2}$$

where $\eta = 377$ for free space impedance. The scattering matrix of the quad-mode antenna is calculated in CST and is given by,

$$\mathbf{S} = \begin{bmatrix} S_{11} & S_{12} & S_{13} & S_{14} \\ S_{21} & S_{22} & S_{23} & S_{24} \\ S_{31} & S_{32} & S_{33} & S_{34} \\ S_{41} & S_{42} & S_{43} & S_{44} \end{bmatrix}. \tag{4.2.3}$$

An equivalent model is given in Figure 4.7 of the multi-mode network of the quad-mode antenna feed ports which are characterized by the scattering matrix and the complex value of the incident and reflected waves as follows,

$$\mathbf{b} = [\mathbf{S}][\mathbf{w}]. \tag{4.2.4}$$

The total radiated power of the quad-mode antenna is expressed as

$$P_{rad} = P_{max} - P_{reflected}, \tag{4.2.5}$$

(a) se_1^E

(b) mm_1^E

(c) se_2^E

(d) mm_2^E

(e) se_3^E

(f) mm_3^E
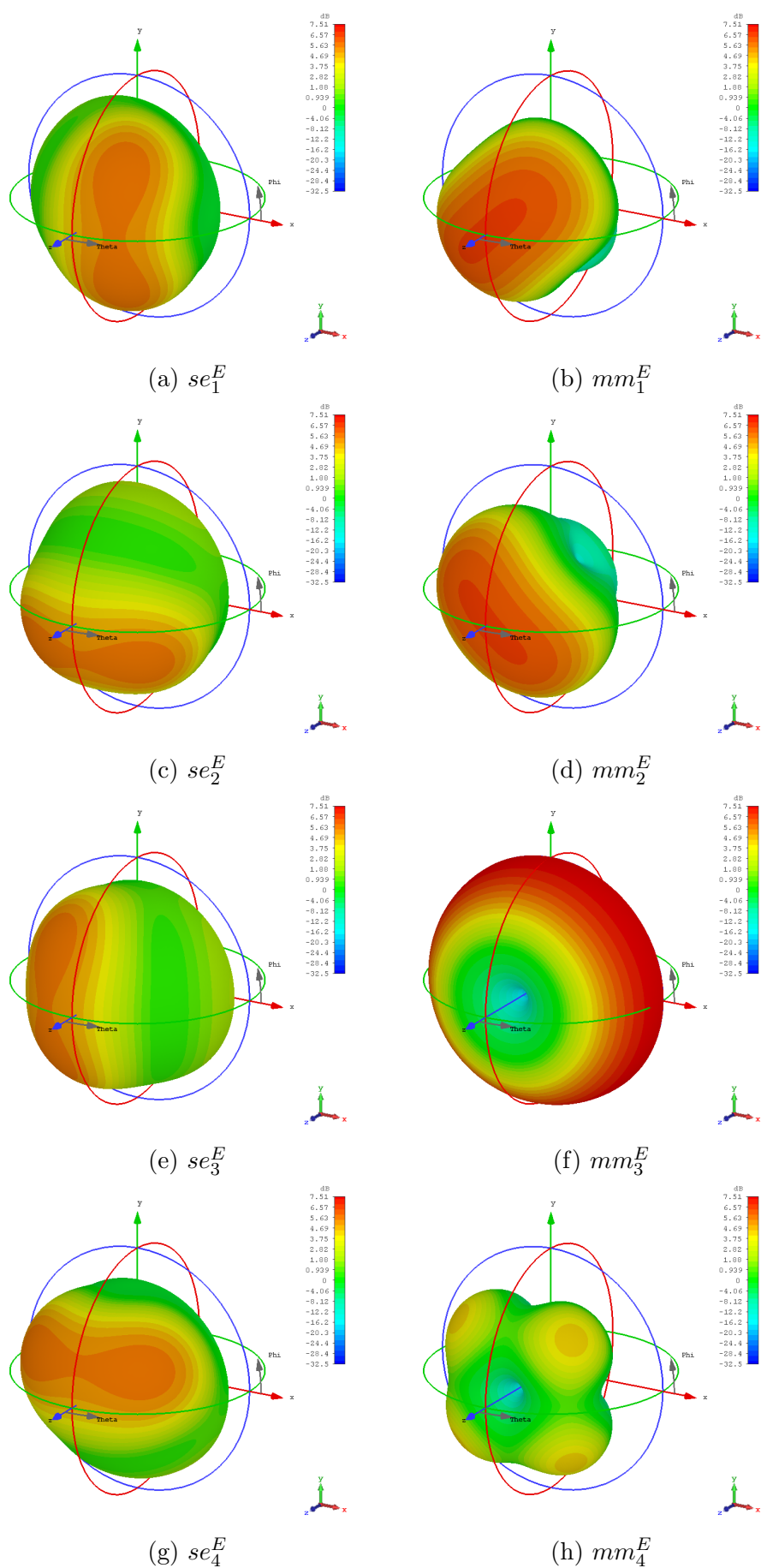
(g) se_4^E

(h) mm_4^E

Figure 4.6: The embedded element multi-mode and single-ended mode far-field radiation pattern.
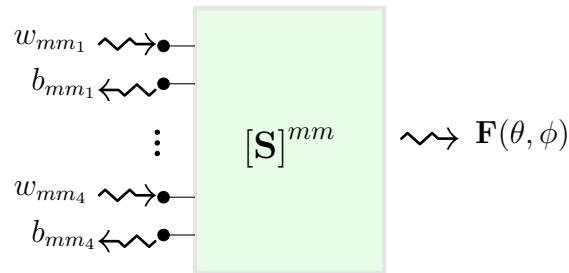
Figure 4.7: Multi-mode network representation of the quad-mode antenna feed ports.

which is the maximum power minus the total reflected power. Using Equation (4.2.4) the total radiated power is calculated as,

$$P_{rad} = \sum_{n=1}^{4} [(|w_{mm_n}|^2) - (|b_{mm_n}|^2)],$$
$$= \mathbf{w}^H \mathbf{w} - \mathbf{b}^H \mathbf{b}. \tag{4.2.6}$$

which can be simplified by substituting Equation (2.4.6) into Equation (4.2.6) that reduces to,

$$P_{rad} = \mathbf{w}^H [I - \mathbf{S}(\mathbf{S})^H] \mathbf{w}, \tag{4.2.7}$$

where H is the Hermitian transpose. Assuming that the antenna is operating in a lossless system, the combined gain can be calculated as follows,

$$G(\theta, \phi) = 4\pi \frac{U(\theta, \phi)}{P_{rad}},$$
$$= \frac{4\pi}{\eta} \frac{\sum_{n=1}^{4} \left[|f_{mm_n}^\theta(\theta, \phi) w_{mm_n}|^2 + |f_{mm_n}^\phi(\theta, \phi) w_{mm_n}|^2 \right]}{\mathbf{w}^H [I - \mathbf{S}(\mathbf{S})^H] \mathbf{w}}. \tag{4.2.8}$$

By varying different combinational sets of the weighting functions $\mathbf{w}$, a hemispheric beam pattern can be obtained for the quad-mode antenna. This will be shown in Section 4.3, where an optimal weighted combination of all four modes will be discussed.

4.3   Optimize a Hemispherical Field-Of-View of the Quad-Mode Antenna

Three optimization techniques are considered in this section; the maximum-gain beamforming theorem, the GA optimization and the FMINSEARCH optimization. Firstly, the maximum-gain beamforming theorem is applied and the complex beamforming weights $\mathbf{w}$ are solved for maximum gain over the FoV. Additionally, the GA optimization and FMINSEARCH tool-kits in the MATLAB environment, will be used to optimize the sets of $\mathbf{\Upsilon}_{mm}$ and $\boldsymbol{\varrho}_{mm}$ excitations for a hemispheric beam pattern, respectively.
The weighting scheme applied to the maximum-gain theorem solves for the complex conjugate weights which satisfy the conjugate-field matching condition, as discussed in Section 2.5. Whereas the GA and the FMINSEARCH solve the set of excitations through optimization techniques.

4.3.1 Beamforming Implementation

The isolated quad-mode antenna is used for beamforming the multi-mode excitations over the hemispheric FoV coverage. The four modes excited through the quadraxial feed line radiate orthogonally, these excitation modes are modelled as a four element array where each mode is represented as a separate element within the array.

By constructively utilising all four modes a maximum gain pattern is obtained at each scanned angle over the hemisphere. The complex beamformer weights, $\mathbf{w}^H = [w_{mm_1}^*, \ldots, w_{mm_4}^*]$, are solved for by using the maximum-gain beamforming theorem, discussed in Section 2.5. This is done by converting the defined quad-mode antenna gain, given in Equation (4.2.8), to its equivalent matrix vector as follows,

$$G(\theta, \phi) = \frac{4\pi}{\eta} \frac{\mathbf{w}^H \mathbf{F} \mathbf{F}^H \mathbf{w}}{\mathbf{w}^H [\mathbf{B}] \mathbf{w}}, \qquad (4.3.1)$$

where $\mathbf{B} = [I - \mathbf{S}[\mathbf{S}]^H]$. The electric field vector of the isolated quad-mode antenna's multi-mode network is given in a two-dimensional vector by,

$$\mathbf{F}^{mm} = \begin{bmatrix} f_{mm_1}^\theta(\theta_0, \phi_0) & f_{mm_1}^\phi(\theta_0, \phi_0) \\ \vdots & \vdots \\ f_{mm_4}^\theta(\theta_0, \phi_0) & f_{mm_4}^\phi(\theta_0, \phi_0) \end{bmatrix}, \qquad (4.3.2)$$

where θ_0, ϕ_0 is the desired angular direction. Taking the partial derivative of Equation (4.3.1) with respect to $\mathbf{w}^H$ and equating the determinate to zero, yields Equation (4.3.3).

$$\mathbf{F} \mathbf{F}^H \mathbf{w} = \frac{\eta}{4\pi} G(\theta, \phi) [\mathbf{B}] \mathbf{w}. \qquad (4.3.3)$$

Obtaining the largest eigenvalue of Equation (4.3.3) the complex beamformer weights are solved as the conjugate eigenvector which results in the maximum gain at each scanned angle over the hemisphere. Figure 4.9 illustrates the maximum gain achieved for each solved set of $\mathbf{w}$ for a hemispheric FoV coverage. A gain variation of less than 3 dBi is achieved.

4.3.2 Pattern Optimization using the Genetic Algorithm

The isolated quad-mode antenna pattern is optimized for wide FoV coverage through the implementation of the GA.

The GA effectively searches for a solution that gives a global minimum. As discussed in Subsection 3.4.1, a fitness function defines the problem and establishes a relationship between the GA and the problem. The function evolves an optimal set of solutions by evaluating the performance of each solution set the algorithm produces.

As previously mentioned the quad-mode antenna has four modes, each with their respective weight $\mathbf{\Upsilon}_{mm} = [\Upsilon_{mm_1}, \ldots, \Upsilon_{mm_4}]$. A hemispheric beam pattern is obtained by optimizing this set of weights through minimizing the fitness value defined in the fitness function.

In this case the fitness of each set is defined by the maximum gain, of the isolated quad-mode antenna gain defined in Equation (4.2.8), minus the minimum gain of the isolated quad-mode antenna's radiation pattern which is,

$$G_{max} = \max_{\theta,\phi} G(\theta, \phi),$$
$$G_{min} = \min_{\theta,\phi} G(\theta, \phi), \qquad (4.3.4)$$

over the hemisphere of $0° \leq \theta \leq 90°$ and $0° \leq \phi \leq 360°$. The fitness value is then given as,

$$\min_{\Upsilon} F = G_{max} - G_{min}. \tag{4.3.5}$$

The algorithm is terminated when the best fitness value over the generation is smaller or equal to the last iteration. The stopping criteria is predefined in MATLAB for the GA, as discussed in Subsection 3.4.1. The normalized set of Υ_{mm} that achieves a hemispheric beam pattern is given by,

$$\begin{bmatrix} \Upsilon_{mm_1} \\ \Upsilon_{mm_2} \\ \Upsilon_{mm_3} \\ \Upsilon_{mm_4} \end{bmatrix} = \begin{bmatrix} 0.7\underline{/-45°} \\ 0.7\underline{/45°} \\ 1\underline{/0°} \\ 0 \end{bmatrix}. \tag{4.3.6}$$

The two dipole sets of excitations have a phase delay of $90°$ and a $45°$ delay between the monopole set of excitation and the fourth mode is null.

4.3.3   Pattern Optimization using the FMINSEARCH Optimizer

The isolated quad-mode antenna pattern is optimized for wide FoV coverage through the implementation of the FMINSEARCH.

The FMINSEARCH optimizer is an iterative process that will minimize the fitness value, as discussed in Section 3.5. The FMINSEARCH solver use the Nelder-Mead simplex algorithm to optimize the set of weights. The complex weighting functions $\boldsymbol{\varrho}_{mm} = [\varrho_{mm_1}, \dots, \varrho_{mm_4}]$ is optimized.

A quad-mode antenna gain pattern is used for the optimization. Using the maximum and minimum gain defined in Equation (4.3.4) the fitness value is given as,

$$\min_{\boldsymbol{\varrho}} F = G_{max} - G_{min}. \tag{4.3.7}$$

The normalized set of multi-mode excitations obtained are,

$$\begin{bmatrix} \varrho_{mm_1} \\ \varrho_{mm_2} \\ \varrho_{mm_3} \\ \varrho_{mm_4} \end{bmatrix} = \begin{bmatrix} 0.5\underline{/4°} \\ 0.5\underline{/4°} \\ 1\underline{/0°} \\ 0.7\underline{/-20°} \end{bmatrix}. \tag{4.3.8}$$

4.3.4   The Simulated Radiation Patterns

The embedded and isolated quad-mode antenna patterns are depicted in Figure 4.8 for both $\boldsymbol{\Upsilon}_{mm}$ and $\boldsymbol{\varrho}_{mm}$ solution sets. The $\boldsymbol{\Upsilon}_{mm}$ set results in a gain variation of 4.7 dBi and 4.5 dBi for the embedded element pattern and the isolated quad-mode antenna, respectively.

For the $\boldsymbol{\varrho}_{mm}$ set, the embedded element pattern has a gain variation of 4.2 dBi and the isolated pattern shows a gain variation of 1.7 dBi.

The two simulated patterns are different due to the parasitic conditions that the embedded element pattern accounts for, which lowers the overall gain performance of the

quad-mode antenna. The gain variation drops by 0.2 dBi for the $\boldsymbol{\Upsilon}_{mm}$ and 2.5 dBi for the $\boldsymbol{\varrho}_{mm}$. By comparing Equations (4.3.6) and (4.3.8), it can be seen that the $\boldsymbol{\varrho}_{mm}$ set excites the ϱ_{mm_4} mode out of phase from the other modes, thereby distorting the gain pattern.

The results show that, by using the quad-mode antenna $\boldsymbol{\varrho}_{mm}$ set in an array configuration, coupling between similar modes would occur and degrade the array gain performance.

The maximum-gain theorem solve multiple sets **w** for each scanned angle over a hemispheric FoV coverage. The quad-mode antenna obtains a maximum gain at each scanned angle over the hemisphere when excited by these solved sets of beamforming weights. The maximum gain of each set of weights are illustrated in Figure 4.9 at each scanned angle over the hemisphere.

Figure 4.10 illustrates the 1-D gain patterns of the equivalent $\boldsymbol{\Upsilon}_{mm}$ and $\boldsymbol{\varrho}_{mm}$ sets and the maximum-gain theorem results, for a ϕ-cut at 0°. The maximum-gain theorem solves the sets of multi-mode weighting functions that achieve the highest maximum gain values at each scanned angle over the hemisphere. Figure 4.10 shows that the two sets of optimized weighting functions simulates a lower gain pattern than the sets of multi-mode weighting functions solved using the maximum-gain theorem, over the hemisphere. It can also be concluded from Figure 4.10 that the $\boldsymbol{\varrho}_{mm}$ set gives an approximately constant gain variation.

4.4 FoV comparison between quad-mode antenna and the Short-Circuit Quadrifilar Helix Antenna

This section will discuss the comparisons between two ultra-wide FoV coverage antennas, the quad-mode antenna and S-C QHA.

As mentioned in the previous section, the $\boldsymbol{\varrho}_{mm}$ set obtains a variation of 1.7 dBi for the isolated quad-mode antenna pattern, which exhibits an almost isotropic radiation pattern. The S-C QHA consists of four helical windings oriented 90° apart. By exciting all four arms with equal amplitude and quadrature phase, a maximum gain of 5.26 dBi is obtained with an overall gain variation of 10.63 dBi is simulated in CST.

4.4.1 The Short-Circuit Quadrifilar Helix Antenna

Figure 4.11 shows the S-C QHA where the resonant fractional turn within each of the four helical element results in a cartoidal beam pattern with circular polarization. These antennas are widely used in mobile communications, space communications and satellite systems. The S-C QHA consists of two orthogonally placed bifilar helices that are shorted at the top. In [21], Kilgus proves that a bifilar helix antenna has a similar current distribution to a loop-dipole. The S-C QHA is modelled in [21] and the electrical field distribution is calculated. Furthermore, Kilgus shows a maximum gain can be obtained along the axis by feeding the S-C QHA in phase quadrature.

4.4.2 Radiation Characteristics and Performance

The S-C QHA is simulated in CST over an infinite ground plane at 2 GHz. Exciting each helical port with an equal amplitude and a phase shift of 0°, 90°, 180°, 270° respectively, results in an approximately hemispheric radiation pattern as illustrated in Figure 4.12a.

(a) The Υ_{mm} set, the embedded pattern.

(b) The Υ_{mm} set, the isolated pattern.

(c) The ϱ_{mm} set, the embedded pattern.

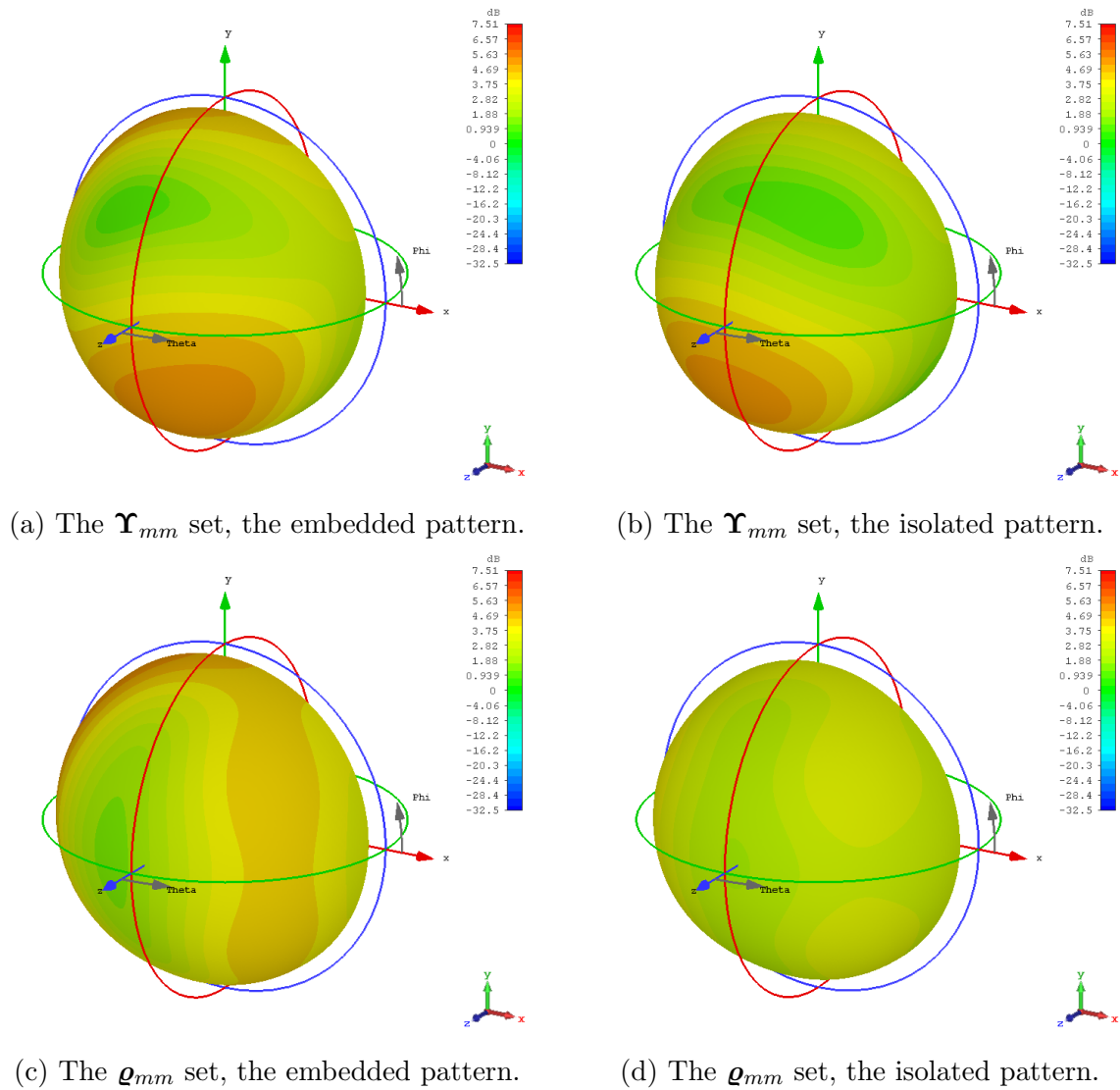(d) The ϱ_{mm} set, the isolated pattern.

Figure 4.8: 3-D Gain patterns in $[dB]$ of the isolated and embedded quad-mode antenna pattern for the multi-mode excitation sets of ϱ_{mm} and Υ_{mm}.
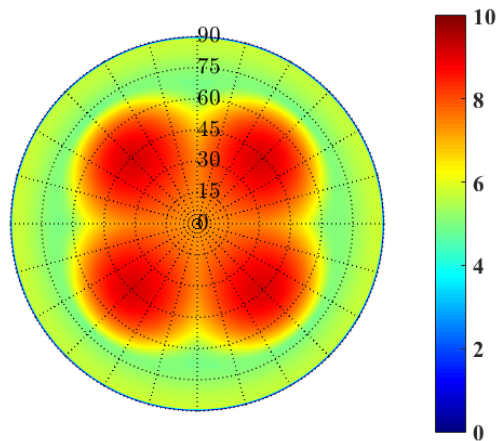

Figure 4.9: The maximum gain for the quad-mode antenna over the hemispheric FoV coverage.
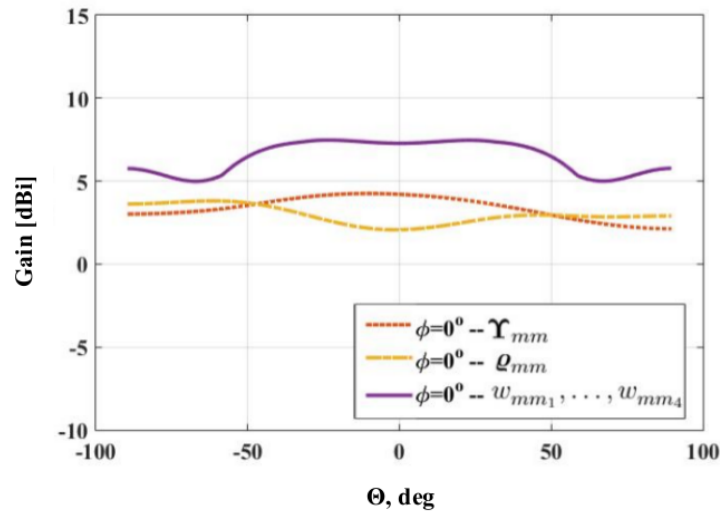
Figure 4.10: The maximum-gain theorem compared with the simulated isolated quad-mode antenna Υ_{mm} and ϱ_{mm} sets.
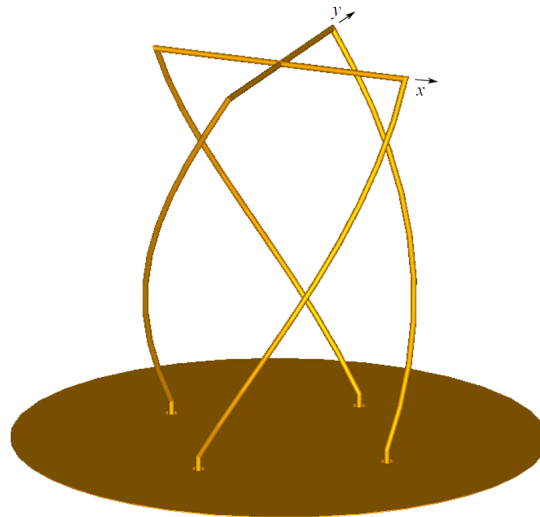

Figure 4.11: The Short-Circuit Quadrifilar Helix Antenna

A maximum gain of 5.3 dBi and a minimum gain of -5.4 dBi are obtained, resulting in an overall gain variation of 10.7 dBi over the hemispheric FoV.

Various innovative feeding networks that are able to excite the antenna in phase quadrature exist. For example, a 180° hybrid connected to a 3 dB quadrature hybrid can be connected to the four ports of the S-C QHA feed points.

The radiation pattern, polarization, and input impedance of the S-C QHA can be controlled by a simple parameter adjustment. A more hemispheric beam pattern can be obtained by choosing the helix circumference in wavelengths to be $C_\lambda < 0.75$ and by extending the length of the helices to be longer than a half-wavelength, as shown in Figure 4.12b. The antenna exhibits a maximum gain of 4.6 dBi and an overall gain variation of 7.4 dBi. The gains of two S-C QHA are compared in Figure 4.13 at $\phi = 0°$. The longer S-C QHA has less overall gain variation but the antenna's dimensions are not manufacturable, with a helix radius of 5.6 mm. The gains of the simulated quad-mode antenna ϱ_{mm} set and the S-C QHA are compared at $\phi = 0°, 45°, 90°$, as shown in Figures 4.14a-4.14c respectively. The quad-mode antenna demonstrates 1.7 dBi gain variation in

(a) S-C QHA   (b) S-C QHA with longer helical windings
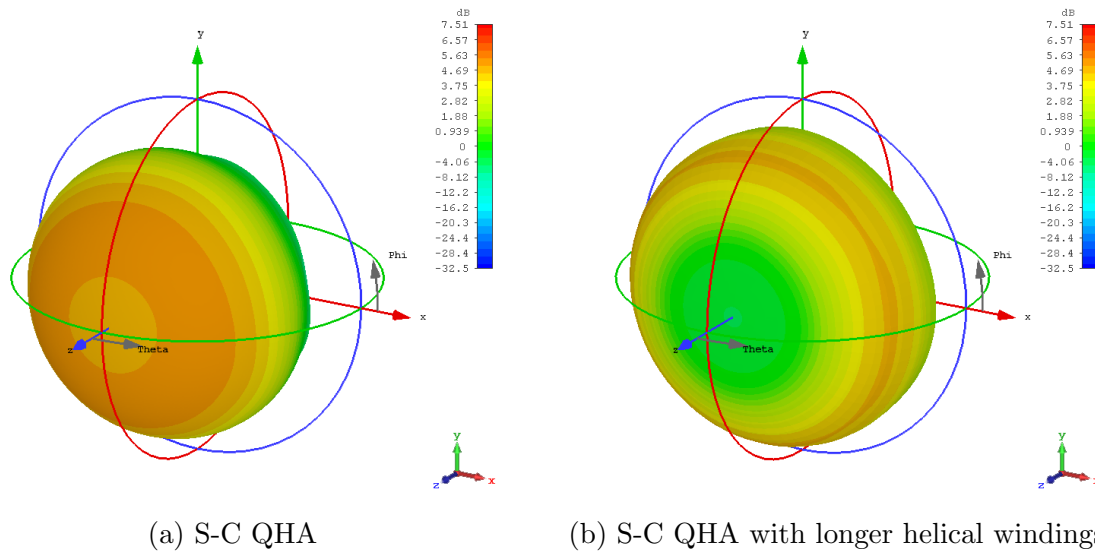
Figure 4.12: 3-D gain pattern of the; (a) S-C QHA and (b) S-C QHA with longer helical windings, simulated in CST at 2 GHz
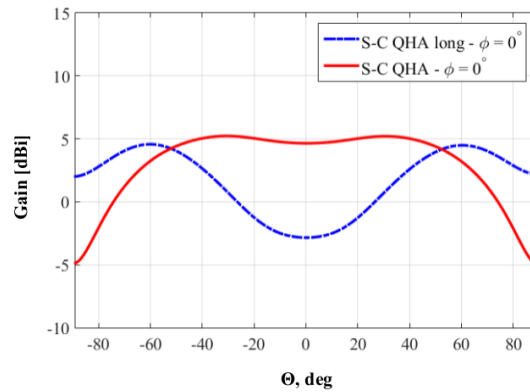
Figure 4.13: The gain of a S-C QHA; which has a smaller radius, longer helical windings and where the windings are approximately half-wavelength, taken at $\phi = 0°$

the overall beam pattern.

4.5   Transformations of a Multi-Mode Network to a Single-Ended Network

To perform measurements on a multi-mode antenna is a difficult task and unnecessary when a multi-mode network can be fully characterized by its equivalent single-ended network. A general technique is presented in [3] to allow for the transformation of a network terminated by four multi-mode ports to a network terminated by four single-ended mode ports. Subsection 4.5.1 describes how the port voltages and currents on one network can be derived from a linear combination of the voltages and currents on another network.
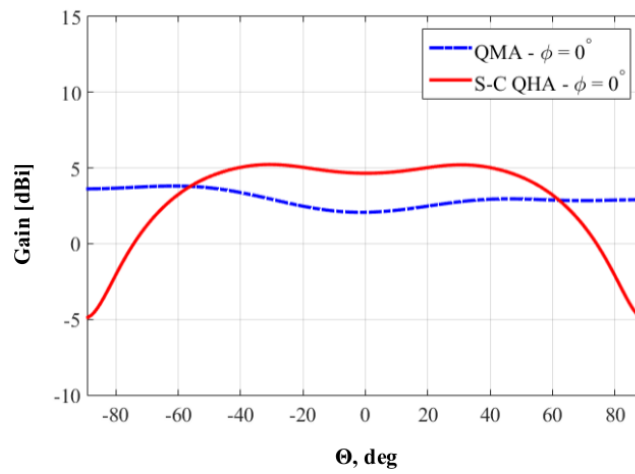
(a) Gain pattern of the quad-mode antenna and S-C QHA at $\phi = 0°$.
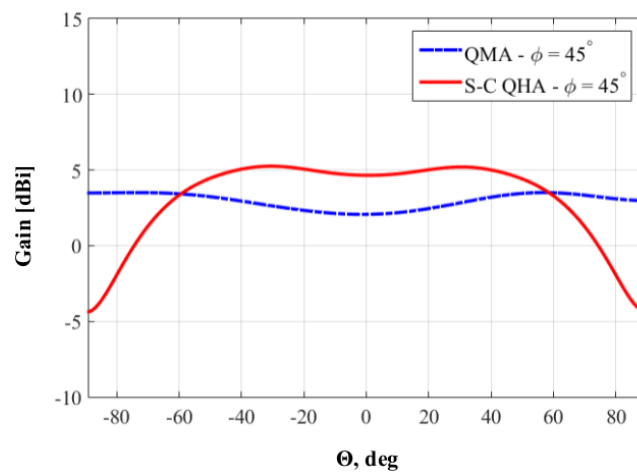
(b) Gain pattern of the quad-mode antenna and S-C QHA at $\phi = 45°$.
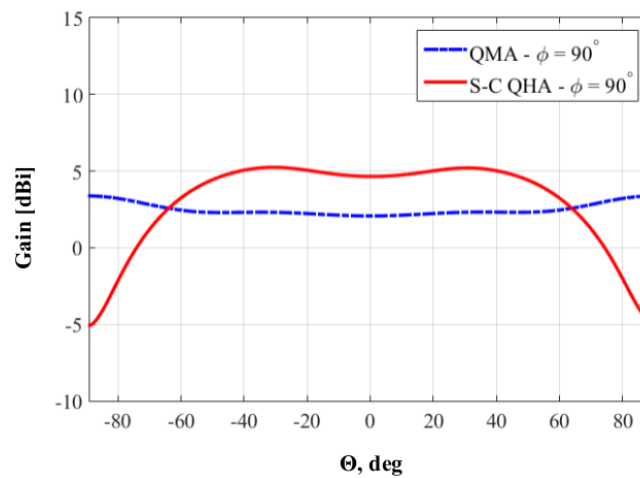
(c) Gain pattern of the quad-mode antenna and S-C QHA at $\phi = 90°$.

Figure 4.14: 1-D gain pattern of the quad-mode antenna (QMA) and S-C QHA at ϕ-cuts.

4.5.1   Generalised S-Parameters Transformations of the Quad-Mode Antenna

The S-parameters transformation technique, discussed in [3], will be used for the transformation of an N-port network, as shown in Figure 4.16. The network is excited in two different ways to form two equivalent N-port networks, single-ended and multi-mode.
The $\mathbf{S}^{mm}$ network can be transformed into its equivalent $\mathbf{S}^{se}$ network by using the S-parameter transformation. The S-parameter transformation can only be applied if the port voltages V_n^{mm} and port currents I_n^{mm} of the multi-mode network can be written as a linear combination of the port voltages V_n^{se} and port currents I_n^{se} of the single-ended network.
In this case a multi-mode network consists of 4 multi-modal ports which are terminated by the port impedances Z_n^{mm}, and a single-ended network consists of 4 single-ended ports which are terminated by the port impedances Z_n^{se}. The impedance matrices for both networks are calculated in CST as follows,

$$\mathbf{Z}^{\text{se}} = \begin{bmatrix} 64.4 & 0 & 0 & 0 \\ 0 & 64.4 & 0 & 0 \\ 0 & 0 & 64.4 & 0 \\ 0 & 0 & 0 & 64.4 \end{bmatrix} \qquad \mathbf{Z}^{\text{mm}} = \begin{bmatrix} 46.1 & 0 & 0 & 0 \\ 0 & 46.1 & 0 & 0 \\ 0 & 0 & 38.6 & 0 \\ 0 & 0 & 0 & 29 \end{bmatrix}. \tag{4.5.1}$$

The port voltages and currents for the single-ended network can be calculated from Figure 4.15 and are given by,

$$\begin{aligned}
V_{se_1} &= \frac{1}{2}V_{mm_1} + \frac{1}{2}V_{mm_2} + V_{mm_3} + \frac{1}{2}V_{mm_4}, \\
V_{se_2} &= \frac{1}{2}V_{mm_1} - \frac{1}{2}V_{mm_2} + V_{mm_3} - \frac{1}{2}V_{mm_4}, \\
V_{se_3} &= -\frac{1}{2}V_{mm_1} - \frac{1}{2}V_{mm_2} + V_{mm_3} + \frac{1}{2}V_{mm_4}, \\
V_{se_4} &= -\frac{1}{2}V_{mm_1} + \frac{1}{2}V_{mm_2} + V_{mm_3} - \frac{1}{2}V_{mm_4},
\end{aligned} \tag{4.5.2}$$

$$\begin{aligned}
I_{se_1} &= \frac{1}{2}I_{mm_1} + \frac{1}{2}I_{mm_2} + \frac{1}{4}I_{mm_3} + \frac{1}{2}I_{mm_4}, \\
I_{se_2} &= \frac{1}{2}I_{mm_1} - \frac{1}{2}I_{mm_2} + \frac{1}{4}I_{mm_3} - \frac{1}{2}I_{mm_4}, \\
I_{se_3} &= -\frac{1}{2}I_{mm_1} - \frac{1}{2}I_{mm_2} + \frac{1}{4}I_{mm_3} + \frac{1}{2}I_{mm_4}, \\
I_{se_4} &= -\frac{1}{2}I_{mm_1} + \frac{1}{2}I_{mm_2} + \frac{1}{4}I_{mm_3} - \frac{1}{2}I_{mm_4},
\end{aligned} \tag{4.5.3}$$

which can be written in vector form as follows,

$$\mathbf{V}^{se} = \mathbf{K}^{\text{v}}\mathbf{V}^{mm}, \tag{4.5.4}$$

$$\mathbf{I}^{se} = \mathbf{K}^{\text{i}}\mathbf{I}^{mm}. \tag{4.5.5}$$

The port voltages and currents of the single-ended network can be obtained through superposition of the four multi-mode excitations. The $\mathbf{V}^{se,mm}$ and $\mathbf{I}^{se,mm}$ are $[4 \times 1]$ matrices of the port voltages and currents for the single-ended and multi-mode networks. The transformation matrices $\mathbf{K}^{\mathrm{v}}$ and $\mathbf{K}^{\mathrm{i}}$, discussed in [3], are given by,

$$
\mathbf{K}^{\mathrm{v}} =
\begin{bmatrix}
\frac{1}{2} & \frac{1}{2} & 1 & \frac{1}{2} \\
\frac{1}{2} & -\frac{1}{2} & 1 & -\frac{1}{2} \\
-\frac{1}{2} & -\frac{1}{2} & 1 & \frac{1}{2} \\
-\frac{1}{2} & \frac{1}{2} & 1 & -\frac{1}{2}
\end{bmatrix},
\tag{4.5.6}
$$

$$
\mathbf{K}^{\mathrm{i}} =
\begin{bmatrix}
\frac{1}{2} & \frac{1}{2} & \frac{1}{4} & \frac{1}{2} \\
\frac{1}{2} & -\frac{1}{2} & \frac{1}{4} & -\frac{1}{2} \\
-\frac{1}{2} & -\frac{1}{2} & \frac{1}{4} & \frac{1}{2} \\
-\frac{1}{2} & \frac{1}{2} & \frac{1}{4} & -\frac{1}{2}
\end{bmatrix}.
\tag{4.5.7}
$$

The incident and reflected waves of each port of the single-ended and multi-mode networks can be related to their port voltages and currents by using the definition given in [22] for real port impedances.

This relationship of port voltages and currents to incident and reflected waves is given in matrix form as,

$$
\begin{aligned}
\mathbf{a} &= \frac{1}{2}\mathbf{Z}^{-\frac{1}{2}}\mathbf{V} + \frac{1}{2}\mathbf{Z}^{\frac{1}{2}}\mathbf{I}, \\
\mathbf{b} &= \frac{1}{2}\mathbf{Z}^{-\frac{1}{2}}\mathbf{V} - \frac{1}{2}\mathbf{Z}^{\frac{1}{2}}\mathbf{I},
\end{aligned}
\tag{4.5.8}
$$

or by,

$$
\begin{aligned}
\mathbf{V} &= \mathbf{Z}^{\frac{1}{2}}(\mathbf{a} + \mathbf{b}), \\
\mathbf{I} &= \mathbf{Z}^{-\frac{1}{2}}(\mathbf{a} - \mathbf{b}),
\end{aligned}
\tag{4.5.9}
$$

where $\mathbf{a}$ and $\mathbf{b}$ are $[4 \times 1]$ matrices.

By substituting the diagonal impedance matrices from Equation (4.5.1) into Equation (4.5.8), the $\mathbf{a}^{\mathrm{se}}$ and $\mathbf{b}^{\mathrm{se}}$ incident and reflected waves of the single-ended network can be calculated as follows,

$$
\begin{aligned}
\mathbf{a}^{se} &= \frac{1}{2}\big(\mathbf{Z}^{se}\big)^{-\frac{1}{2}}\mathbf{V}^{se} + \frac{1}{2}\big(\mathbf{Z}^{se}\big)^{\frac{1}{2}}\mathbf{I}^{se}, \\
&= \frac{1}{2}\big(\mathbf{Z}^{se}\big)^{-\frac{1}{2}}\mathbf{K}^{\mathrm{v}}\mathbf{V}^{mm} + \frac{1}{2}\big(\mathbf{Z}^{se}\big)^{\frac{1}{2}}\mathbf{K}^{\mathrm{i}}\mathbf{I}^{mm}, \\
&= \frac{1}{2}\big(\mathbf{Z}^{se}\big)^{-\frac{1}{2}}\mathbf{K}^{\mathrm{v}}\big(\mathbf{Z}^{mm}\big)^{\frac{1}{2}}\big(\mathbf{a}^{mm} + \mathbf{b}^{mm}\big), \\
&+ \frac{1}{2}\big(\mathbf{Z}^{se}\big)^{\frac{1}{2}}\mathbf{K}^{\mathrm{i}}\big(\mathbf{Z}^{mm}\big)^{-\frac{1}{2}}\big(\mathbf{a}^{mm} - \mathbf{b}^{mm}\big),
\end{aligned}
\tag{4.5.10}
$$

$$
\begin{aligned}
\mathbf{b}^{se} &= \frac{1}{2}\big(\mathbf{Z}^{se}\big)^{-\frac{1}{2}}\mathbf{K}^{\mathrm{v}}\big(\mathbf{Z}^{mm}\big)^{\frac{1}{2}}\big(\mathbf{a}^{mm} + \mathbf{b}^{mm}\big), \\
&- \frac{1}{2}\big(\mathbf{Z}^{se}\big)^{\frac{1}{2}}\mathbf{K}^{\mathrm{i}}\big(\mathbf{Z}^{mm}\big)^{-\frac{1}{2}}\big(\mathbf{a}^{mm} - \mathbf{b}^{mm}\big).
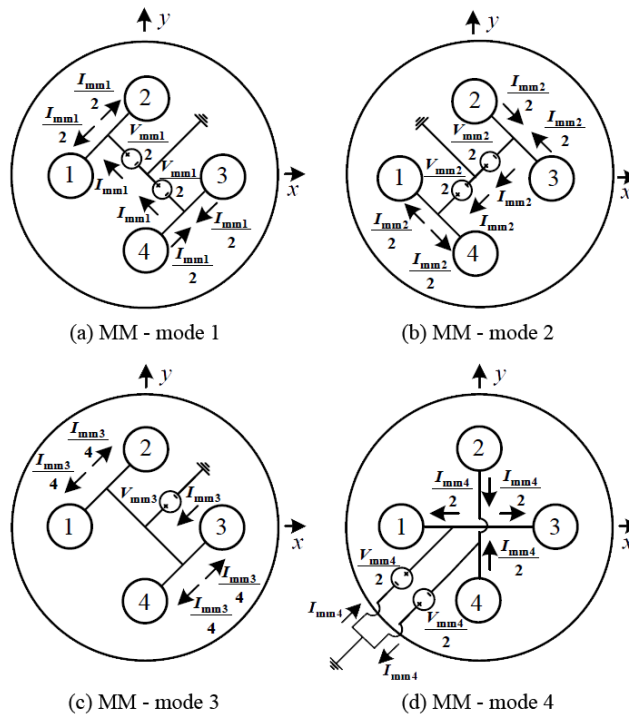\end{aligned}
\tag{4.5.11}
$$

Figure 4.15: Excitations for port modes 1-4 [3].

Equations (4.5.10) and (4.5.11) can be further reduced to,

$$\mathbf{a}^{se} = \mathbf{M}_s \mathbf{a}^{mm} + \mathbf{M}_c \mathbf{b}^{mm},$$
$$\mathbf{b}^{se} = \mathbf{M}_c \mathbf{a}^{mm} + \mathbf{M}_s \mathbf{b}^{mm},$$

(4.5.12)

where matrices $\mathbf{M}_s$ and $\mathbf{M}_c$ are given by,

$$\mathbf{M}_s = \frac{1}{2}\big(\mathbf{Z}^{se}\big)^{-\frac{1}{2}}\mathbf{K}^{v}\big(\mathbf{Z}^{mm}\big)^{\frac{1}{2}} + \frac{1}{2}\big(\mathbf{Z}^{se}\big)^{\frac{1}{2}}\mathbf{K}^{i}\big(\mathbf{Z}^{mm}\big)^{-\frac{1}{2}},$$

(4.5.13)

$$\mathbf{M}_c = \frac{1}{2}\big(\mathbf{Z}^{se}\big)^{-\frac{1}{2}}\mathbf{K}^{v}\big(\mathbf{Z}^{mm}\big)^{\frac{1}{2}} - \frac{1}{2}\big(\mathbf{Z}^{se}\big)^{\frac{1}{2}}\mathbf{K}^{i}\big(\mathbf{Z}^{mm}\big)^{-\frac{1}{2}}.$$

(4.5.14)

4.5.2   The Simulated Results and Verification

The multi-mode network is simulated in CST and the resulting set of S-parameters $\mathbf{S}^{mm}$ is transformed to a set of $\mathbf{S}^{se}$ S-parameters for the single-ended network.

The reflected waves are given by $\mathbf{b}^{se} = \mathbf{S}^{se}\mathbf{a}^{se}$ and $\mathbf{b}^{mm} = \mathbf{S}^{mm}\mathbf{a}^{mm}$ and can be used to calculate the S-parameters of the single-ended network $\mathbf{S}^{se}$ as follows,

$$\mathbf{S}^{se} = \big(\mathbf{M}_c + \mathbf{M}_s \mathbf{S}^{mm}\big)\big(\mathbf{M}_s + \mathbf{M}_c \mathbf{S}^{mm}\big)^{-1}.$$

(4.5.15)

The transformed $\mathbf{S}^{se}$ martix is compared to a second full wave CST simulation of the structure in Figures 4.17a and 4.17b. The results compare the two S-matrices for the multi-mode network and single-ended mode network. Therefore the transformation makes it possible to obtain an excitation matrix $\mathbf{a}^{se}$ from the set of multi-mode excitations that
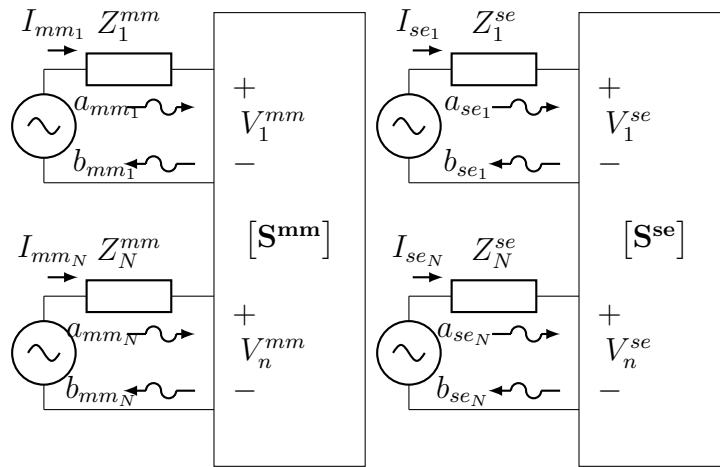
Figure 4.16: Two N-port networks with ports using the multi-mode set (mm) and the single-ended set (se).

enables an ultra-wide field distribution.

For verification the multi-mode excitation matrix given by,

$$\mathbf{a}^{mm} = \begin{bmatrix} 1\angle 0° & 0\angle 0° & 0\angle 0° & 0\angle 0° \\ 0\angle 0° & 1\angle 0° & 0\angle 0° & 0\angle 0° \\ 0\angle 0° & 0\angle 0° & 1\angle 0° & 0\angle 0° \\ 0\angle 0° & 0\angle 0° & 0\angle 0° & 1\angle 0° \end{bmatrix}, \tag{4.5.16}$$

is transformed into the single-ended mode excitation matrix as follows,

$$\mathbf{a}^{se} = \begin{bmatrix} 0.5\angle -0.2° & 0.5\angle -0.2° & 0.5\angle 180° & 0.5\angle 180° \\ 0.5\angle -0.2° & 0.5\angle 180° & 0.5\angle 180° & 0.5\angle -0.2° \\ 0.5\angle 1.6° & 0.5\angle 1.6° & 0.5\angle 1.6° & 0.5\angle 1.6° \\ 0.4\angle -13° & 0.4\angle 167° & 0.4\angle -13° & 0.4\angle 167° \end{bmatrix}. \tag{4.5.17}$$

Figure 4.18 depicts the gain, as simulated in CST, using the incident waves given in Equations (4.5.16) and (4.5.17) for the multi-mode and the transformed single-ended networks respectively. The transformed single-ended mode excitations compare well with the simulated multi-mode set of excitations as illustrated in Figure 4.18.

The $\mathbf{\Upsilon}_{mm}$ set given in Equation (4.3.6) is transformed to its equivalent $\mathbf{\Upsilon}_{se}$ network as follows,

$$\begin{bmatrix} \Upsilon_{se_1} \\ \Upsilon_{se_2} \\ \Upsilon_{se_3} \\ \Upsilon_{se_4} \end{bmatrix} = \begin{bmatrix} 1\underline{/0°} \\ 0.7\underline{/45°} \\ 0 \\ 0.7\underline{/-45°} \end{bmatrix}. \tag{4.5.18}$$

Figure 4.19 compares the simulated gain patterns of the multi-mode set, given in Equation (4.5.18), and the transformed set of single-ended mode excitations, given in Equation (4.5.18). Additionally, the $\boldsymbol{\varrho}_{mm}$ set given in Equation (4.3.8) is transformed into its

equivalent $\boldsymbol{\varrho}_{se}$ network as follows,

$$
\begin{bmatrix}
\varrho_{se_1} \\
\varrho_{se_2} \\
\varrho_{se_3} \\
\varrho_{se_4}
\end{bmatrix}
=
\begin{bmatrix}
2.56\underline{/-9^\circ} \\
0.64\underline{/-32^\circ} \\
0.59\underline{/-46^\circ} \\
0.71\underline{/29^\circ}
\end{bmatrix}.
\tag{4.5.19}
$$

4.6 Conclusion

Within this chapter the quad-mode antenna was explained and the different modal excitations were discussed. The embedded and the isolated element patterns of the quad-mode antenna were examined in Section 4.2.

This chapter continued by obtaining an optimal set of multi-modal port excitations in Section 4.3. Three optimization techniques were used in this section and three different excitation sets were calculated; the complex beamforming weights $\mathbf{w}$ were calculated using the maximum-gain theorem, the GA optimized set of weights $\boldsymbol{\Upsilon}_{mm}$ and the FMINSEARCH optimized the set of weights $\boldsymbol{\varrho}_{mm}$.

The optimized set $\boldsymbol{\varrho}_{mm}$ of the quad-mode antenna yields a broader hemispheric FoV coverage than the S-C QHA, as discussed in Section 4.4.

In Section 4.5 a transformation technique was presented that entails a multi-mode network to be transformed into a single-ended mode network. Furthermore in this section, the simulated CST gain results for the transformation of the multi-mode excitation given in Equation (4.5.16) into the single-ended excitation given in Equation (4.5.17), compare well. The optimized multi-mode sets were calculated and compared.

Therefore further investigation will be conducted to optimize the quad-mode antenna within a planar array configuration.
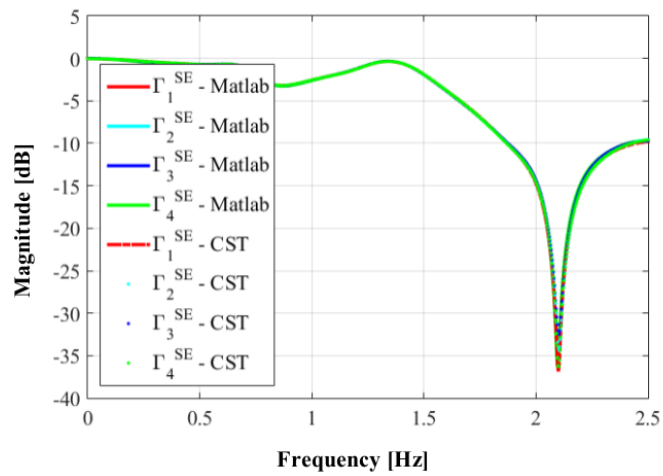
(a) The magnitude given in $[dB]$.
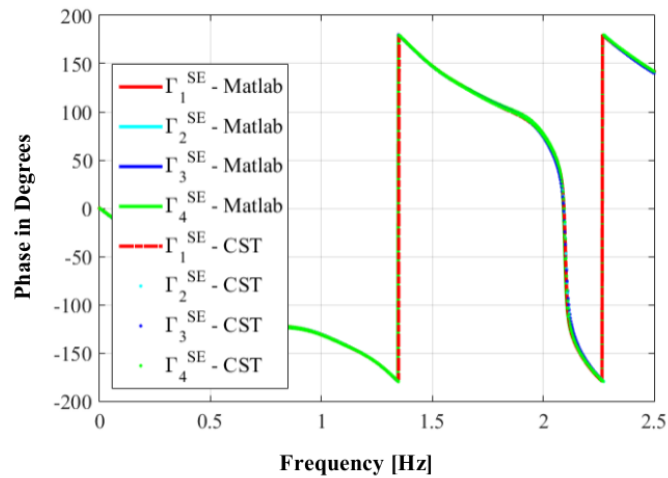
(b) The phase in degrees

Figure 4.17: Comparison of the S-parameters of the simulated single-ended network and the transformed single-ended mode network.
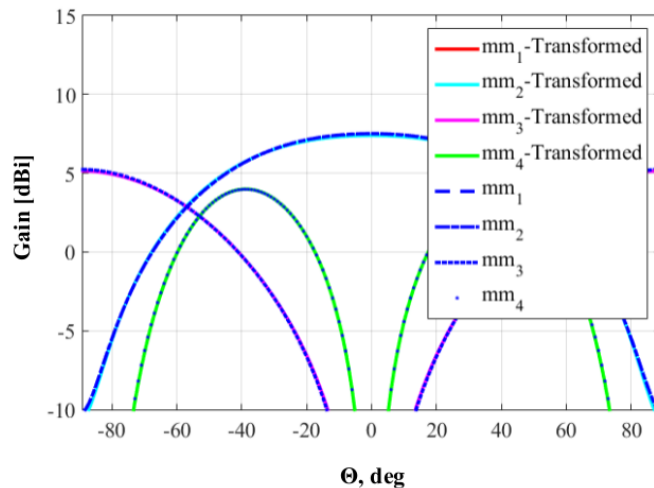
Figure 4.18: Comparison of the simulated transformed single-ended gain and simulated multi-mode gain at $\phi = 0°$ in $|dBi|$.
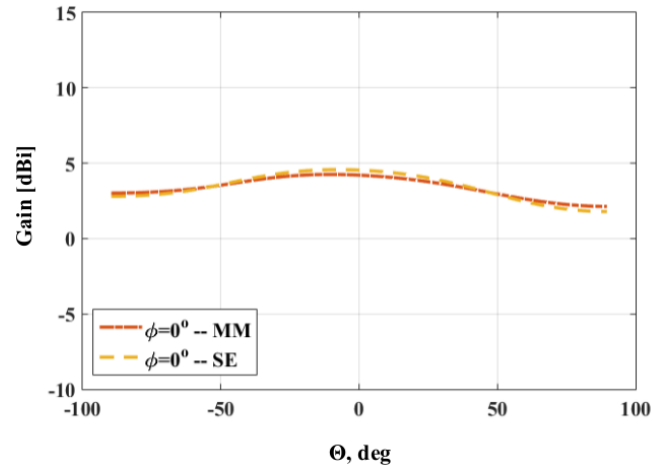
(a) Gain pattern of the quad-mode antenna at $\phi = 0°$.

(b) Gain pattern of the quad-mode antenna at $\phi = 45°$.

(c) Gain pattern of the quad-mode antenna at $\phi = 90°$.

Figure 4.19: 1-D gain pattern in $[dBi]$ of the simulated transformed single-ended mode (**SE**) network and multi-mode (**MM**) network at ϕ-cuts.

Chapter 5

Feed Network System

5.1 Introduction

The four dipole arms, within the quad-mode antenna, are connected and fed by a quadraxial transmission line. By exciting the antenna with an optimal combinational set of complex weighting functions, a hemispherical beam pattern is observed.
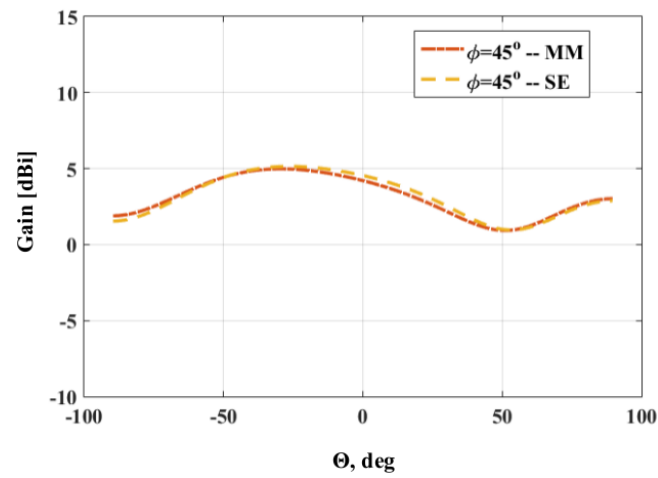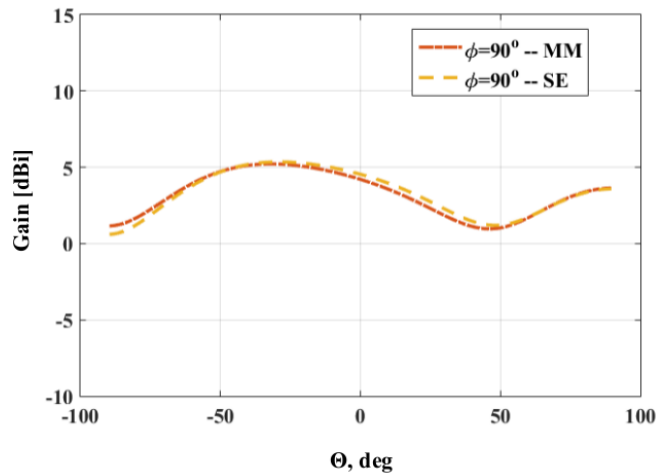
An optimal set of complex excitation weights for the multi-mode network is obtained in Chapter 4. This optimal set is transformed using the theory discussed in Section 4.5 to its equivalent single-ended mode network.

In this chapter the transformed set of single-ended excitations will be used and a quad-mode antenna feed network will be designed. This chapter will also discuss the design theory and investigate the simulated results of the quad-mode antenna feed network. The network will initially be designed in ADS Agilent and redrawn in CST Microwave Studio. The feed network will be integrated into the quad-mode antenna and simulated in CST over an infinite and a finite ground plane. The results will be compared to the initial set of single-ended mode and multi-mode excitations.

5.2 Components of a Feed Network System

This section will discuss the theory of designing the feed network which will be implemented later in this chapter. The theory discussed in this section is based on the empirical formulae given and explained in more detail in [4]. The microstrip line components will be explained in Subsection 5.2.1. Section 5.3 shows the relevant equations that will be used during the design process. Subsection 5.2.2 discusses the concept of even-odd mode analysis. Subsection 5.2.3 explains the design process of an unequal power N-way Wilkinson Power Divider (WPD)[4]. This section will discuss the fundamentals that will be used for the design process in Section 5.3.

5.2.1 Microstrip Line

The geometry of a microstrip line is shown Figure 5.1, with W as the conductor width that is printed on a grounded dielectric substrate of thickness t. The simulation work, discussed in Subsection 5.3.1, will be simulated and performed with PEC as the conductor material and FR-4 for the dielectric substrate. The substrate has a relative permittivity of $\epsilon_r = 4.3$ and is simulated in CST as a loss free substrate.
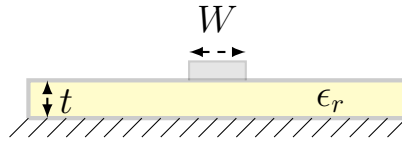
Figure 5.1: Microstrip transmission line geometry.

Due to the geometry of a microstrip line an effective dielectric constant ϵ_{eff} needs to be obtained, which can be approximated by [4],

$$\epsilon_{eff} = \frac{\epsilon_r + 1}{2} + \frac{\epsilon_r - 1}{2} \frac{1}{\sqrt{1 + 12t/W}}. \tag{5.2.1}$$

The propagation constant and phase velocity of the microstrip line, which are needed for the transmission line design, can be equated to,

$$\beta = \frac{\omega}{c}\sqrt{\epsilon_{eff}}, \tag{5.2.2}$$

$$v_p = \frac{\omega}{\beta} = \lambda f_0, \tag{5.2.3}$$

where f_0 is the operating frequency and λ the wavelength. The effective dielectric can be interpreted as a dielectric region that fills the surrounding area of the microstrip transmission line. Given a microstrip line, with a set W and t, the characteristic impedance of the line is approximated as [4],

$$Z_0 = \begin{cases} \frac{60}{\sqrt{\epsilon_{eff}}}\ln\left(\frac{8t}{W} + \frac{W}{4t}\right) & \text{for } W/t \leq 1 \\ \frac{2}{\pi}\left[B - 1 - \ln(2B - 1) + \frac{\epsilon_r - 1}{2\epsilon_r}\left(\ln(B - 1) + 0.39 - \frac{0.61}{\epsilon_r}\right)\right] & \text{for } W/t \geq 1 \end{cases} \tag{5.2.4}$$

where

$$B = \frac{377\pi}{2Z_0\sqrt{\epsilon_r}}. \tag{5.2.5}$$

In actual design processes the transmission line characteristic impedance Z_0 and dielectric substrate ϵ_r are known, and the W/t ratio can be calculated by,

$$W = \frac{8e^A}{e^{2A} - 2}, \tag{5.2.6}$$

for $W/t \leq 2$ and,

$$W = h \times \left[\frac{Z_0}{60}\sqrt{\frac{\epsilon_r + 1}{2}} + \frac{\epsilon_r - 1}{\epsilon_r + 1}\left(0.23 + \frac{0.11}{\epsilon_r}\right)\right], \tag{5.2.7}$$

in a quasi-TEM microstrip line and the constant A is

$$A = \frac{Z_0}{60}\sqrt{\frac{\epsilon_r + 1}{2}} + \frac{\epsilon_r - 1}{\epsilon_r + 1}\left(0.23 + \frac{0.11}{\epsilon_r}\right). \tag{5.2.8}$$

All practical applications in circuit design will inherently contain discontinuities. When modelled at higher frequencies these discontinuities introduce added parasitic reactances in the transmission line. This degrades the performance parameters of the circuit, with

mismatches and spurious coupling or radiation. Bends and T-junctions can be compensated for through chamfering and mitering the transmission line. Therefore by changing the surface area of the microstrip line the added capacitance or inductance will be compensated for. The characteristic impedance equation of a transmission line is $Z_0 = \sqrt{L/C}$. Therefore the characteristic impedance of a line can be adjusted by changing the inductance or capacitance of the line.

Another approach to balance out the excess reactances is to construct an equivalent circuit that will account for the discontinuities. These discontinuities can be compensated for by adjusting the length and width of the transmission line in the design of the circuit.

5.2.2 Even-Odd Mode Analysis

The even-odd mode analysis, discussed in [4], is to be used to derive a WPD. The analysis will simplify the design process of a feed network which will be looked at later in this chapter.

The WPD shown in Figure 5.2 can be simplified by dividing it across mid-plane in a symmetrical form. This is done in Figure 5.3 for even-mode analysis and Figure 5.4 for odd-mode analysis where the quarter-wave transmission lines Z and the shunt resistor r have been normalized to a characteristic impedance Z_0. Choosing the two parallel normalized source resistor to be 2, a equivalent resistor of 1 is obtained at the matched resistor, also normalized. Therefore by choosing the transmission line characteristic impedance to be $Z = \sqrt{2}$ and the shunt resistor to be $r = 2$ an equal-power split will be obtained at the output ports. The even-odd mode voltage excitations are defined as,

$$\text{Even mode } V_{g2} = V_{g3} = 2V_0; \qquad \text{Odd mode } V_{g2} = -V_{g3} = 2V_0, \qquad (5.2.9)$$

where V_0 is the input voltage, V_{g2} the output at port 2 and V_{g3} the output at port 3, as given in [4]. When considering even-mode analysis the following excitations are adapted for each voltage source, $V_{g2} = 4V_0$ and $V_{g3} = 0$. This will allow no current to flow through the shunt resistor and an open circuit is formed across mid-plane, the even-mode circuit is illustrated in Figure 5.3. When looking into P_2 an impedance of $Z_{in}^e = Z^2/2$ is seen. Therefore to match the load at P_2 the transmission line characteristic impedance must be $Z = \sqrt{2}$ then $V_2^e = V_0$ for $Z_{in}^e = 1$.

When calculating the voltage at V_1^e the transmission line equation is used, given in [4] as,

$$V(x) = V^+(e^{-j\beta x} + \Gamma e^{j\beta x}), \qquad (5.2.10)$$

where the propagation constant is $\beta = 2\pi/\lambda$. By letting $x = -\lambda/4$ at the point P_2 Equation (5.2.10) reduces to,

$$V(-\lambda/4) = jV^+(1 - \Gamma) = V_0, \qquad (5.2.11)$$

and setting $x = 0$ at the point P_1 Equation (5.2.10) reduces to,

$$V(0) = V^+(1 + \Gamma) = jV_0\frac{\Gamma + 1}{\Gamma - 1}. \qquad (5.2.12)$$

The reflection coefficient seen at P_1 towards the normalized load resistor of 2 is given as,

$$\Gamma = \frac{2 - \sqrt{2}}{2 + \sqrt{2}}, \qquad (5.2.13)$$
$$\therefore V_1^e = -jV_0\sqrt{2}.$$

For odd-mode analysis the voltage results in a null in the middle when the odd-mode excitations become $V_{g2} = -V_{g3} = 2V_0$ and $V_{3o} = -V_{2o}$. The circuit can then be split as shown in Figure 5.4. In order to match the point P_2 for odd-mode analysis, $r = 2$. This will then result in $V_2^0 = V_0$ and $V_1^0 = 0$ and all the power will be delivered to the $r/2$ resistor and none will go through to the point P_1. This will allow for the input impedance at the point P_1 to be calculated when the output port is terminated in a matched load. By doing so, no current will flow through $r/2$ and the resistor can be removed. Thus, two parallel quarter wavelength transmission lines are connected at the point P_1. The input impedance seen looking towards the load is given as,

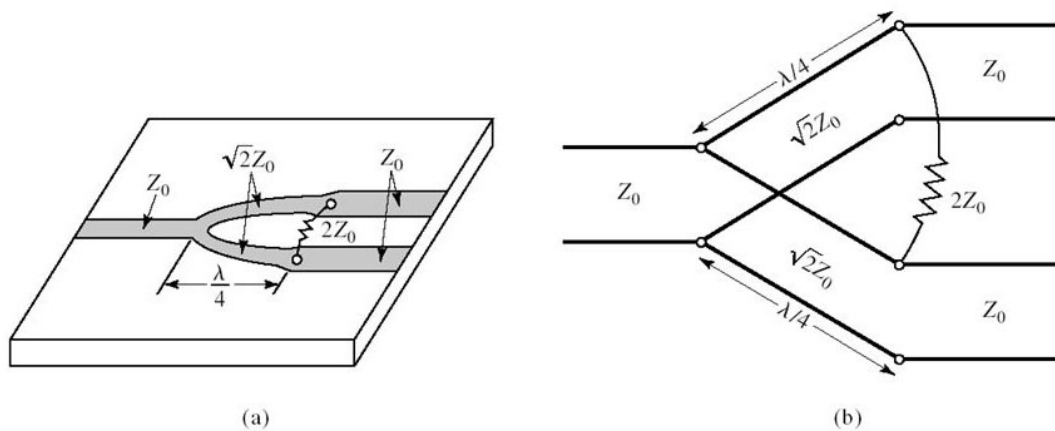$$Z_{in} = \frac{1}{2} = (\sqrt{2})^2 = 1. \tag{5.2.14}$$

Figure 5.2: The Wilkinson power divider. (a) A microstrip line WPD. (b) The equivalent WPD circuit. [4]
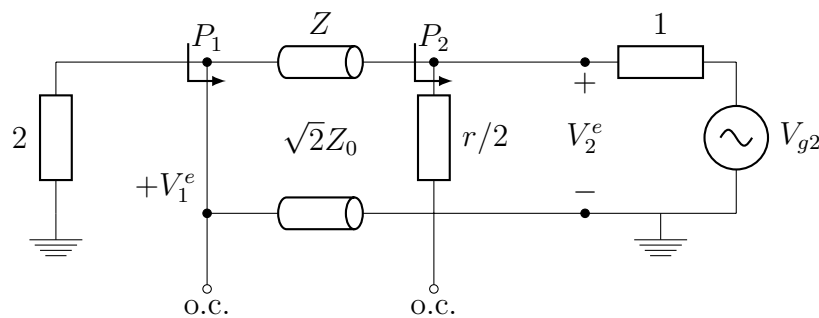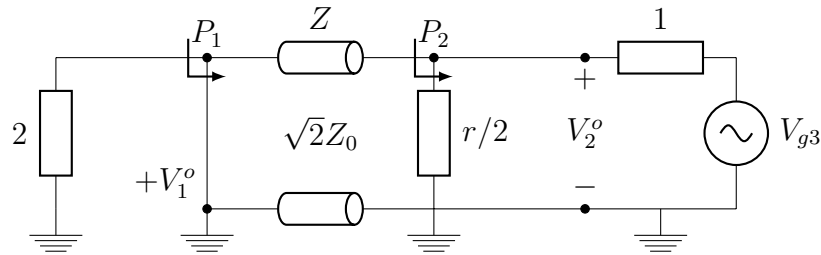

Figure 5.3: Even-mode circuit.
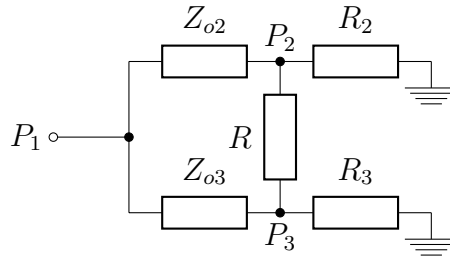
Figure 5.4: Odd-mode circuit.

Figure 5.5: Unequal Wilkinson power divider.

5.2.3 Unequal Power N-way Wilkinson Power Divider

Figure 5.5 illustrates an unequal power split WPD that can be calculated through obtaining a power ratio between port 2 and port 3, given as $k_p = P_3/P_2$. Give the power ratio between each port a characteristic impedance of the two transmission lines is calculated in [4] as,

$$
\begin{aligned}
Z_{02} &= Z_0\sqrt{\frac{1 + k_p^2}{k_p^3}}, \\
Z_{03} &= k_p Z_{03} = Z_0\sqrt{k_p(1 + k_p^2)}, \\
R &= Z_0\left(k_p + \frac{1}{k_p}\right).
\end{aligned}
\tag{5.2.15}
$$

In order to obtain the output impedance R_2 and R_3, a quarter wavelength transmission lines can be used. For the analysis of an N-way WPD a equivalent 2-way model can be obtained. The parameters at the Nth branch can be derived through predefining the power ratio at each branch line and using the combining technique, discussed in [4], to transform the circuit into its equivalent 2-way model. The first branch is then defined as the Nth branch and the second as $N - 1$ branch. This process is repeated until all the branch line parameters are found.

For example considering a 3-way WPD with unequal power division, as illustrated in Figure 5.6. The characteristic impedance of port 2 is calculated through applying the power combining technique between port 3 and port 4. The power ratio is then given as $k_p^2 = P_{combined}/P_2 = 1$. The impedance seen looking into port 2 is given in Equation (5.2.15) and the output resistor at port 2 is chosen to be $R_2 = 50\Omega$. The impedance of port 4 can be obtained by combining ports 2 and 3 and considering the power ratio at the combined ports to be 75% of the input power, then $k_p^2 = 3$. Port 3 and port 4 have the same power ratio and therefore the same results will be obtained for both cases. The impedance
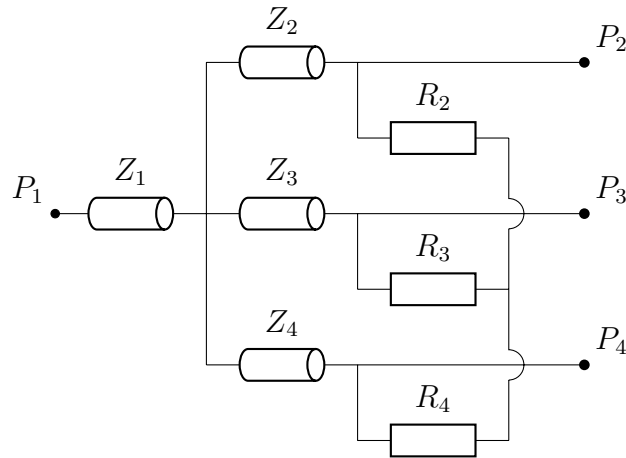
Figure 5.6: A 3-way Wilkinson power divider with unequal power division.

for port 3 and port 4 is obtained from Equation (5.2.15) as, $Z_3 = Z_4 = Z_0\sqrt{(1 + k_p^2)k_p}$ and the output resistors will be matched as follows,

$$R_3 = R_4 = Z_0 k_p. \tag{5.2.16}$$

5.3   The Design Process

A 3-way Power Divider (3PD), shown in Figure 5.7, with unequal amplitudes and phase will be designed using the single-ended complex weights defined in Equation (5.3.1) as follows,

$$\begin{bmatrix} \Upsilon_{se_1} \\ \Upsilon_{se_2} \\ \Upsilon_{se_3} \\ \Upsilon_{se_4} \end{bmatrix} = \begin{bmatrix} 1\underline{/0^\circ} \\ 0.707\underline{/45^\circ} \\ 0 \\ 0.707\underline{/-45^\circ} \end{bmatrix}. \tag{5.3.1}$$

where $\boldsymbol{\Upsilon}_{se}$ is the complex excitation vector for the input ports of the quad-mode antenna. This set is used for the design process of the feed network because it has conventional amplitudes and phase shifts between each port. Additional transmission lines, Z_{p_2}, Z_{p_3} and Z_{p_4}, are added at each output port of the 3PD to compensate for the phase shifts in Equation (5.3.1). The conductor is simulated as a PEC with a FR-4 dielectric substrate. The design process will be subdivided into two parts. The first part calculates the distribution power and the second part matches the quad-mode antenna input impedance to the output port. In order to allow a relative phase shift between each port, additional transmission lines will be added in the matching circuitry. The current ratio between each output port is given as follows,

$$\begin{aligned} I_2 &= 0.42, \\ I_3 &= 0.29, \\ I_4 &= 0.29, \end{aligned} \tag{5.3.2}$$

and the total current ratio I_{total} is given by,

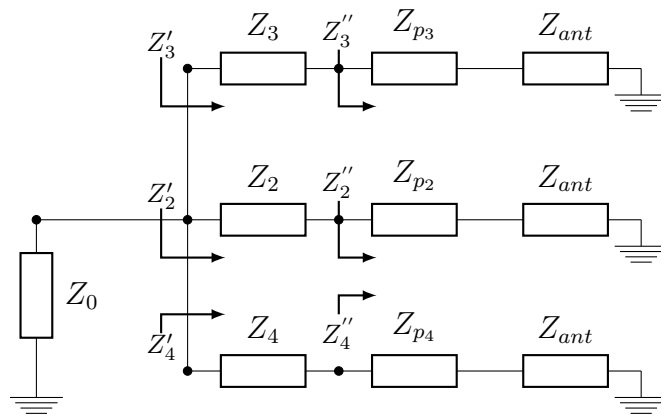$$I_{total} = I_2 + I_3 + I_4 = 1. \tag{5.3.3}$$

Figure 5.7: Three-way power divider, with unequal amplitude and phase shifted.

By choosing the input impedance as $Z_0 = 25 \ \Omega$ and setting the output impedance at port 2 to $Z_2^{''} = 50 \ \Omega$, the characteristic impedances Z_n for each of the n-output ports are obtained through the current forcing property and are calculated as follows,

$$Z_n{'} = \frac{Z_0}{I_n},$$

$$\therefore \quad Z_2{'} = \frac{25}{0.42} = 59.5\Omega, \tag{5.3.4}$$

$$Z_3{'} = Z_4{'} = \frac{25}{0.29} = 86.2\Omega.$$

Due to the property of a $\lambda/4$ transmission line, which is discussed in [4], the voltage at one end of the line is equal to the product of the current and impedance of the line at the other end of the line. Therefore the output impedance looking into ports $Z_2^{''}$, $Z_3^{''}$ and $Z_4^{''}$ is given by,

$$Z_2^{''} = \frac{Z_2^2}{Z_2'} \quad \Rightarrow Z_2 = \sqrt{(50)(59.5)} = 54.6 \ \Omega. \tag{5.3.5}$$

When power is applied at the input, the voltages between each pair of arms in the divider are given as follows,

$$Z_2 I_2 = Z_3 I_3 = Z_4 I_4 \quad \therefore \quad Z_2 I_2 = (54.6)(0.42) = 22.91. \tag{5.3.6}$$

From Equation (5.3.4) the characteristics impedances at port 3 and port 4 are given as,

$$Z_3 I_3 = Z_4 I_4 = 22.91 \quad \Rightarrow Z_3 = Z_4 = \frac{22.91}{0.29} = 79 \ \Omega. \tag{5.3.7}$$

From Equation (5.3.5) the impedance seen looking into port 3 and 4 is $Z_3^{''} = Z_4^{''} = 72.4$ Ω. The relative phase shift between each of the output ports will be implemented using a quarter-wave transformer line and matched to the quad-mode antenna's input impedance, which is $Z_{ant} = 64.4 \ \Omega$ at each dipole arm. The matching circuitry is designed by adjusting the width of the transmission line using Equation (5.2.7) for a microstrip line, using a FR-4 substrate with a permittivity $\epsilon_r = 4.2$ and height $h = 0.5 \ mm$. This will be discussed in more detail in the next Subsection 5.3.1.

The designed model is implemented in ADS Agilent as shown in Figure 5.8 and simulated using the ideal transmission line component. Figure 5.10 shows the magnitudes of the calculated scattering parameters and relative phase shifts at each output port. The results agree with the Υ_{se} set excitations at 2 GHz, given in Equation (5.3.1).
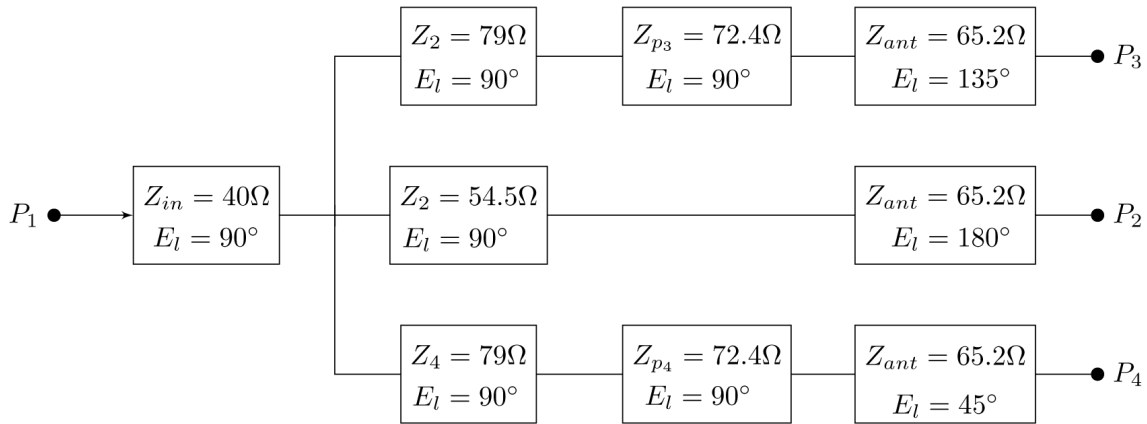
Figure 5.8: The block diagram of the feed network design with ideal transmission lines ADS Agilent representation; with E_ℓ the electric length, Z_{ant} the quad-mode antenna input impedance.

5.3.1 Results, Simulations and Verification of The Feed Network Design

The feed network designed in Section 5.3 is simulated and optimized in ADS Agilent and CST Microwave Studio. Both 3-D EM solvers CST frequency domain and ADS MoM Momentum are based upon Method of Moments (MoM) computational techniques and will be used in this section.

5.3.1.1 ADS simulations

A full wave EM simulation of the design discussed in Section 5.3 is simulated using ADS. The ideal transmission lines, shown in Figure 5.8, are replaced with microstrip line components in ADS. The transmission line widths are calculated using Equation (5.2.7) and electrical lengths, given by [4], as $E_\ell = \beta l$ where $\beta = 2\pi/\lambda$ and λ is obtained using Equation (5.2.3). The model schematic is first simulated and parameter optimized to the specification at each output port. Additionally, the microstrip schematic circuit design is optimized through mitered steps and chamfering bends to compensate for discontinuities which leads to performance degradation.

The optimized scattering parameter results are depicted in Figure 5.11. From Figure 5.11 it can be seen that the circuit is matched well and the output ports are defined to specifications.

The next step in the design process is to generate a layout of the microstrip feed network schematic model and run a full wave EM simulation using ADS Method of Moments Microwave Momentum. The layout is shown in Figure 5.9 and includes the dimensions of the design parameters.

The EM simulation results are depicted in Figure 5.12. By comparing all three ADS simulations it is evident that the ideal model yields the most favourable results. This is because it is a lossless transmission line.

The EM model layout performs well with a low reflection coefficient of $|S_{11}| = -21$ *dB* and the transmission amplitudes are, $|S_{12}| = -3.2$ *dB*, $|S_{13}| = -5.7$ *dB* and $|S_{14}| = -5.9$ *dB* at 2 GH*z*. Furthermore, the relative phase shift between ports 3 and 2 is $-38°$, and
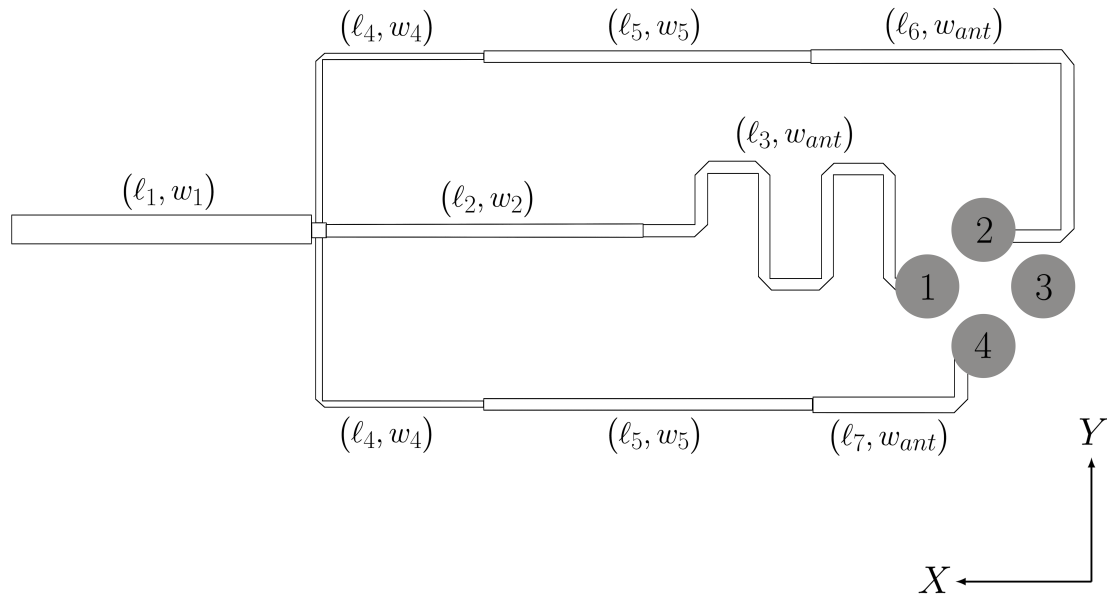
Figure 5.9: The layout diagram of the feed network design, parameter values are given in Table 5.1.

Table 5.1: Feed Network Parameters

Parameters	Values (mm)
ℓ_1	20.97
w_1	2.06
ℓ_2	20.97
w_2	0.82
ℓ_3	42.6
ℓ_4	21.6
w_4	0.385
ℓ_5	21.47
w_5	0.47
ℓ_6	33.5
ℓ_7	12.9
w_{ant}	0.58

the relative phase shift between ports 4 and 2 is 48°. The obtained results surpass the design specifications given in Equation (5.3.1) with an operating frequency of 2 GHz.

### 5.3.1.2   CST simulations

The feed network is redrawn in CST Microwave Studios and simulated above an infinite ground plane using the CST frequency solver domain. Figure 5.13 depicts the transmitted power, $|S_{12}|$, $|S_{13}|$, $|S_{14}|$, the return loss $|S_{11}|$, and relative phase delay between port 2, port 3 and port 4. The results agree with the ADS simulation. Additionally, the feed
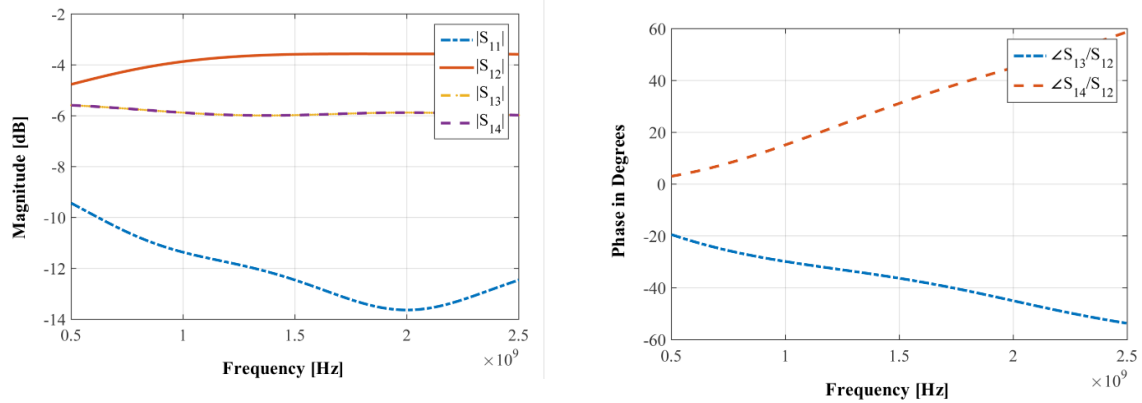
(a) The transmitted power and return loss, in dB.

(b) Relative phase delay of port 3 and port 4.

Figure 5.10: ADS results of the feed network using ideal transmission lines.
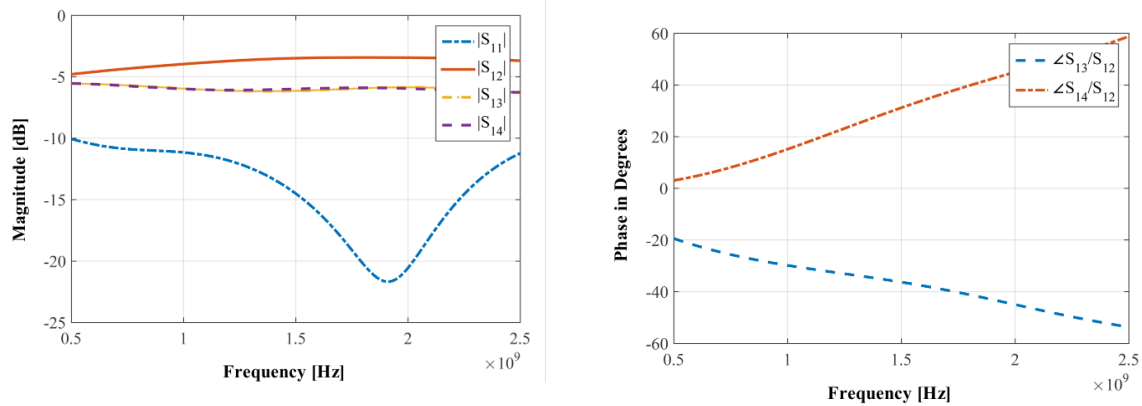
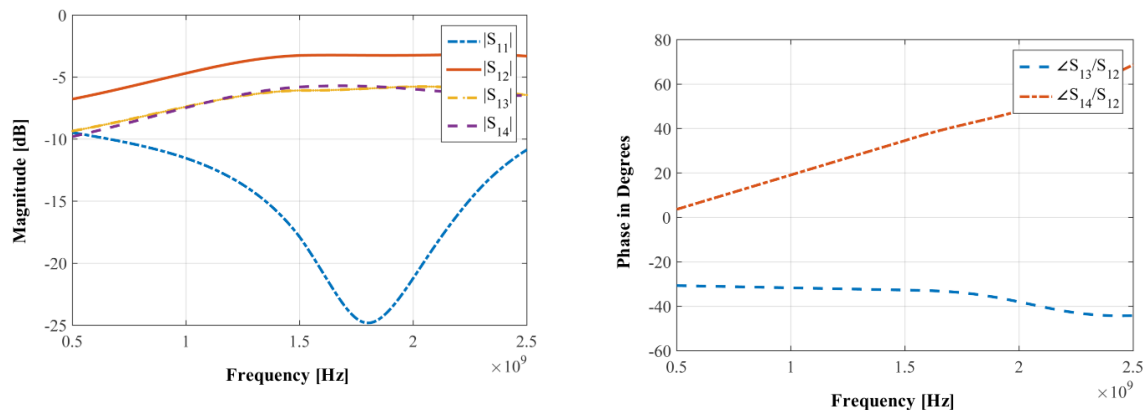(a) The transmitted power and return loss, in dB.

(b) Relative phase delay of port 3 and port 4.

Figure 5.11: ADS results of the feed network model with microstrip transmission lines, FR-4 substrate, and PEC.

(a) ADS simulation of the transmitted power and return loss, in dB.

(b) Relative phase delay of port 3 and port 4.

Figure 5.12: ADS full wave EM MoM simulation results of the feed network layout model.

network system is simulated in CST above a finite ground plane of width $w = 100\ mm$, a lossless FR-4 dielectric substrate and a PEC for the ground plane. Depicted in Figure 5.14 are the results of the transmitted power $|S_{12}|$, $|S_{13}|$, $|S_{14}|$ and the return loss $|S_{11}|$. Both ADS and CST simulations compare well and in the next section the quad-mode antenna will be integrated into the feed system.

The integrated feed network is simulated and the single-ended network excitations are compared for both an infinite ground plane, denoted as $\Upsilon_{se_n}^{inf}$, and a finite ground plane, denoted as $\Upsilon_{se_n}^{fin}$,

$$
\begin{bmatrix} \Upsilon_{se_1}^{inf} \\ \Upsilon_{se_2}^{inf} \\ \Upsilon_{se_3}^{inf} \\ \Upsilon_{se_4}^{inf} \end{bmatrix} = \begin{bmatrix} 1\underline{/0^\circ} \\ 0.75\underline{/-45.9^\circ} \\ 0 \\ 0.75\underline{/44.5^\circ} \end{bmatrix} \quad \begin{bmatrix} \Upsilon_{se_1}^{fin} \\ \Upsilon_{se_2}^{fin} \\ \Upsilon_{se_3}^{fin} \\ \Upsilon_{se_4}^{fin} \end{bmatrix} = \begin{bmatrix} 1\underline{/0^\circ} \\ 0.75\underline{/-45.9^\circ} \\ 0 \\ 0.75\underline{/44.2^\circ} \end{bmatrix}. \tag{5.3.8}
$$

Equation (5.3.8) shows that the phase shift between port 2 and port 4 is 90.4° for the infinite ground plane simulation. The finite ground plane simulation has a phase shift of 90.3° between port 2 and port 4. The two simulations are similar in amplitude and phase. Furthermore, the infinite and finite feed network simulations for the single-ended modes agree with the specified amplitudes and relative phase shifts that were defined in Subsection 4.5.2. The sets of $\Upsilon_{se}^{inf,fin}$ will be compared to the integrated quad-mode antenna network.

The multi-mode set of excitations, after the transformation of single-ended excitation for both finite, denoted $\Upsilon_{mm_n}^{fin}$, and infinite, denoted $\Upsilon_{mm_n}^{inf}$, ground plane simulations are given by,

$$
\begin{bmatrix} \Upsilon_{mm_1}^{inf} \\ \Upsilon_{mm_2}^{inf} \\ \Upsilon_{mm_3}^{inf} \\ \Upsilon_{mm_4}^{inf} \end{bmatrix} = \begin{bmatrix} 0.8\underline{/-44.9^\circ} \\ 0.8\underline{/48.6^\circ} \\ 1\underline{/0^\circ} \\ 0.04\underline{/-175.2^\circ} \end{bmatrix} \quad \begin{bmatrix} \Upsilon_{mm_1}^{fin} \\ \Upsilon_{mm_2}^{fin} \\ \Upsilon_{mm_3}^{fin} \\ \Upsilon_{mm_4}^{fin} \end{bmatrix} = \begin{bmatrix} 0.8\underline{/-44.8^\circ} \\ 0.8\underline{/48.5^\circ} \\ 1\underline{/0^\circ} \\ 0 \end{bmatrix}. \tag{5.3.9}
$$

By comparing the results in Equation (5.3.9) to the initial set of multi-mode excitations, given in Equation (4.3.6), it can be concluded that the results agree and the feed network meets the design specifications.

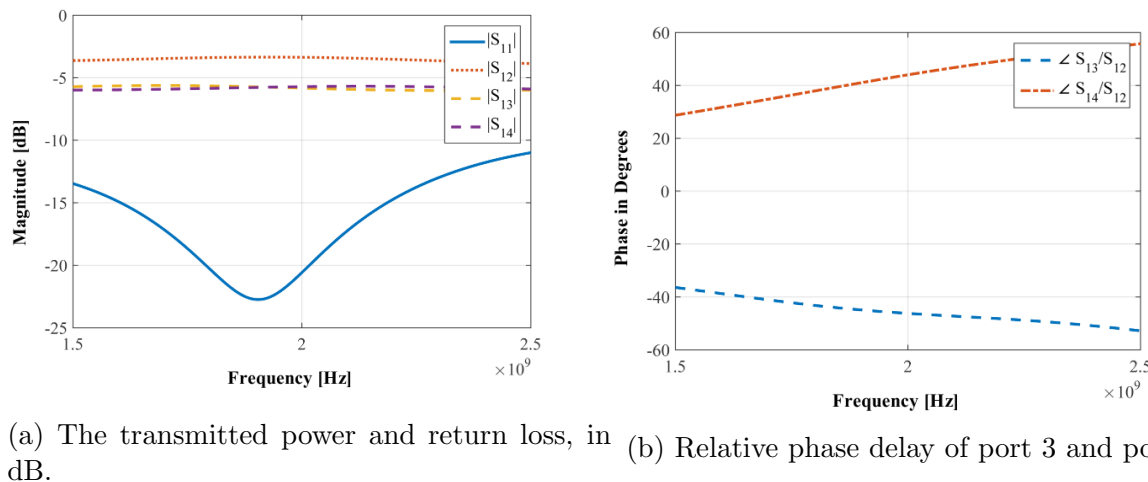## 5.4   Feed Network and Antenna Integration

In this section the far-field radiation patterns of the single-ended mode network and the integrated quad-mode antenna feed network are compared over an infinite and finite ground plane. Figure 5.15 depicts the quad-mode antenna attached to the feed network in CST. Three of the four dipole arms are connected to the output ports of the feed network, port 3 as shown in Figure 5.9 is matched to a 50 Ω impedance.

Figure 5.16 shows the 3-D radiation pattern of the integrated quad-mode antenna design, simulated at 2 GHz over an infinite ground plane using the CST frequency solver. The 3-D radiation pattern of the integrated quad-mode antenna and the single-ended mode network are depicted in Figure 5.16. The integrated quad-mode antenna has a maximum of 4.4 dBi and a gain variation of 8.4 dBi, whereas the single-ended mode network has a maximum gain of 5.4 dBi and a gain variation of 6.65 dBi. The two results has a variation gain that is less than 2 dBi. Figure 5.17 respectively depicts the 1-D gain patterns
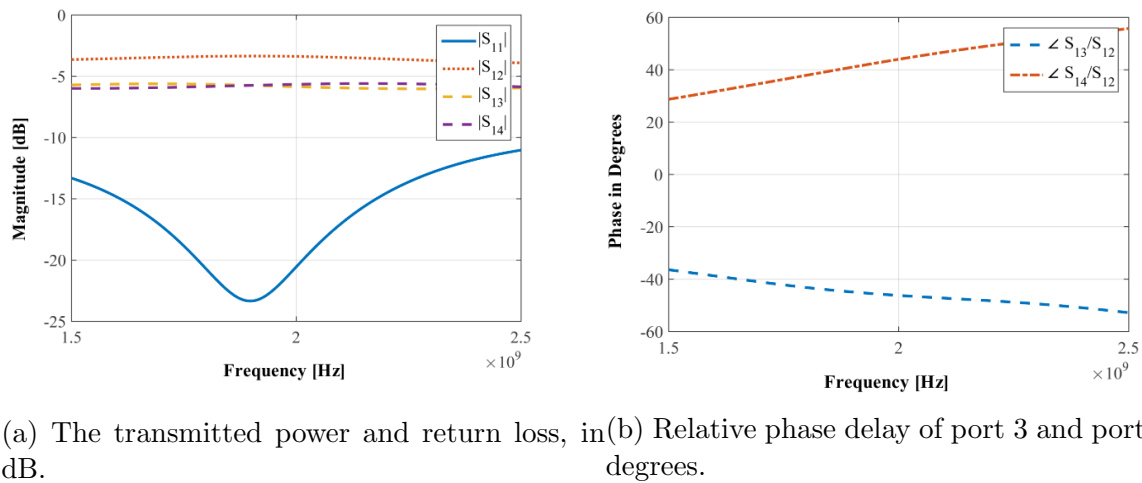
(a) The transmitted power and return loss, in dB.

(b) Relative phase delay of port 3 and port 4, in degrees.

Figure 5.13: CST full wave EM simulation of the feed network layout model over an infinite ground plane.

(a) The transmitted power and return loss, in dB.

(b) Relative phase delay of port 3 and port 4

Figure 5.14: CST full wave EM simulation of the feed network layout model over a finite ground plane.

for the integrated quad-mode antenna and the $[\mathbf{\Upsilon}_{se}]^{inf}$ set compared in the principal and azimuth planes. The feed network has low reflection losses and low coupling between the isolated port 3, from Figure 5.9, and the feed network system.

Figure 5.18 shows the reflection coefficient at the input port S_{11} and S_{21} illustrates the coupling between the input port and the isolated port of the quad-mode antenna. It can be concluded from the results that there is a low coupling factor between the isolated and input port.

The 3-D radiation pattern of the integrated quad-mode antenna is compared to the $[\mathbf{\Upsilon}_{se}]^{fin}$ set as depicted in Figure 5.19, simulated over a finite ground plane.

Figure 5.20 depicts the scattering parameters of the integrated quad-mode antenna system for a finite ground plane. The results show low reflection losses with $|S_{11}| = -21\ dB$ and minor coupling effects between the isolated port and the feed system.

Figure 5.17b depicted a gain variation of 8.6 dBi for the integrated quad-mode antenna simulated in CST for $0° \leq \theta \leq 90°$ and $0° \leq \phi \leq 360°$ over an infinite ground plane, whereas the finite ground plane simulation depicted a gain variation of 12.2 dBi.
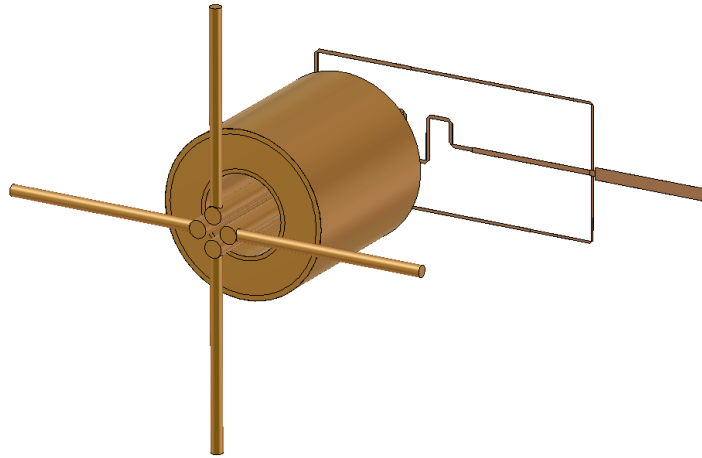
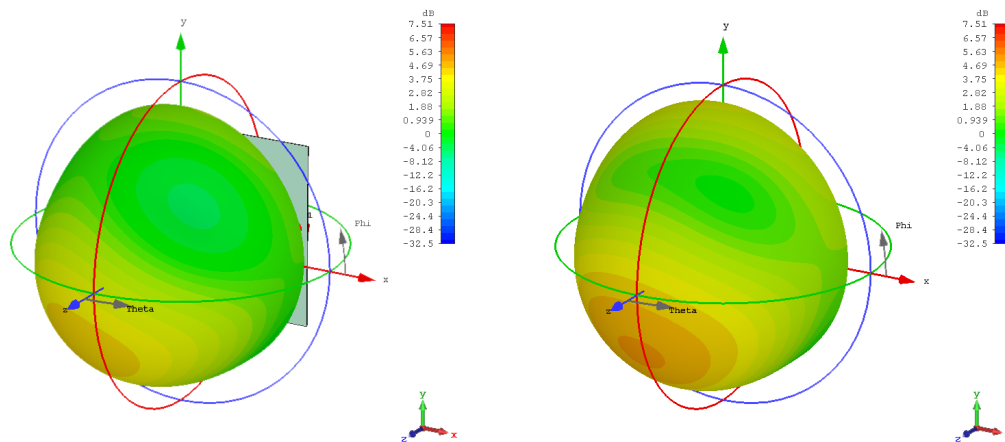Figure 5.15: The quad-mode antenna with the integrated feed network.

5.5   Conclusion

This chapter concludes the design process of a quad-mode antenna feed network system and confirms that a set of $\mathbf{\Upsilon}_{mm}$ can be transformed into its equivalent $\mathbf{\Upsilon}_{se}$ set and an integrated feed network design can be obtained that provides good results.

The basic components of designing a feed network system were discussed in Section 5.2. This section reviewed theory such as the microstrip line, even-odd mode analysis and the Wilkinson power divider.

In Section 5.3 the feed network was designed and the single-ended mode excitations were used at the output ports of the system. The feed network was first designed and simulated in ADS Agilent and then redrawn in CST in order for the feed network to be integrated into the quad-mode antenna.

Section 5.4 discussed the process of integrating the quad-mode antenna into the feed network design. This section also discussed and verified the integrated quad-mode antenna results. The results were compared to the single-ended mode network results which were simulated in CST. The results compared within boundaries and the validity of the feed network was confirmed.

(a) The integrated quad-mode antenna, a maximum of 4.4 *dBi* and a gain variation of 8.4 *dBi*.

(b) The single-ended mode network, a maximum of 5.4 *dBi* and a gain variation of 6.65 *dBi*.

Figure 5.16: The far-field radiation pattern of the integrated quad-mode antenna and the single-ended mode network, simulated in CST over an infinite ground plane.

(a) $\phi = 0°$-plane cut, $|dBi|$

(b) $\phi = 45°$-plane cut, $|dBi|$

(c) $\phi = 90°$-plane cut, $|dBi|$

Figure 5.17: Gain pattern in $|dBi|$ for the quad-mode antenna excited by the feed network compared to the $\mathbf{\Upsilon}_{se}$ and $\mathbf{\Upsilon}_{mm}$ networks' excitation at various ϕ-plane cuts, simulated over a infinite ground plane in CST.
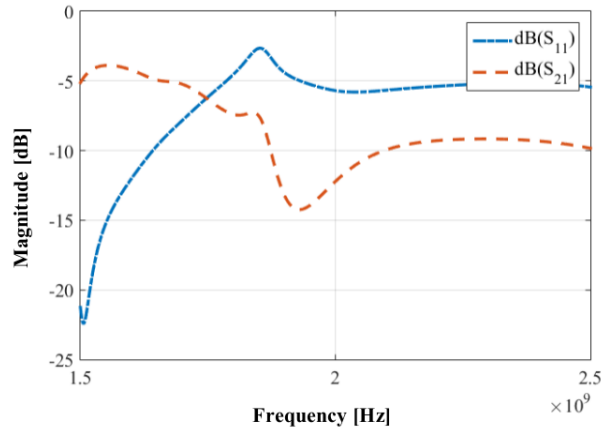
Figure 5.18: The reflection losses in $|dBi|$ and the coupling factor between port 1 and the isolated quad-mode antenna port.
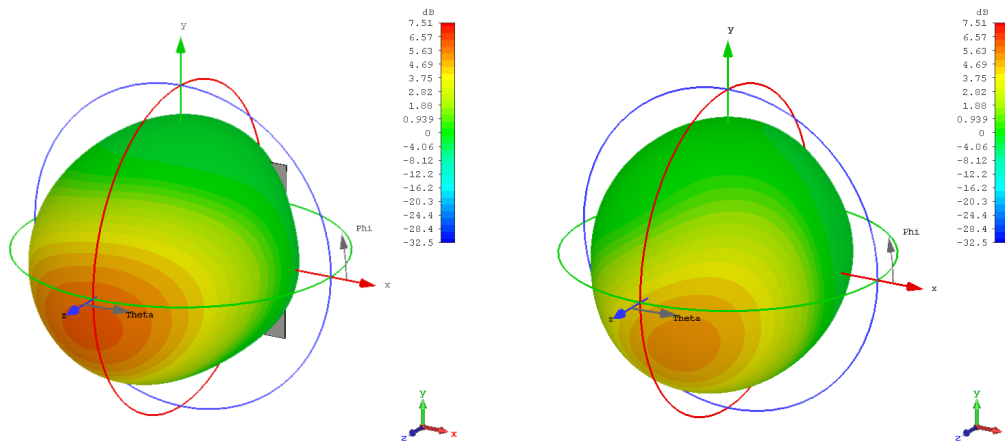
(a) The integrated quad-mode antenna, a maximum of 6.02 dBi with a gain variation of 12.2 dBi.

(b) The single-ended mode network, a maximum of 5.2 dBi and with a gain variation of 9.2 dBi.

Figure 5.19: The far-field radiation pattern of the integrated quad-mode antenna and the single-ended mode network simulated in CST over a finite ground plane.
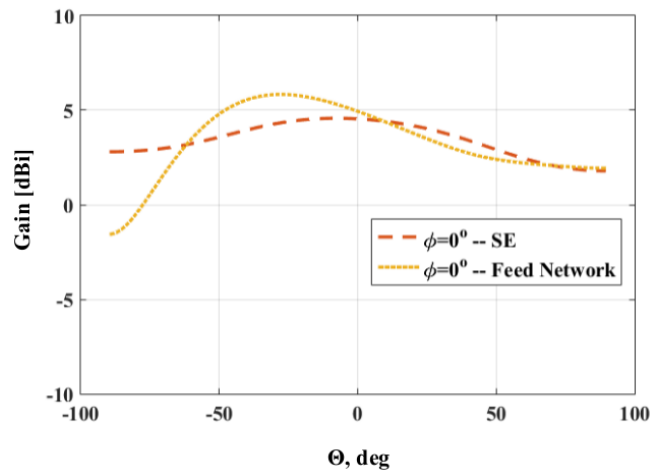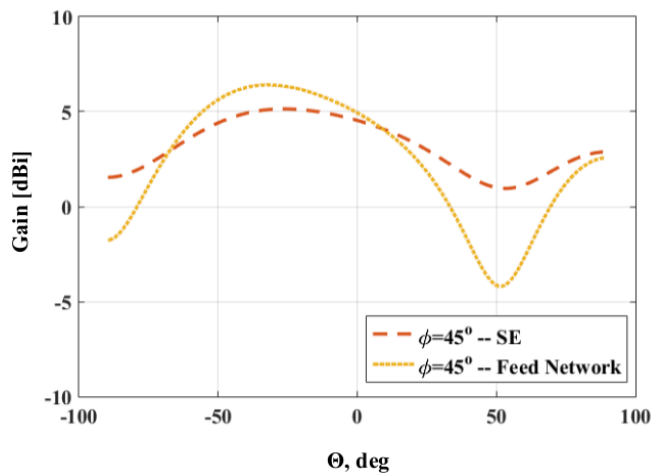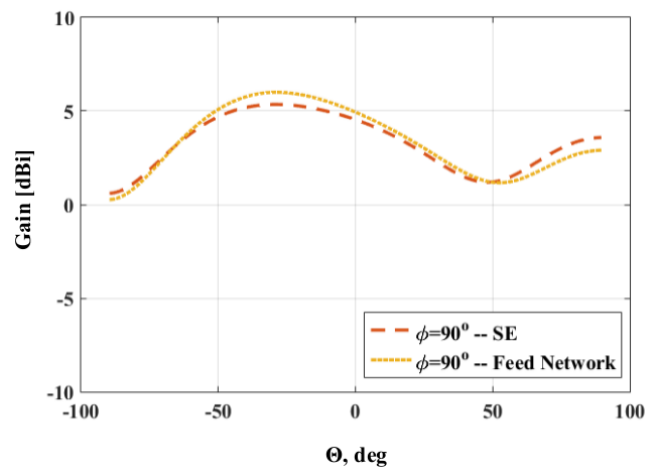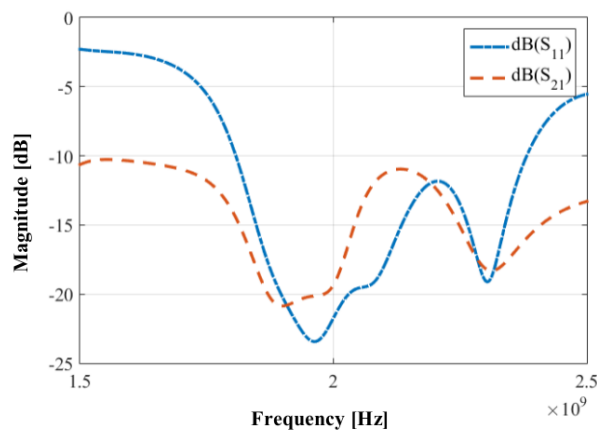

Figure 5.20: The quad-mode antenna feed network simulated over a finite ground plane in CST, the reflection coefficient and the coupling factor between each port.

(a) $\phi = 0°$-plane cut

(b) $\phi = 45°$-plane cut

(c) $\phi = 90°$-plane cut

Figure 5.21: Gain pattern for the quad-mode antenna feed network compared to the $\mathbf{\Upsilon}_{se}$ set of excitations at various ϕ-plane cuts, simulated over a finite ground plane in CST.
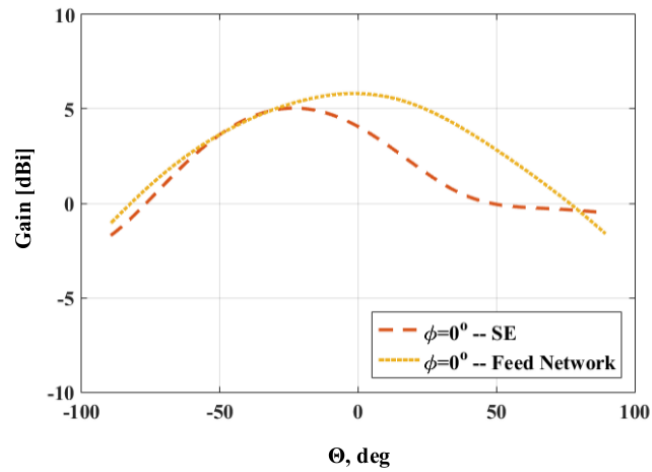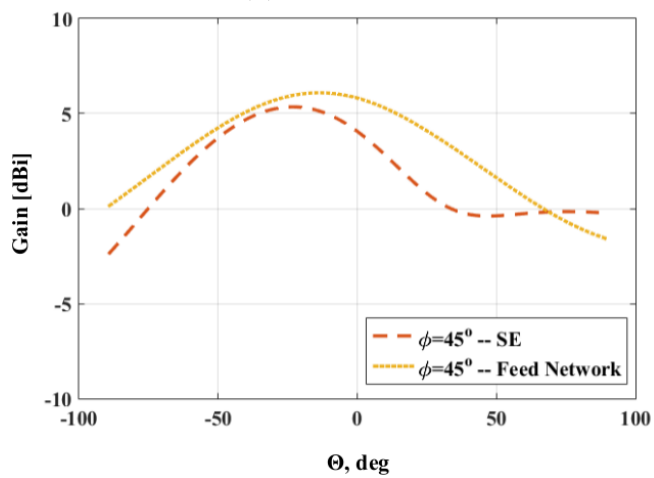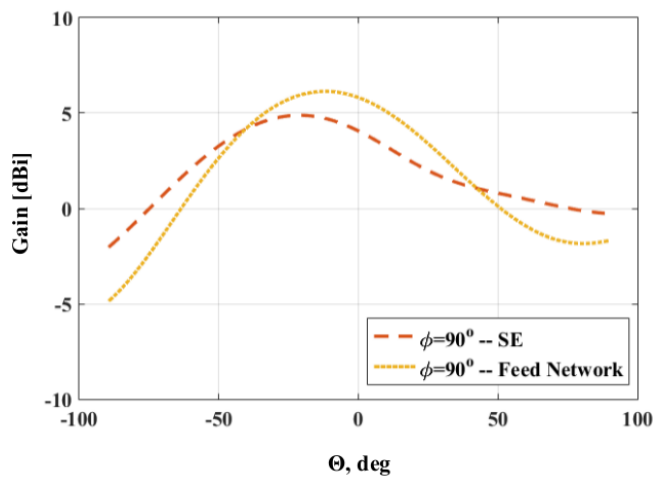
Chapter 6

Phased Array Antenna

6.1 Introduction

Antenna arrays are increasingly being used for a variety of applications due to their ability to control certain parameters of the radiation pattern like beam steering, null angle placement, and increasing the signal-to-noise ratio. In this chapter, the quad-mode antenna is placed in a 2×2 array configuration with the objective of maximizing the radiation pattern over a hemispheric FoV coverage. A combinational set of multi-mode excitation weights will be obtained through beamforming and optimization techniques, such as the GA and the Nelder-Mead simplex algorithm. This optimized set of multi-mode excitation weights will allow for a hemispheric FoV coverage.

To illustrate the basic concept of beamforming and optimization techniques, a 2×2 quarter-wavelength monopole array will be designed and implemented, using the maximum-gain theorem and the GA optimization, to maximize the gain in a certain direction. In turn, two sets of weighting functions will be solved and optimized for a 2×2 quarter-wavelength monopole array. The design and the simulated results will be given in Section 6.2.

The design of a 2×2 quad-mode antenna array will be discussed and a basic array configuration will be implemented. The procedure for obtaining a set of weighting functions that will achieve a hemispheric FoV coverage for the 2×2 quad-mode antenna array will be obtained by implementing the maximum-gain theorem and optimization techniques, such as the GA solver and the FMINSEARCH solver. Various methods will be examined and implemented which will produce a different radiation pattern for each obtained set of weighting functions.

The 2×2 quad-mode antenna array will be excited through the following two procedures as illustrated in Figure 6.1.

- The maximum-gain theorem will be implemented to solve sixteen complex beamforming weighting functions $\mathbf{w}_{mm}^{MGT}$ for each of the four antennas' multi-mode excitation weights. A set of sixteen multi-mode excitation weights will be obtained for each scanned angle over the hemisphere. The complex weighting functions are obtained by using a conjugate-field matching technique.

- The same procedure follows for optimizing a set, $\mathbf{w}_{mm}^{GA}$, of sixteen complex weights through the implementation of the GA.

The GA optimization and the maximum-gain theorem will be simulated and the results will be verified in Subsection 6.3.1.
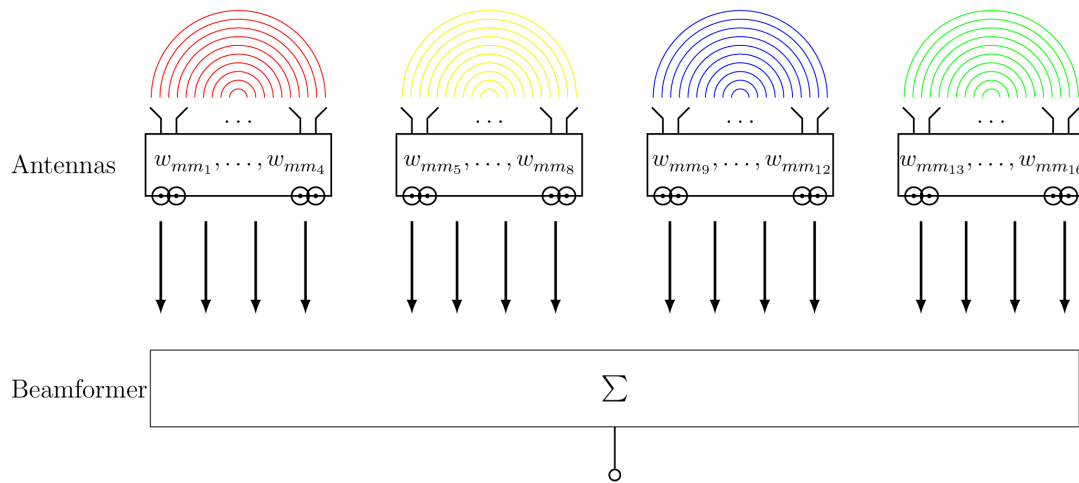
Figure 6.1: A representation of a 2×2 quad-mode antenna array weighted with sixteen multi-mode excitation complex weighting functions.

To reduce the number of complex weighting functions, three further procedures will be investigated. Here the same set of four multi-mode excitation weights $\boldsymbol{\mathcal{N}}_{mm}$ is used for each quad-mode antenna and the four antennas are then weighted with the four-element set $\mathbf{w}_{QMA}$, giving eight complex weighting functions as illustrated in Figure 6.2.
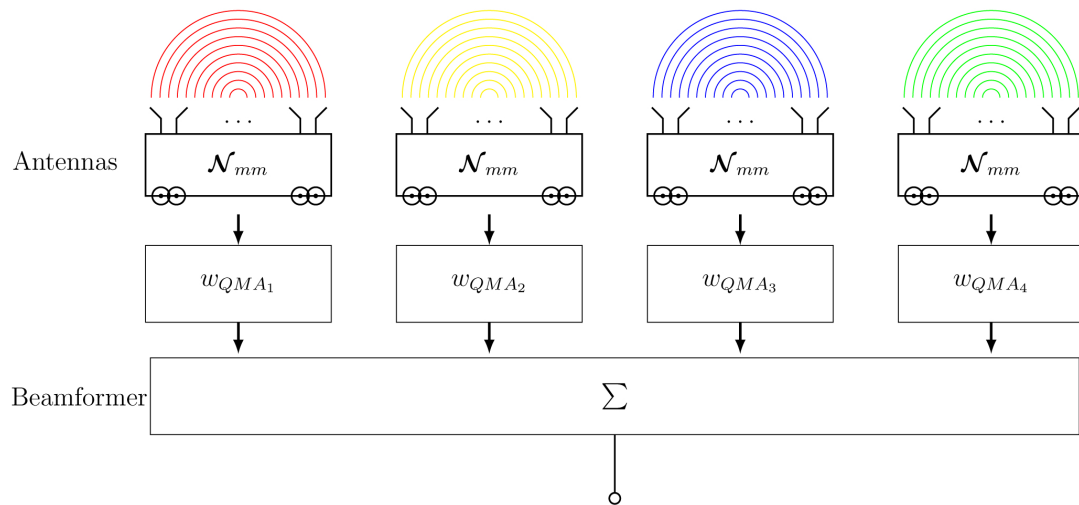
Figure 6.2: A representation of a 2×2 quad-mode antenna array weighted with the following sets of complex weighting functions; $\boldsymbol{\mathcal{N}}_{mm}$ and $\mathbf{w}_{QMA}$.

- In the first case, the eight complex weighting functions will be calculated using the GA optimization with the weights denoted as $\boldsymbol{\mathcal{N}}_{mm}^{GA}$ for the four multi-mode excitation weights and $\mathbf{w}_{QMA}^{GA}$ for the four quad-mode antennas within the array. The results will be implemented and verified in Subsection 6.3.2.

- Alternatively, the weight set $\boldsymbol{\mathcal{N}}_{mm}$ can be determined using the GA or the FMIN-SEARCH algorithms, with the $\mathbf{w}_{QMA}$ set calculated using the maximum-gain theorem. These sets are denoted as $\boldsymbol{\mathcal{X}}_{mm}$, $\mathbf{w}_{QMA}^{MGT}$ and $\boldsymbol{\mathcal{B}}_{mm}$, $\mathbf{w}_{QMA}^{MGT}$. The results will be simulated and verified in Subsection 6.3.3.

- Finally the weight sets, developed in Section 4.3 to create a single quad-mode antenna with a hemispheric FoV, can be used as the weights $\mathcal{N}_{mm}$, with the quad-mode antennas' weights set $\mathbf{w}_{QMA}$ determined using the maximum-gain theorem. These sets are denoted as $\mathbf{\Upsilon}_{mm}$, $\mathbf{w}_{QMA}^{MGT}$ and $\boldsymbol{\varrho}_{mm}$, $\mathbf{w}_{QMA}^{MGT}$. The results will be simulated and verified in Subsection 6.3.4.

Subsection 6.3.5 will compare the above mentioned multi-mode sets of excitation weights; the sixteen multi-mode excitation weights $\mathbf{w}_{mm}^{MGT}$ set, the $\mathbf{\Upsilon}_{mm}$ set, the $\boldsymbol{\varrho}_{mm}$ set, the $\mathcal{X}_{mm}$ set, and the $\mathcal{B}_{mm}$ set.

The solved set of $\mathbf{w}_{mm}^{MGT}$ will be used to steer the beam pattern of an ideal 2×2 quad-mode antenna array, using the isolated and embedded element pattern and the actual 2×2 quad-mode antenna array drawn in CST. The three obtained results will be compared and discussed in Section 6.4.

6.2 The Implementation of a 2×2 Quarter-Wavelength Monopole Array

This section uses a simplistic antenna array configuration in order to demonstrate the basic principle of the maximum-gain beamforming theorem and GA optimization technique. A set of complex weighting functions are used to steer the beam pattern of a 2×2 quarter-wavelength monopole array to obtain a maximum gain towards a desired scanned angle. A quarter-wavelength monopole antenna, discussed in Section A.1, is placed in a 2×2 planar array configuration. Assuming identical antenna elements along the x- and y-direction, the array pattern can be calculated by summing the replicated pattern, $f^{\theta}(\theta, \phi)$, of the monopole antennas, given in Equation (A.1.3). Each element has a relative phase shift applied depending on the antenna's position in the x- and y- plane.

The complex weighting function $\mathbf{w} = [w_1, \ldots, w_4]$ is used to optimize the array gain for the desired angles of θ_0 and ϕ_0. The weighted gain of this array, in matrix form, is given by,

$$G^A(\theta_0, \phi_0) = \frac{\mathbf{w}^H \mathbf{F}_T \mathbf{F}_T^H \mathbf{w}}{P_{rad}}, \tag{6.2.1}$$

where $\mathbf{F}_T$, is a $[4 \times 1]$ matrix of far-fields defined as,

$$\mathbf{F}_T = \begin{bmatrix} f^{\theta}(\theta_0, \phi_0) \\ f^{\theta}(\theta_0, \phi_0)e^{jk_0\frac{\lambda}{2}\beta_y} \\ f^{\theta}(\theta_0, \phi_0)e^{jk_0\frac{\lambda}{2}\beta_x} \\ f^{\theta}(\theta_0, \phi_0)e^{jk_0\frac{\lambda}{2}(\beta_x+\beta_y)} \end{bmatrix}, \tag{6.2.2}$$

and β_x and β_y are given in Equation (2.4.3) and k_0 the propagation constant in free space is given in Equation (2.2.2). A lossless monopole antenna will be considered for further analysis. With a radiation efficiency of one, the total power supplied by the generator will equal the total power radiated by the antenna $P_{rad} = P_{in}$.

The array is ideal and mutual coupling effects will be neglected. The scattering matrix of an ideal array is then obtained by setting $S_{m,n} = 0$ for every $m \neq n$. The reflection coefficient $\Gamma_{m,n}$ for the m, n^{th} element in the array will be equal for an identical element

array $\Gamma_{m,n} = \Gamma$. Furthermore, the S-matrix of a 2×2 monopole array is given by,

$$\mathbf{S}^A = \begin{bmatrix} \Gamma & 0 & 0 & 0 \\ 0 & \Gamma & 0 & 0 \\ 0 & 0 & \Gamma & 0 \\ 0 & 0 & 0 & \Gamma \end{bmatrix}. \tag{6.2.3}$$

The input impedance for a monopole antenna is given in [7] as $Z_{in} = 36.5 + j21.25$. The reflection coefficient is obtained by substituting Z_{in} and a characteristic impedance of $Z_0 = 50 \ \Omega$ into Equation (2.2.11), expressed as $\Gamma = (Z_{in} - Z_0)/(Z_{in} + Z_0)$. This yields a reflection coefficient of $\Gamma = -0.09 + j0.26$. The total radiated power delivered to the quarter-wavelength monopole array is defined by,

$$P_{rad} = \mathbf{w}^H [\mathbf{B}] \mathbf{w}. \tag{6.2.4}$$

The **B** is given by,

$$\mathbf{B} = \left[\mathbf{I} - \mathbf{S}^A [\mathbf{S}^A]^H \right], \tag{6.2.5}$$

The maximum-gain theorem, discussed in Section 2.5, will be implemented here for a 2×2 quarter-wavelength monopole array and the complex beamforming weighting functions are denoted as $[\mathbf{w}^{MGT}]^H = [w_1^{MGT}]^* \dots [w_4^{MGT}]^*$. By taking the partial derivative of the gain matrix in Equation (6.2.1) with respect to $[\mathbf{w}^{MGT}]^H$ and equating it to zero, the maximum gain problem simply becomes a generalized eigenvalue problem as discussed in Subsection 2.5.2 with **A** and **B** square matrices of size $[2 \times 2]$.

The matrix **A** can be expressed as,

$$\mathbf{A} = \mathbf{F}_T \mathbf{F}_T^H. \tag{6.2.6}$$

The complex beamforming weights that give maximum gain in all scanned angles can be obtained by solving the eigenvector problem and taking the conjugate of the eigenvector corresponding to the largest eigenvalue obtained. The beam pattern of the array achieves a maximum gain towards a desired direction when the conjugate-field matching condition is satisfied [6]. Therefore each port within the array is excited with a combinational set of complex conjugate weights $[\mathbf{w}^{MGT}]^H$ that allows the beam pattern to be steered in a desired angular direction.

The GA optimization, discussed in Subsection 3.4.1, is implemented here in order to optimize the set of complex beamforming weights $\mathbf{w}^{GA} = [w_1^{GA}, \dots, w_4^{GA}]$. This is done through correctly defining the fitness function discussed in Section 3.3. The complex weight $\mathbf{w}^{GA}$ is optimized by maximizing the array gain, $G^A(\theta_0, \phi_0)$, given in Equation (6.2.1), in decibel for a desired angular direction of θ_0 and ϕ_0. That is,

$$G_{max} = \max_{\mathbf{w}} G^A(\theta_0, \phi_0) \qquad \forall \quad \left(0° \leq \theta_0 \leq 90°; 0° \leq \phi_0 \leq 360° \right). \tag{6.2.7}$$

The fitness value F is minimized in order to obtain a combinational set of complex weighting functions which will achieve a maximum beam pattern in the desired direction. The fitness function is then given as,

$$\min_{\mathbf{w}} F = G - G_{max}, \tag{6.2.8}$$

where $G = 15 \ dBi$ is chosen and F is the fitness value to be minimized.

The 2×2 quarter-wavelength monopole array beam pattern is scanned to different angles

by exciting the array with an optimal set of combinational weights. The results are depicted in Figures 6.3 and 6.4, for the maximum-gain theorem used to solve for the $[\mathbf{w}^{MGT}]^{H}$ set and the GA optimization used to optimize the $\mathbf{w}^{GA}$ set, respectively.

The maximum-gain beamforming theorem and the GA optimization techniques obtained the same maxima at each scanned angle, as seen in Figures 6.3 and 6.4. Therefore it can be concluded that the GA optimization approach gives the same optimal value as the maximum-gain theorem and thus will be used for further analysis of a 2×2 quad-mode antenna array.
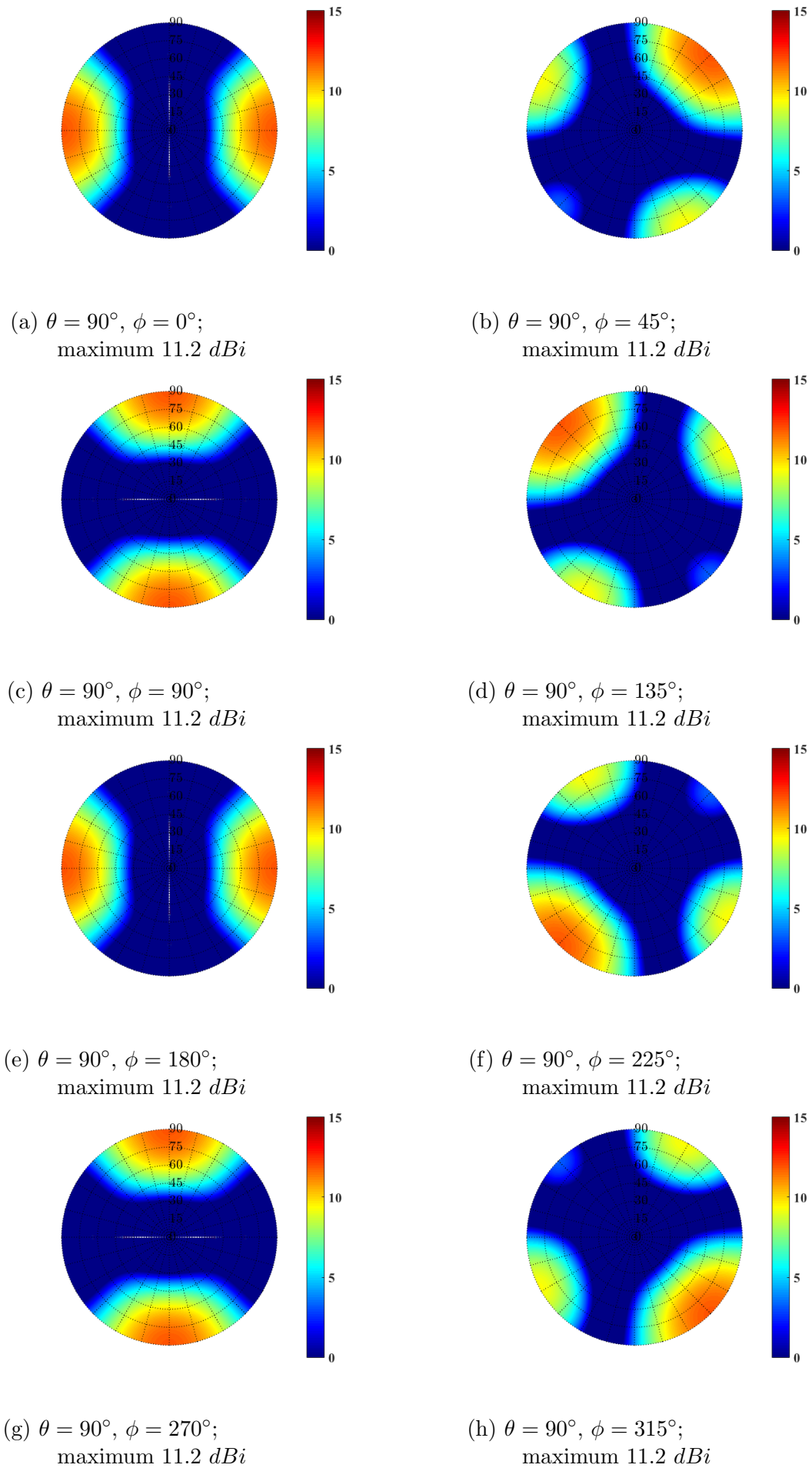
(a) $\theta = 90°$, $\phi = 0°$;
maximum 11.2 dBi

(b) $\theta = 90°$, $\phi = 45°$;
maximum 11.2 dBi

(c) $\theta = 90°$, $\phi = 90°$;
maximum 11.2 dBi

(d) $\theta = 90°$, $\phi = 135°$;
maximum 11.2 dBi

(e) $\theta = 90°$, $\phi = 180°$;
maximum 11.2 dBi

(f) $\theta = 90°$, $\phi = 225°$;
maximum 11.2 dBi

(g) $\theta = 90°$, $\phi = 270°$;
maximum 11.2 dBi

(h) $\theta = 90°$, $\phi = 315°$;
maximum 11.2 dBi

Figure 6.3: Gain patterns in $[dBi]$ for the 2×2 quarter-wavelength monopole array excited by the optimized set of $[\mathbf{w}^{MGT}]^H$.

(a) $\theta = 90°$, $\phi = 0°$;
maximum 11.2 dBi

(b) $\theta = 90°$, $\phi = 45°$;
maximum 11.2 dBi

(c) $\theta = 90°$, $\phi = 90°$;
maximum 11.2 dBi

(d) $\theta = 90°$, $\phi = 135°$;
maximum 11.2 dBi

(e) $\theta = 90°$, $\phi = 180°$;
maximum 11.2 dBi

(f) $\theta = 90°$, $\phi = 225°$;
maximum 11.2 dBi

(g) $\theta = 90°$, $\phi = 270°$;
maximum 11.2 dBi

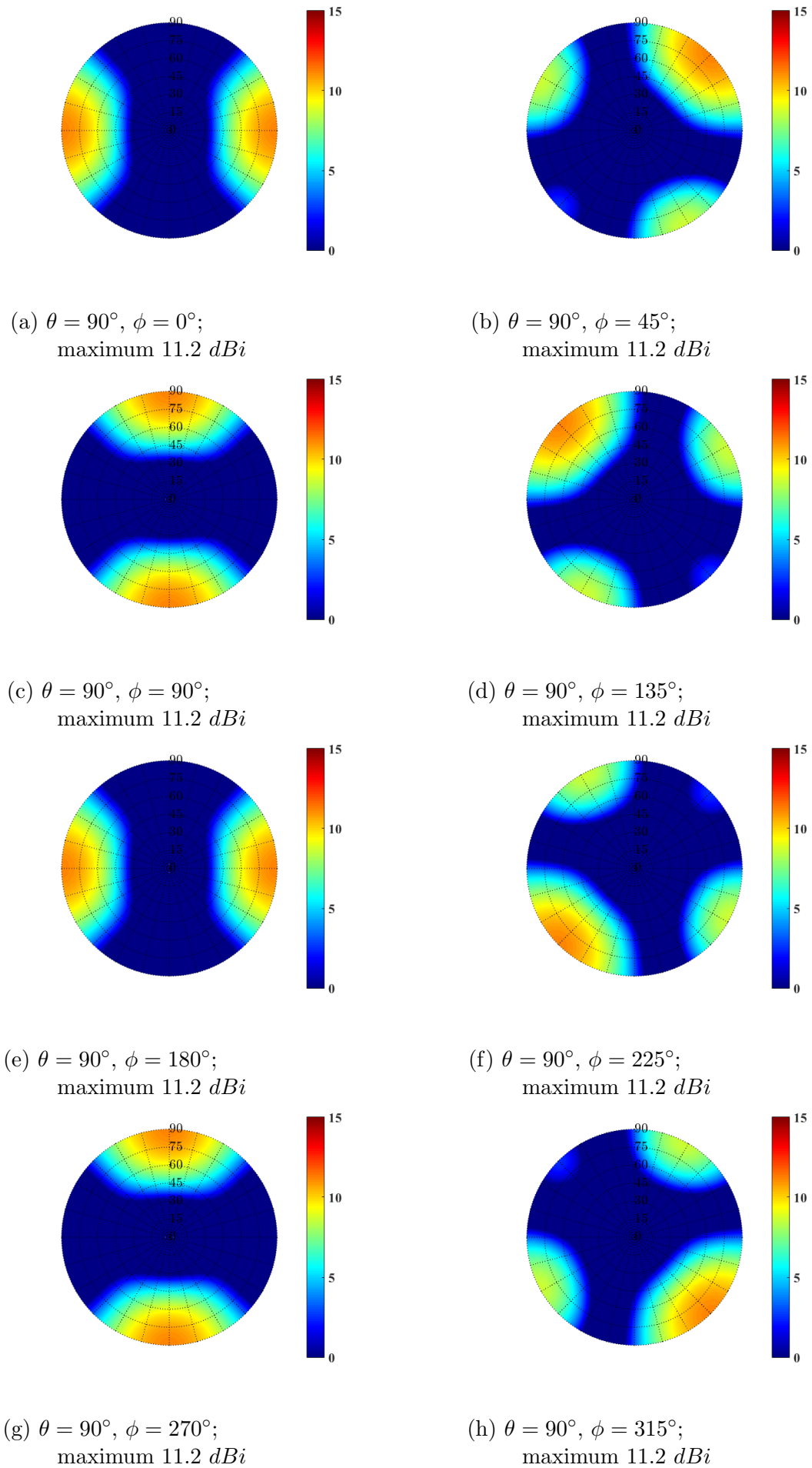(h) $\theta = 90°$, $\phi = 315°$;
maximum 11.2 dBi

Figure 6.4: Gain patterns in $[dBi]$ for the 2×2 quarter-wavelength monopole array excited by the optimized set of $\mathbf{w}^{GA}$.

6.3   The Implementation of a 2×2 Quad-Mode Antenna Array

The quad-mode antenna is placed in a 2×2 planar array configuration, as shown in Figure 2.4, with an interelement spacing of $\lambda/2$. A single quad-mode antenna total electric field pattern $\mathbf{F}(\theta, \phi)$ at the origin, is extracted from CST as,

$$\mathbf{F}(\theta, \phi) = f_{mm_n}^{\theta}(\theta, \phi)\hat{\boldsymbol{\theta}} + f_{mm_n}^{\phi}(\theta, \phi)\hat{\boldsymbol{\phi}}, \tag{6.3.1}$$

where f_{mm_n} represents the quad-mode antenna's multi-mode electric field radiation pattern as defined in Section 4.2. The single quad-mode antenna's weighted radiation pattern, discussed in Chapter 4, is repeated here for the ease of reading,

$$U(\theta, \phi) = \frac{1}{\eta}\left|\sum_{n=1}^{4} w_{mm_n} f_{mm_n}^{\theta}(\theta, \phi)\right|^2 + \frac{1}{\eta}\left|\sum_{n=1}^{4} w_{mm_n} f_{mm_n}^{\phi}(\theta, \phi)\right|^2, \tag{6.3.2}$$

and the gain,

$$G(\theta, \phi) = 4\pi \frac{U(\theta, \phi)}{P_{in}}. \tag{6.3.3}$$

Given that it is a lossless system the total input power P_{in} is given by,

$$P_{in} = P_{rad} = \mathbf{w}_{mm}^{H}\big[I - \mathbf{S}[\mathbf{S}]^{H}\big]\mathbf{w}_{mm}, \tag{6.3.4}$$

where $\mathbf{w}_{mm}$ is the complex multi-mode set of excitations and $\mathbf{S}$ is the scattering matrix of the single antenna element which is extracted from CST as,

$$\mathbf{S} = \begin{bmatrix} S_{11} & S_{12} & S_{13} & S_{14} \\ S_{21} & S_{22} & S_{23} & S_{24} \\ S_{31} & S_{22} & S_{33} & S_{34} \\ S_{41} & S_{42} & S_{43} & S_{44} \end{bmatrix}. \tag{6.3.5}$$

The beam pattern of a 2×2 quad-mode antenna array will be scanned towards a desired direction. This is achieved by exciting the array elements in an optimum condition and will be accomplished using the maximum-gain theorem and MATLAB optimization toolboxes.

The embedded element pattern, discussed in Subsection 2.4.1, is a crucial performance characteristic in beamforming that enables a realizable gain pattern in a desired angular direction. The embedded element pattern will be simulated at 2 GHz using CST's periodic boundary conditions application. The simulated electric field pattern of the quad-mode antenna will be extracted from CST, mathematically implemented in an array configuration and used to steer the beam pattern towards a maximum. Furthermore, the application allows the users to specify the antenna's scanned angle. This allows the mathematically calculated array to be verified using CST's far-field array application with an interelement spacing of $\lambda/2$. The array's beam pattern will be steered towards broadside $\theta = 0°$ and compared in MATLAB with the mathematically implemented array.

The notation $\mathbf{w}_{QMA} = [w_{QMA_1}, \dots, w_{QMA_4}]$ will denote the complex weighting function of each quad-mode antenna with respect to its position within the array configuration. From here on the following notations will be used; w_{QMA_1} represents the complex weighting function of the reference antenna positioned at $(0, 0)$; w_{QMA_2} represents the complex

weighting function of the antenna at position $(0, d)$; w_{QMA_3} represents the complex weighting function of the antenna at position $(d, 0)$ and w_{QMA_4} represents the complex weighting function of the antenna at position (d, d), where $d = \lambda/2$. The multi-mode excitation sets $\mathbf{w}_{mm}^{MGT,GA}$, $\mathcal{N}_{mm}^{GA}$, $\mathcal{X}_{mm}$, and $\mathcal{B}_{mm}$ will be optimized using the GA algorithm and the FMINSEARCH optimization toolboxes in MATLAB and solved for using the maximum-gain theorem.

6.3.1 The Maximum-Gain Theorem Implemented for the $\mathbf{w}_{mm}^{MGT}$ Set and the Genetic Algorithm Optimization for the $\mathbf{w}_{mm}^{GA}$ Set
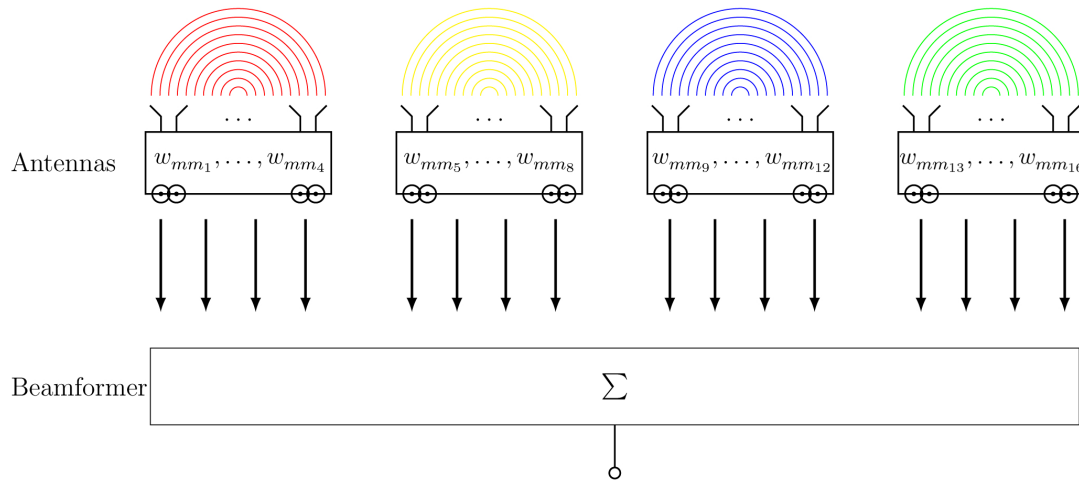

Figure 6.5: A representation of a 2×2 quad-mode antenna array weighted with the set of sixteen multi-mode excitation weights $\mathbf{w}_{mm}$.

The sixteen complex weighting functions $\mathbf{w}_{mm}$ are used to excite a 2×2 quad-mode antenna array as illustrated in Figure 6.5. The maximum-gain theorem is implemented to maximize the beam pattern over a hemispheric FoV coverage through solving the weighting functions that satisfy the conjugate field matching conditions [6].
The complex beamforming weighting function is given as $[\mathbf{w}_{mm}^{MGT}]^H = [w_{mm_1}^{MGT}]^*, \ldots, [w_{mm_{16}}^{MGT}]^*$. The array field vector $\mathbf{F}_T$ at the input of the beamformer is given by a two-dimensional array of sixteen element patterns as follows,

$$
\mathbf{F}_T = \begin{bmatrix}
f_{mm_1}^{\theta} & f_{mm_1}^{\phi} \\
\vdots & \vdots \\
f_{mm_4}^{\theta} & f_{mm_4}^{\phi} \\
f_{mm_1}^{\theta} e^{jk_0 \frac{\lambda}{2}\beta_y} & f_{mm_1}^{\phi} e^{jk_0 \frac{\lambda}{2}\beta_y} \\
\vdots & \vdots \\
f_{mm_4}^{\theta} e^{jk_0 \frac{\lambda}{2}\beta_y} & f_{mm_4}^{\phi} e^{jk_0 \frac{\lambda}{2}\beta_y} \\
f_{mm_1}^{\theta} e^{jk_0 \frac{\lambda}{2}\beta_x} & f_{mm_1}^{\phi} e^{jk_0 \frac{\lambda}{2}\beta_x} \\
\vdots & \vdots \\
f_{mm_4}^{\theta} e^{jk_0 \frac{\lambda}{2}\beta_x} & f_{mm_4}^{\phi} e^{jk_0 \frac{\lambda}{2}\beta_x} \\
f_{mm_1}^{\theta} e^{jk_0 \frac{\lambda}{2}(\beta_y+\beta_x)} & f_{mm_1}^{\phi} e^{jk_0 \frac{\lambda}{2}(\beta_y+\beta_x)} \\
\vdots & \vdots \\
f_{mm_4}^{\theta} e^{jk_0 \frac{\lambda}{2}(\beta_y+\beta_x)} & f_{mm_4}^{\phi} e^{jk_0 \frac{\lambda}{2}(\beta_y+\beta_x)}
\end{bmatrix}, \tag{6.3.6}
$$

where the progressive phase delays β_x and β_y are given in Equation (2.4.3) and k_0 the propagation constant in free space is given in Equation (2.2.2). Equation (6.3.6) gives the four multi-mode electric field patterns $f_{mm_1}, \ldots, f_{mm_4}$ of the single quad-mode antenna,

each with a relative phase shift depending on the antenna's position vector. The far-field array radiation vector at the output of the beamformer is defined as follows,

$$\mathbf{F}_{out} = [\mathbf{w}_{mm}^{MGT}]^H \mathbf{F}_T. \tag{6.3.7}$$

Additionally, the output power of the array is given by,

$$
\begin{aligned}
\left|\mathbf{F}_{out}\right|^2 &= \mathbf{F}_{out}\mathbf{F}_{out}^*, \\
&= \left([\mathbf{w}_{mm}^{MGT}]^H \mathbf{F}_T\right)\left([\mathbf{w}_{mm}^{MGT}]^H \mathbf{F}_T\right)^*, \\
&= [\mathbf{w}_{mm}^{MGT}]^H \mathbf{F}_T \mathbf{F}_T^H [\mathbf{w}_{mm}^{MGT}].
\end{aligned}
\tag{6.3.8}
$$

The weighted array gain is obtained and given in its matrix form as,

$$G^A(\theta, \phi) = \frac{4\pi}{\eta}\left[\frac{[\mathbf{w}_{mm}^{MGT}]^H \mathbf{F}_T \mathbf{F}_T^H [\mathbf{w}_{mm}^{MGT}]}{[\mathbf{w}_{mm}^{MGT}]^H \left[I - \mathbf{S}^A[\mathbf{S}^A]^H\right][\mathbf{w}_{mm}^{MGT}]}\right], \tag{6.3.9}$$

where η is the free space impedance and $\mathbf{S}^A$ is the S-matrix of the ideal planar array configuration. The array S-matrix is a $[16 \times 16]$ matrix given by,

$$\mathbf{S}^A = \begin{bmatrix} [\mathbf{S}] & 0 & \dots & 0 \\ 0 & [\mathbf{S}] & & \vdots \\ \vdots & & [\mathbf{S}] & 0 \\ 0 & \dots & 0 & [\mathbf{S}] \end{bmatrix}, \tag{6.3.10}$$

where the $[4 \times 4]$ matrix $[\mathbf{S}]$ is the S-matrix of the single quad-mode antenna extracted from CST.

Following the same procedure as discussed in Subsection 2.5.2, the weighted array gain in Equation (6.3.9) is maximized by taking the partial derivative of $G^A(\theta, \phi)$ with respect to $[\mathbf{w}_{mm}^{MGT}]^H$ and equating the determinant to zero, which is given as,

$$\det(\mathbf{F}\mathbf{F}^H - G^A(\theta, \phi)\mathbf{B}) = 0, \tag{6.3.11}$$

By solving the characteristic Equation (6.3.11) for the largest root, a complex beamforming weight $[\mathbf{w}_{mm}^{MGT}]^H$ is obtained that directs the gain to a maximum at each scanned angle.

The GA optimization is implemented by minimizing the fitness value F_{itness}. The multi-mode set of excitations $\mathbf{w}_{mm}^{GA} = [w_{mm_1}^{GA}, \dots, w_{mm_{16}}^{GA}]$ for the four antennas within the array will be optimized for maximum gain over the hemisphere. The far-field radiation pattern

of the array $\mathbf{F}_T$ is defined here as,

$$[\mathbf{F}_T]_n = \begin{bmatrix} f^\theta_{mm_1} & f^\phi_{mm_1} \\ \vdots & \vdots \\ f^\theta_{mm_4} & f^\phi_{mm_4} \\ f^\theta_{mm_1}e^{jk_0\frac{\lambda}{2}\beta_y} & f^\phi_{mm_1}e^{jk_0\frac{\lambda}{2}\beta_y} \\ \vdots & \vdots \\ f^\theta_{mm_4}e^{jk_0\frac{\lambda}{2}\beta_y} & f^\phi_{mm_4}e^{jk_0\frac{\lambda}{2}\beta_y} \\ f^\theta_{mm_1}e^{jk_0\frac{\lambda}{2}\beta_x} & f^\phi_{mm_1}e^{jk_0\frac{\lambda}{2}\beta_x} \\ \vdots & \vdots \\ f^\theta_{mm_4}e^{jk_0\frac{\lambda}{2}\beta_x} & f^\phi_{mm_4}e^{jk_0\frac{\lambda}{2}\beta_x} \\ f^\theta_{mm_1}e^{jk_0\frac{\lambda}{2}(\beta_y+\beta_x)} & f^\phi_{mm_1}e^{jk_0\frac{\lambda}{2}(\beta_y+\beta_x)} \\ \vdots & \vdots \\ f^\theta_{mm_4}e^{jk_0\frac{\lambda}{2}(\beta_y+\beta_x)} & f^\phi_{mm_4}e^{jk_0\frac{\lambda}{2}(\beta_y+\beta_x)} \end{bmatrix}. \tag{6.3.12}$$

The gain of the array is given as,

$$G^A(\theta,\phi) = \frac{4\pi}{\eta} \frac{\sum_{n=1}^{16} |w^{GA}_{mm_n}[F^\theta_T]_n|^2 + |w^{GA}_{mm_n}[F^\phi_T]_n|^2}{\mathbf{w}^{GA}_{mm}\big[I - \mathbf{S}^A[\mathbf{S}^A]^H\big][\mathbf{w}^{GA}_{mm}]^H}, \tag{6.3.13}$$

where η is the free space impedance and $\mathbf{S}^A$ is given in Equation (6.3.10). The array gain is maximized as,

$$G_{max} = \max_{w^{GA}_{mm_1},...,w^{GA}_{mm_{16}}} G^A(\theta_0,\phi_0)dB \qquad \forall \quad \left(0° \leq \theta_0 \leq 90°; 0° \leq \phi_0 \leq 360°\right) \tag{6.3.14}$$

for the desired angle of θ_0, ϕ_0. The fitness function is evaluated by minimizing the fitness value as,

$$\min_{w^{GA}_{mm_1},...,w^{GA}_{mm_{16}}} F = G - G_{max} \tag{6.3.15}$$

and $G = 15\ dBi$ is chosen as the maximum gain threshold.

The optimized complex weighting functions, $\mathbf{w}^{MGT,GA}_{mm}$, results are verified and the radiation patterns are simulated using the embedded element pattern. The embedded element pattern omits the edge effects of the elements in the array and therefore the results presented here are only an approximation of an actual 2×2 quad-mode antenna array.

The normalized complex beamforming weighting functions solved at broadside are given in Equation (6.3.16), which compares the obtained weighting functions of the beamforming weights and the GA optimized weights. Equation (6.3.16) shows that a maximum

beam pattern at $\theta = 0°$, is achieved through only exciting the crossed dipole modes.

$$
\begin{bmatrix} w^{MGT}_{mm_1} \\ w^{MGT}_{mm_2} \\ w^{MGT}_{mm_3} \\ w^{MGT}_{mm_4} \\ w^{MGT}_{mm_5} \\ w^{MGT}_{mm_6} \\ w^{MGT}_{mm_7} \\ w^{MGT}_{mm_8} \\ w^{MGT}_{mm_9} \\ w^{MGT}_{mm_{10}} \\ w^{MGT}_{mm_{11}} \\ w^{MGT}_{mm_{12}} \\ w^{MGT}_{mm_{13}} \\ w^{MGT}_{mm_{14}} \\ w^{MGT}_{mm_{15}} \\ w^{MGT}_{mm_{16}} \end{bmatrix} = \begin{bmatrix} 1\underline{/0°} \\ 0.57\underline{/-16°} \\ 0 \\ 0 \\ 1\underline{/0°} \\ 0.57\underline{/-16°} \\ 0 \\ 0 \\ 1\underline{/0°} \\ 0.57\underline{/-16°} \\ 0 \\ 0 \\ 1\underline{/0°} \\ 0.57\underline{/-16°} \\ 0 \\ 0 \end{bmatrix}, \quad \begin{bmatrix} w^{GA}_{mm_1} \\ w^{GA}_{mm_2} \\ w^{GA}_{mm_3} \\ w^{GA}_{mm_4} \\ w^{GA}_{mm_5} \\ w^{GA}_{mm_6} \\ w^{GA}_{mm_7} \\ w^{GA}_{mm_8} \\ w^{GA}_{mm_9} \\ w^{GA}_{mm_{10}} \\ w^{GA}_{mm_{11}} \\ w^{GA}_{mm_{12}} \\ w^{GA}_{mm_{13}} \\ w^{GA}_{mm_{14}} \\ w^{GA}_{mm_{15}} \\ w^{GA}_{mm_{16}} \end{bmatrix} = \begin{bmatrix} 0.9\underline{/0°} \\ 1\underline{/0°} \\ 0 \\ 0 \\ 0.92\underline{/1°} \\ 1\underline{/0°} \\ 0 \\ 0 \\ 0.92\underline{/1°} \\ 1\underline{/0°} \\ 0 \\ 0 \\ 0.9\underline{/1°} \\ 1\underline{/0°} \\ 0 \\ 0 \end{bmatrix}. \tag{6.3.16}
$$

The resultant maximum gain patterns are given in Figures 6.6a and 6.6b for the solved $\mathbf{w}^{MGT}_{mm}$ set and optimized $\mathbf{w}^{GA}_{mm}$ set. The results illustrate the same beam pattern as a horizontal dipole array. The results show that the solved and optimized sets correlate.

The theoretical array gain calculated in MATLAB for the set of $\mathbf{w}^{MGT}$ is verified with the simulated CST far-field array gain of the embedded pattern at broadside, as illustrated Figure 6.7. The results compare well and the mathematically calculated array can be used for further analysis.

Furthermore, the array beam pattern is steered to the desired angular directions of a constant $\theta = 45°$ with increments of $45°$ for ϕ starting from $0°$ to $360°$. The gain patterns are depicted in Figures 6.8 and 6.9, for the solved and optimized sets obtained through the maximum-gain theorem and GA algorithms, respectively. The corresponding complex weights are summarized in Tables 6.1 and 6.2. The two methods compare well and maximize the gain pattern of the array towards a desired direction.

The maximum gain values of each scanned angle over a hemispheric FoV coverage are depicted in Figure 6.10 for the $w^{MGT}_{mm_1}, \ldots, w^{MGT}_{mm_{16}}$ set, obtained through solving for the maximum-gain beamforming theorem.

Table 6.1: 16 Complex Weights Obtained from the Maximum Gain Beam forming Theorem

θ , ϕ	$45°, 0°$	$45°, 45°$	$45°, 90°$	$45°, 135°$	$45°, 180°$	$45°, 225°$	$45°, 270°$	$45°, 315°$
$w_{mm_1}^{MGT}$	$0.4\angle-60°$	$0.5\angle-54°$	$0.4\angle-60°$	0	$0.4\angle199°$	$0.5\angle126°$	$0.4\angle119°$	0
$w_{mm_2}^{MGT}$	$0.4\angle-61°$	0	$0.4\angle120°$	$0.5\angle126°$	$0.4\angle199°$	0	$0.4\angle-60°$	$0.5\angle-54°$
$w_{mm_3}^{MGT}$	$0.8\angle16°$	0	$0.8\angle-165°$	0	$0.8\angle16°$	0	$0.8\angle-164°$	0
$w_{mm_4}^{MGT}$	$1\angle0°$	$1\angle0°$	$1\angle0°$	$1\angle0°$	$1\angle0°$	$1\angle0°$	$1\angle0°$	$1\angle0°$
$w_{mm_5}^{MGT}$	$0.4\angle-60°$	$0.5\angle-144°$	$0.4\angle172°$	0	$0.4\angle199°$	$0.5\angle-144°$	$0.4\angle-113°$	0
$w_{mm_6}^{MGT}$	$0.4\angle-6116°$	0	$0.4\angle-8°$	$0.5\angle35°$	$0.4\angle199°$	0	$0.4\angle67°$	$0.51\angle36°$
$w_{mm_7}^{MGT}$	$0.8\angle16°$	0	$0.8\angle68°$	0	$0.8\angle16°$	0	$0.8\angle-37°$	0
$w_{mm_8}^{MGT}$	$1\angle0°$	$1\angle-90°$	$1\angle-127°$	$1\angle-90°$	$1\angle0°$	$1\angle90°$	$1\angle127°$	$1\angle90°$
$w_{mm_9}^{MGT}$	$0.4\angle173°$	$0.5\angle-144°$	$0.4\angle-60°$	0	$0.4\angle-114°$	$0.5\angle-144°$	$0.4\angle119°$	0
$w_{mm_{10}}^{MGT}$	$0.4\angle172°$	0	$0.4\angle119°$	$0.5\angle-144°$	$0.4\angle-113°$	0	$0.4\angle-60°$	$0.51\angle-144°$
$w_{mm_{11}}^{MGT}$	$0.8\angle-112°$	0	$0.8\angle-164°$	0	$0.8\angle143°$	0	$0.8\angle164°$	0
$w_{mm_{12}}^{MGT}$	$1\angle-127°$	$1\angle-90°$	$1\angle0°$	$1\angle90°$	$1\angle127°$	$1\angle90°$	$1\angle0°$	$1\angle-90°$
$w_{mm_{13}}^{MGT}$	$0.4\angle173°$	$0.5\angle126°$	$0.4\angle172°$	0	$0.4\angle-114°$	$0.5\angle-54°$	$0.4\angle-113°$	0
$w_{mm_{14}}^{MGT}$	$0.4\angle172°$	0	$0.4\angle-8°$	$0.5\angle126°$	$0.4\angle-113°$	0	$0.4\angle67°$	$0.51\angle-54°$
$w_{mm_{15}}^{MGT}$	$0.8\angle-112°$	0	$0.8\angle68°$	0	$0.8\angle143°$	0	$0.8\angle-37°$	0
$w_{mm_{16}}^{MGT}$	$1\angle-127°$	$1\angle-180°$	$1\angle-127°$	$1\angle0°$	$1\angle127°$	$1\angle180°$	$1\angle127°$	$1\angle0°$

Table 6.2: 16 Complex Weights Optimized using the Genetic Algorithm

θ, ϕ	$45°, 0°$	$45°, 45°$	$45°, 90°$	$45°, 135°$	$45°, 180°$	$45°, 225°$	$45°, 270°$	$45°, 315°$
$w^{GA}_{mm_1}$	$0.8\angle 101°$	$0.8\angle 10°$	$0.1\angle 28°$	$0.1\angle -92°$	$0.9\angle -47°$	0	$0.59\angle 12°$	$0.59\angle 30°$
$w^{GA}_{mm_2}$	$0.9\angle -86°$	0	$1\angle 0°$	$0.8\angle -90°$	$0.9\angle 125°$	$0.73\angle -142°$	$1\angle 0°$	0
$w^{GA}_{mm_3}$	$0.2\angle -156°$	0	$0.8\angle 70°$	$0.1\angle 151°$	0	0	$0.3\angle -105°$	$0.19\angle -105°$
$w^{GA}_{mm_4}$	$0.3\angle -166°$	$0.9\angle 156°$	$0.8\angle -126°$	$1\angle 144°$	0	$1\angle -89°$	$0.56\angle 37°$	$1\angle -98°$
$w^{GA}_{mm_5}$	$0.9\angle 101°$	$0.9\angle 53°$	$0.2\angle -82°$	$0.1\angle 100°$	$0.8\angle -172°$	$0.27\angle 88°$	$0.7\angle 139°$	$0.77\angle 7°$
$w^{GA}_{mm_6}$	$0.8\angle -86°$	$0.1\angle -37°$	$1\angle -118°$	$1\angle 103°$	$1\angle 0°$	$0.8\angle -54°$	$1\angle 127°$	0
$w^{GA}_{mm_7}$	$0.1\angle -157°$	0	$0.9\angle -48°$	$0.1\angle -12°$	$0.2\angle -152°$	$0.32\angle 177°$	$0.1\angle 30°$	0
$w^{GA}_{mm_8}$	$0.3\angle -166°$	$0.9\angle 107°$	$0.8\angle 117°$	$1\angle -23°$	$0.2\angle -145°$	$1\angle 0°$	$0.58\angle 163°$	$1\angle 0°$
$w^{GA}_{mm_9}$	$1\angle 0°$	$1\angle 0°$	$0.1\angle -65°$	$0.1\angle -26°$	$0.9\angle 117°$	$0.17\angle 81°$	$0.71\angle 13°$	$0.74\angle -59°$
$w^{GA}_{mm_{10}}$	$0.7\angle -153°$	$0.2\angle -93°$	$0.9\angle -71°$	$1\angle -63°$	$0.9\angle -72°$	$0.89\angle -51°$	$1\angle 2°$	$0.16\angle 174°$
$w^{GA}_{mm_{11}}$	$0.3\angle 105°$	$0.2\angle 19°$	$0.8\angle 0°$	$0.4\angle -172°$	0	0	$0.22\angle -102°$	0
$w^{GA}_{mm_{12}}$	0	$0.9\angle 54°$	$0.9\angle 163°$	$1\angle 170°$	$0.3\angle 1305°$	$0.79\angle 3°$	$0.51\angle 39°$	$1\angle 174°$
$w^{GA}_{mm_{13}}$	$1\angle 0°$	$0.9\angle -47°$	$0.2\angle -149°$	$0.2\angle 125°$	$0.8\angle -10°$	$0.21\angle 179°$	$0.63\angle 140°$	$0.84\angle 32°$
$w^{GA}_{mm_{14}}$	$0.7\angle 172°$	$0.1\angle -130°$	$0.9\angle 171°$	$0.9\angle 128°$	$0.9\angle 163°$	$1\angle 38°$	$0.79\angle 130°$	$0.25\angle -72°$
$w^{GA}_{mm_{15}}$	0	$0.2\angle -49°$	$0.8\angle -119°$	$0.2\angle 20°$	$0.2\angle 9°$	$0.14\angle -95°$	$0.18\angle 24°$	0
$w^{GA}_{mm_{16}}$	$0.3\angle 94°$	$0.9\angle 6°$	$0.7\angle 46°$	$1\angle 0°$	$0.3\angle -2°$	$0.85\angle 133°$	$0.62\angle 167°$	$1\angle 0°$
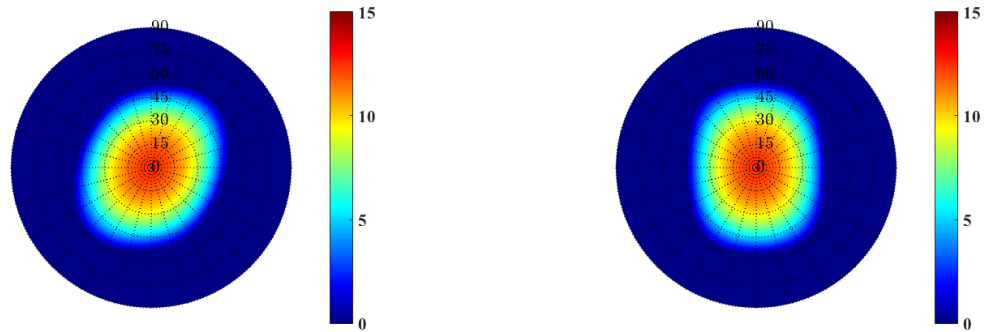
(a) The $\mathbf{w}_{mm}^{MGT}$ set; a maximum of 12.4 dBi.   (b) The $\mathbf{w}_{mm}^{GA}$ set; a maximum of 12.5 dBi.

Figure 6.6: The maximum gain patterns obtained for the $w_{mm_1}^{MGT,GA}, \ldots, w_{mm_{16}}^{MGT,GA}$ sets solved for and optimized, respectively, for the quad-mode antenna array at broadside.
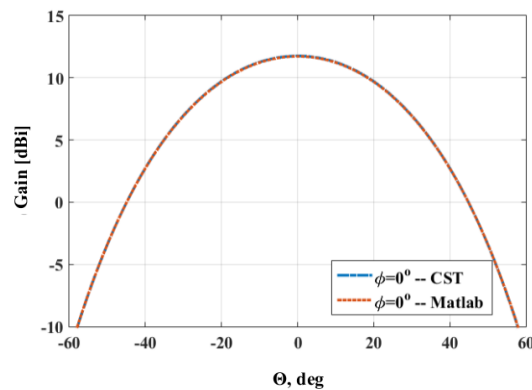

Figure 6.7: The 1-D gain of the solved $w_{mm_1}^{MGT}, \ldots, w_{mm_{16}}^{MGT}$ at broadside; the theoretical pattern is compared with CST simulated pattern.

6.3.2   The Genetic Algorithm Optimization for the $\mathcal{N}_{mm}^{GA}$ Set and the $\mathbf{w}_{QMA}^{GA}$ Set

Two sets of complex weighting functions are optimized to steer the antenna beam to a maximum gain, which is the multi-mode excitation set that determines each single antenna's radiation pattern and the set of complex weighting functions that excites each antenna within the array configuration. For clarity, the implementation of a 2×2 quad-mode antenna array optimization is illustrated in Figure 6.11. The $\mathbf{w}_{QMA}^{GA} = [w_{QMA_1}^{GA}, \ldots, w_{QMA_4}^{GA}]$ set is the excited complex weights applied to each quad-mode antenna and $\mathcal{N}_{mm}^{GA} = [\mathcal{N}_{mm_1}^{GA}, \ldots, \mathcal{N}_{mm_4}^{GA}]$ denotes the four multi-mode excitation weights. By varying eight complex weighting functions, which is the set of $\mathcal{N}_{mm}^{GA}$ excitations and the set of $\mathbf{w}_{QMA}^{GA}$, a combination of the two sets are obtained that steers the beam pattern towards a desired direction.

The GA optimization technique is used and the quad-mode antenna array gain pattern G^A is obtained by first calculating the single quad-mode antenna gain pattern for the set of optimized $\mathcal{N}_{mm}^{GA}$ excitations. That is,

$$G(\theta, \phi) = \frac{4\pi}{\eta} \left[\frac{|\sum_{n=1}^{4} \mathcal{N}_{mm_n}^{GA} f_{mm_n}^{\theta}(\theta, \phi)|^2 + |\sum_{n=1}^{4} \mathcal{N}_{mm_n}^{GA} f_{mm_n}^{\phi}(\theta, \phi)|^2}{[\mathcal{N}_{mm}^{GA}]^H [I - \mathbf{S}[\mathbf{S}]^H] \mathcal{N}_{mm}^{GA}} \right], \qquad (6.3.17)$$
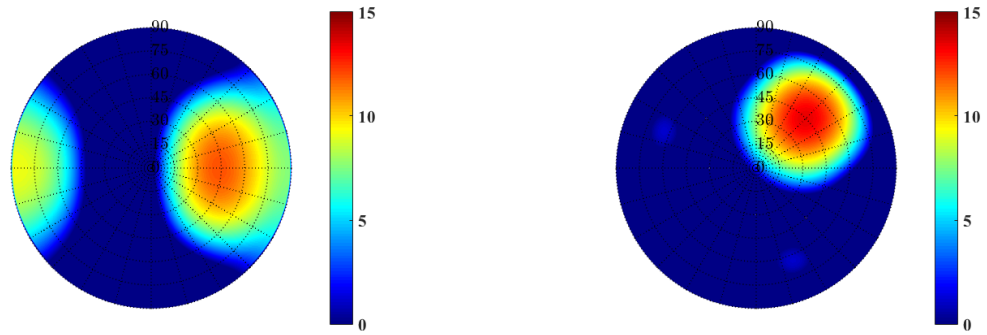
(a) $\theta = 45°$, $\phi = 0°$; a maximum of 11.97 dBi. (b) $\theta = 45°$, $\phi = 45°$ a maximum of 13.5 dBi.
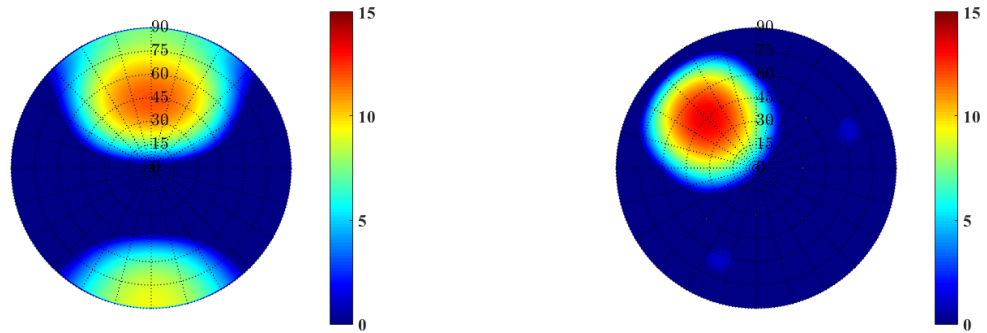
(c) $\theta = 45°$, $\phi = 90°$; a maximum of 11.97 dBi.(d) $\theta = 45°$, $\phi = 135°$; a maximum of 13.5 dBi.
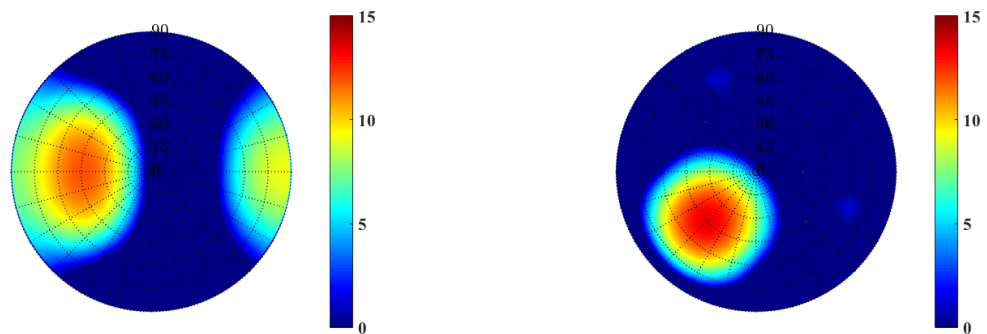
(e) $\theta = 45°$, $\phi = 180°$ a maximum of 11.97 dBi.(f) $\theta = 45°$, $\phi = 225°$; a maximum of 13.5 dBi.
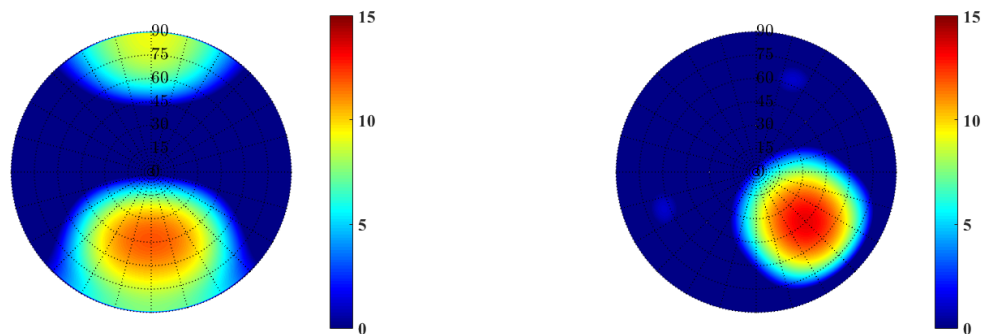
(g) $\theta = 45°$, $\phi = 270°$; a maximum of 11.97 dBi.(h) $\theta = 45°$, $\phi = 315°$; a maximum of 13.5 dBi.

Figure 6.8: Gain pattern in $[dBi]$ for a 2×2 quad-mode antenna array excited by the solved set of $w_{mm_1}^{MGT}, \ldots, w_{mm_{16}}^{MGT}$.
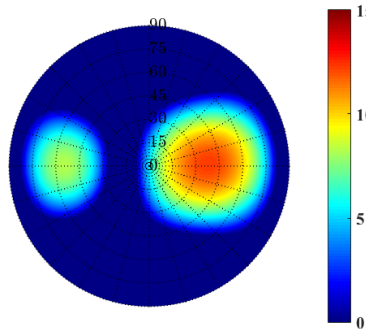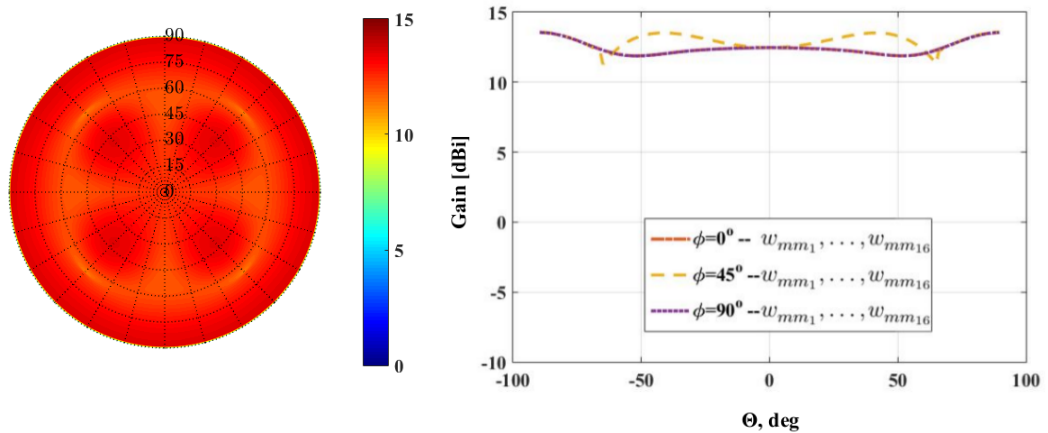
(a) $\theta = 45°$, $\phi = 0°$; maximum of 12.5 dBi.   (b) $\theta = 45°$, $\phi = 45°$; maximum of 13.3 dBi.
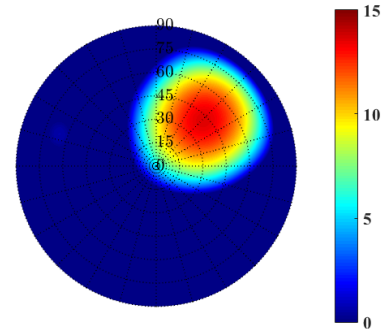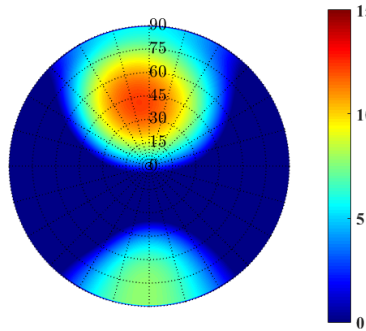
(c) $\theta = 45°$, $\phi = 90°$; maximum of 11.65 dBi. (d) $\theta = 45°$, $\phi = 135°$; maximum of 11.67 dBi.
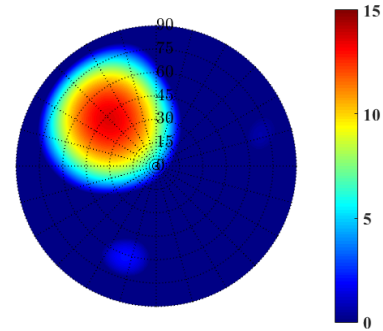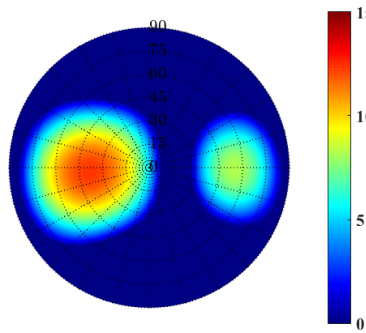
(e) $\theta = 45°$, $\phi = 180°$; maximum of 12.5 dBi. (f) $\theta = 45°$, $\phi = 225°$; maximum of 12.5 dBi.
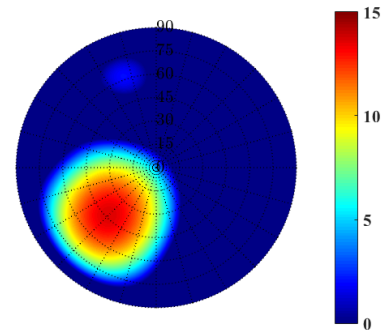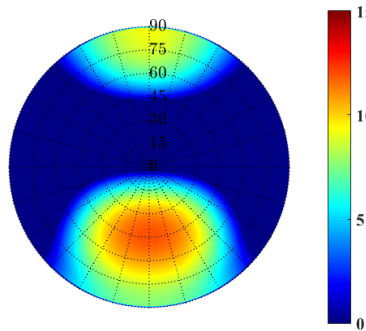
(g) $\theta = 45°$, $\phi = 270°$; maximum of 12.5 dBi. (h) $\theta = 45°$, $\phi = 315°$; maximum of 12.5 dBi.
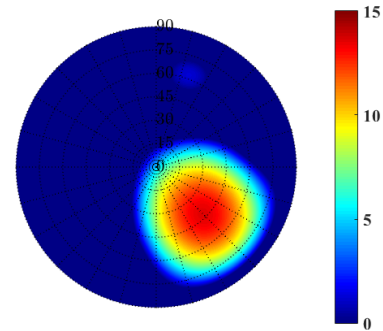
Figure 6.9: Gain pattern in $[dBi]$ for a 2×2 quad-mode antenna array excited by the solved set of $w_{mm_1}^{GA}, \ldots, w_{mm_{16}}^{GA}$.

Figure 6.10: $w^{MGT}_{mm_1}, \ldots, w^{MGT}_{mm_{16}}$ set; maximum of 13.6 dBi and minimum of 11.3 dBi.
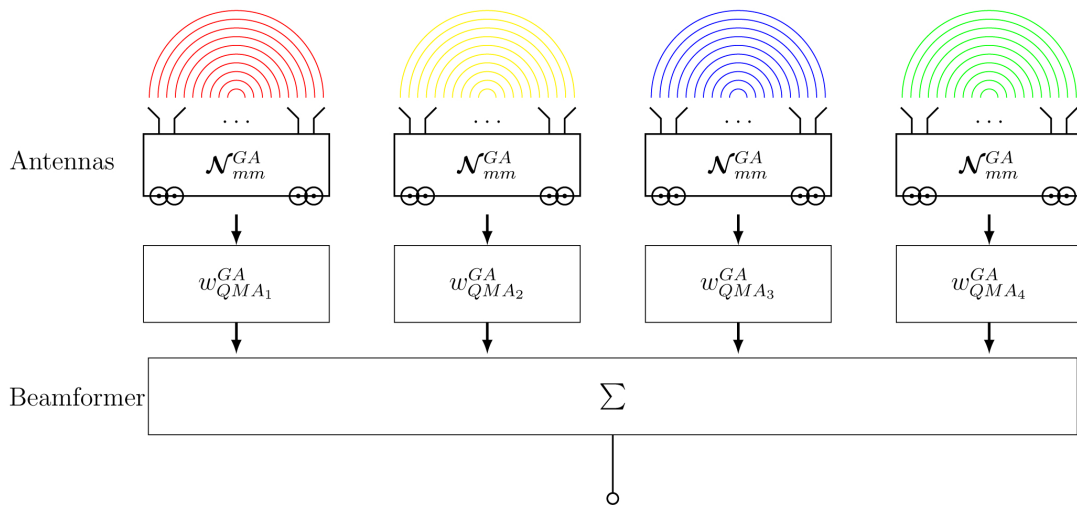
Figure 6.11: A representation of a 2×2 quad-mode antenna array optimization for the complex multi-mode $\mathcal{N}^{GA}_{mm}$ excitation set and four antennas excitation set $\mathbf{w}^{GA}_{QMA}$.

where $\mathbf{S}$ and f_{mm_n} are the single quad-mode antenna scattering matrix and far-field vector extracted from CST. Using the obtained element gain, the principle of pattern multiplication will be applied, with the array factor given in Equation (2.4.2) and the array gain obtained as,

$$G^A(\theta, \phi) = G(\theta, \phi)|AF(\theta, \phi)|^2, \tag{6.3.18}$$

The array gain is maximized as,

$$G_{max} = \max_{\mathcal{N}^{GA}_{mm}, \mathbf{w}^{GA}_{QMA}} G^A(\theta_0, \phi_0) \quad \forall \quad \left(0° \leq \theta_0 \leq 90°; 0° \leq \phi_0 \leq 360°\right) \tag{6.3.19}$$

and changing the weighting functions to achieve a maximum beam towards the desired angular directions of θ_0 and ϕ_0. A mathematical representation of the fitness function is given as,

$$\min_{\mathcal{N}_{mm}, \mathbf{w}_{QMA}} F = G - G_{max} \quad \forall \quad \left(0° \leq \theta_0 \leq 90°; 0° \leq \phi_0 \leq 360°\right) \tag{6.3.20}$$

over the hemispheric FoV coverage, which is $\left(0° \leq \theta_0 \leq 90°; 0° \leq \phi_0 \leq 360°\right)$. The fitness value is minimized through maximizing the array gain and where G is chosen to
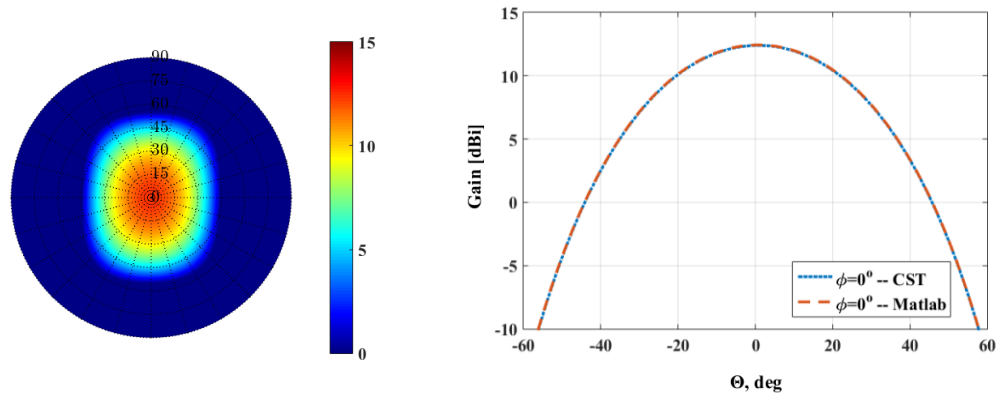
(a) $0°, 0°$; maximum of $12\ dBi$.

(b) Theoretical gain pattern compared with CST simulation.

Figure 6.12: Gain pattern in $[dBi]$ maximized at broadside given the optimized $\mathcal{N}_{mm}^{GA}$ and $\mathbf{w}_{QMA}^{GA}$.

be larger than the maximum array gain obtained from the $w_{mm_1}, \ldots, w_{mm_{16}}$ set which is the optimal set of multi-mode excitation for a 2×2 quad-mode antenna array.

The maximum gain pattern at $\theta = 0°$, $\phi = 0°$ yields the set of complex weighting functions given in Equation (6.3.21), and the corresponding gain pattern is depicted in Figure 6.12a. The theoretical gain pattern maximized to broadside is compared with the CST full wave simulated gain pattern as shown in Figure 6.12b. The mathematically calculated and simulated gain patterns correspond well. The foregoing formulation above yields the following result which is optimized for broadside,

$$\begin{bmatrix} \mathcal{N}_{mm_1}^{GA} \\ \mathcal{N}_{mm_2}^{GA} \\ \mathcal{N}_{mm_3}^{GA} \\ \mathcal{N}_{mm_4}^{GA} \end{bmatrix} = \begin{bmatrix} 0.8\underline{/12°} \\ 1\underline{/0°} \\ 0 \\ 0 \end{bmatrix}, \quad \begin{bmatrix} w_{QMA_1}^{GA} \\ w_{QMA_2}^{GA} \\ w_{QMA_3}^{GA} \\ w_{QMA_4}^{GA} \end{bmatrix} = \begin{bmatrix} 0.98\underline{/28°} \\ 0.97\underline{/28°} \\ 0.98\underline{/28°} \\ 0.83\underline{/28°} \end{bmatrix}. \tag{6.3.21}$$

In Table (6.3) the normalized complex weighting function is presented for the desired angular directions for a constant θ at $= 45°$ and ϕ starts at $0°$ with $45°$ increments. Figure 6.13 depicts the corresponding gain patterns achieved. The obtained results shows the optimal set of multi-mode excitation weights at each corresponding scanned angle for the 2×2 array configuration. The normalized complex weighting function in Table (6.3) correlates with solved and optimized results in Tables (6.1) – (6.2). Therefore, by varying both the antenna's weighting functions and the multi-mode excitations an optimal set of weighting functions are obtained, which correspond to the respective angle of optimization.
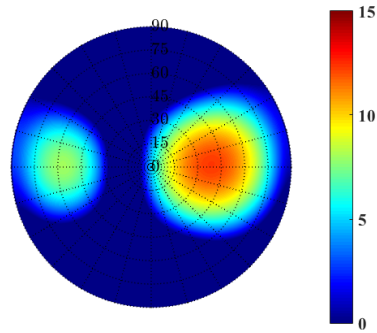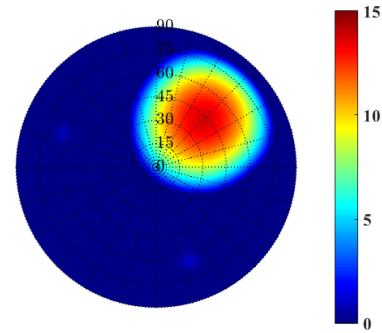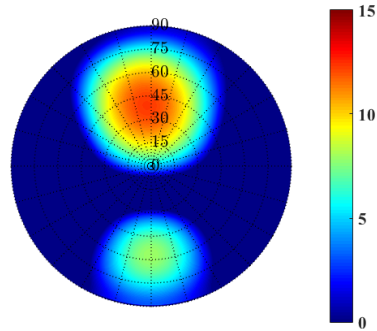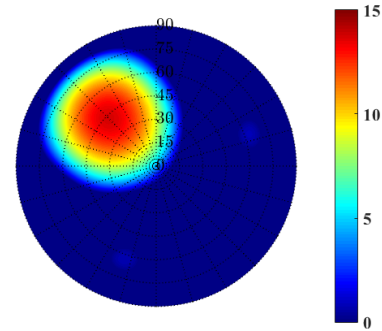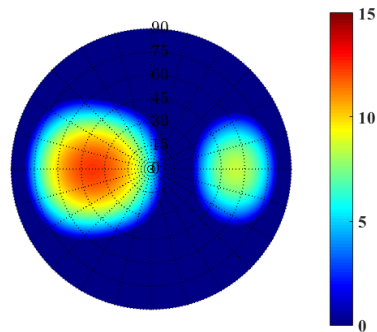
(a) $\theta = 45°$, $\phi = 0°$; maximum of 12 dBi.

(b) $\theta = 45°$, $\phi = 45°$; maximum of 15 dBi.

(c) $\theta = 45°$, $\phi = 90°$; maximum of 13 dBi.

(d) $\theta = 45°$, $\phi = 135°$; maximum of 14 dBi.

(e) $\theta = 45°$, $\phi = 180°$; maximum of 12 dBi.
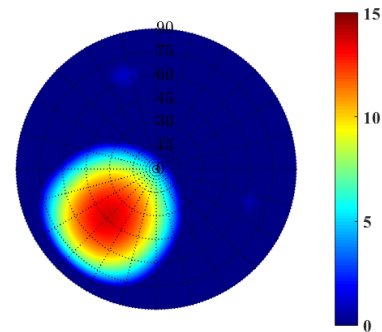
(f) $\theta = 45°$, $\phi = 225°$; maximum of 14 dBi.
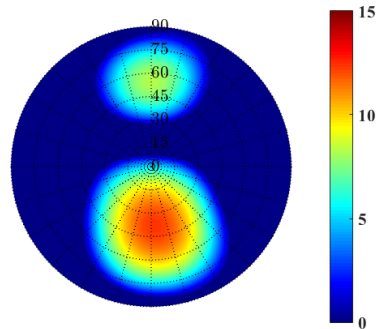
(g) $\theta = 45°$, $\phi = 270°$; maximum of 13 dBi.
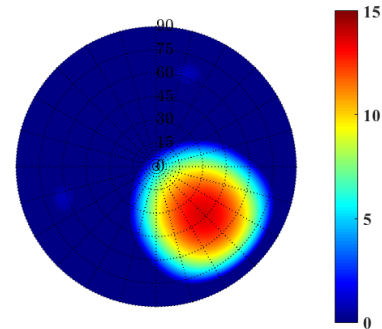
(h) $\theta = 45°$, $\phi = 315°$; maximum of 15 dBi.

Figure 6.13: Gain pattern in $[dBi]$ for the optimized $\mathcal{N}_{mm}^{GA}$ set and $\mathbf{w}_{QMA}^{GA}$ set; the GA optimization.

Table 6.3: 8 Complex Weights Optimized using the Genetic Algorithm

θ, ϕ	$45°, 0°$	$45°, 45°$	$45°, 90°$	$45°, 135°$	$45°, 180°$	$45°, 225°$	$45°, 270°$	$45°, 315°$
$\mathcal{N}^{GA}_{mm_1}$	$1\angle 0°$	0	$0.38\angle 141°$	$0.5\angle{-53°}$	$0.5\angle 51°$	0	$0.23\angle{-40°}$	$0.5\angle 127°$
$\mathcal{N}^{GA}_{mm_2}$	$0.85\angle{-179°}$	$0.52\angle 127°$	$1\angle 130°$	0	$0.2\angle 143°$	$0.5\angle{-52°}$	$0.8\angle 53°$	0
$\mathcal{N}^{GA}_{mm_3}$	0	0	$0.4\angle{-139°}$	0	$0.4\angle 41°$	0	$0.37\angle{-139°}$	0
$\mathcal{N}^{GA}_{mm_4}$	$0.2\angle{-125°}$	$1\angle 0°$	$1\angle 0°$	$1\angle 0°$	$1\angle 0°$	$1\angle 0°$	$1\angle 0°$	$1\angle 0°$
$w^{GA}_{QMA_1}$	$1\angle 0°$	$1\angle 0°$	$1\angle 0°$	$1\angle 0°$	$1\angle 0°$	$1\angle 0°$	$1\angle 0°$	$1\angle 0°$
$w^{GA}_{QMA_2}$	$1\angle 0°$	$1\angle{-88°}$	$1\angle{-128°}$	$1\angle{-92°}$	$1\angle{-2°}$	$1\angle 88°$	$1\angle 127°$	$1\angle 91°$
$w^{GA}_{QMA_3}$	$1\angle{-127°}$	$1\angle{-90°}$	$1\angle{-3°}$	$1\angle 88°$	$1\angle 127°$	$1\angle 92°$	$1\angle 0°$	$1\angle{-88°}$
$w^{GA}_{QMA_4}$	$1\angle{-127°}$	$1\angle{-180°}$	$1\angle{-130°}$	$1\angle 0°$	$1\angle 124°$	$1\angle 180°$	$1\angle 129°$	$1\angle 3°$

6.3.3 The Maximum-Gain Theorem and Optimizations Techniques for the $\mathcal{X}_{mm}$, $\mathcal{B}_{mm}$, and w^{MGT}_{QMA} Sets
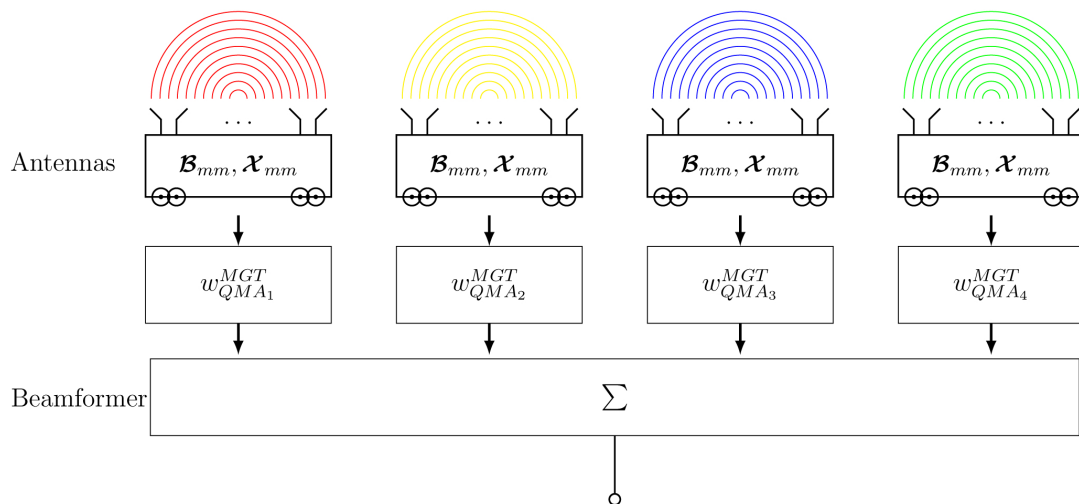

Figure 6.14: A representation of a 2×2 quad-mode antenna array optimization for the complex multi-mode $\mathcal{X}_{mm}, \mathcal{B}_{mm}$ excitation sets and four antennas excitation set $\mathbf{w}^{MGT}_{QMA}$.

For clarification, a representation of the optimization process to be implemented is given in Figure 6.14. An optimal set of combinational multi-mode excitation weights is obtained that provides a relatively constant amplitude variation for various scanned angles. The optimization technique performed here is based on a similar concept as discussed in [23]. The theorem states that there exists a solution of excitations in a finite set that will obtain an equilibrium point.

This is done through optimizing the multi-mode excitation weights of the $\mathcal{X}_{mm}$ set and the $\mathcal{B}_{mm}$ set, using optimization toolboxes in MATLAB the GA solver and the FMINSEARCH solver, respectively, to achieve a $G^A_{max}([\mathcal{X}^*_{mm}, \mathcal{B}^*_{mm}], \Omega^*)$ which is the point where the gain will converge for both sets of weights.

The FMINSEARCH tool is a linear optimizer and is based on the Nelder-Mead algorithm. The function looks for a local minimum by minimizing the fitness value defined in the

fitness function. The algorithm is faster than the GA and works well if the solution set is close to the initial value.

Throughout this subsection the following notation will be adopted for the ease of reading; the $\boldsymbol{\mathcal{X}}_{mm} = [\mathcal{X}_{mm_1} \dots, \mathcal{X}_{mm_4}]$ set will denote the GA optimization and the $\boldsymbol{\mathcal{B}}_{mm} = [\mathcal{B}_{mm_1} \dots, \mathcal{B}_{mm_4}]$ set will denote the FMINSEARCH optimization.

The optimization technique is given by obtaining the equilibrium points $G_{max}^A(\boldsymbol{\mathcal{X}}_{mm}^*, \Omega^*)$ and $G_{max}^A(\boldsymbol{\mathcal{B}}_{mm}^*, \Omega^*)$ where $\boldsymbol{\mathcal{X}}_{mm}$ and $\boldsymbol{\mathcal{B}}_{mm}$, respectively, are the complex weighting functions that will change as the algorithm looks for the maximum value of minimum G_{max}^A values over the hemisphere $(\theta^*, \phi^*) = \Omega^*$. For each combinational set of multi-mode excitations, $\boldsymbol{\mathcal{X}}_{mm}$ and $\boldsymbol{\mathcal{B}}_{mm}$, the fitness function will calculate the gain pattern of the quad-mode antenna, as given in Equation (6.3.17). The algorithm continues by obtaining the complex beamforming weighting functions $[\mathbf{w}_{QMA}^{MGT}]^H$ solved by the maximum-gain theorem for a maximum beam pattern G_{max}^A at each scanned angle. That is,

$$\max_{\boldsymbol{\mathcal{X}}_{mm}, \boldsymbol{\mathcal{B}}_{mm}} G_{max}^A([\boldsymbol{\mathcal{X}}_{mm}, \boldsymbol{\mathcal{B}}_{mm}], \Omega^*) = G_{max}^A([\boldsymbol{\mathcal{X}}_{mm}^*, \boldsymbol{\mathcal{B}}_{mm}^*], \Omega^*) = \min_{\Omega} G_{max}^A([\boldsymbol{\mathcal{X}}_{mm}^*, \boldsymbol{\mathcal{B}}_{mm}^*], \Omega),$$
$$(6.3.22)$$

in order to obtain the optimum sets of solution vectors $\boldsymbol{\mathcal{X}}_{mm}$ and $\boldsymbol{\mathcal{B}}_{mm}$. The maximum-gain theorem will solve the complex weighting functions $[\mathbf{w}_{QMA}^{MGT}]^H = [w_{QMA_1}^{MGT}]^*, \dots, [w_{QMA_4}^{MGT}]^*$ by using a conjugate-field matching technique, as discussed above. By doing this the maximum gain values at each scanned angle over the hemisphere Ω are obtained. That is,

$$\max_{\mathbf{w}_{QMA}^{MGT}} G_{max}^A(\theta_0, \phi_0) \quad \forall \ (\ \theta_0, \ \phi_0 \ ) \text{ start} = 0° \text{ with } 5° \text{ increments.} \qquad (6.3.23)$$

The lowest maximum gain value over the hemisphere can be obtained by,

$$G_{min}^A = \min_{\theta_0, \phi_0} G_{max}^A, \qquad (6.3.24)$$

and the fitness value will be implemented as,

$$F = G - G_{min}^A, \qquad (6.3.25)$$

where $G = 15 \ dBi$ is the hypothetical maximum that the array gain can achieve. This fitness function will converge and an equilibrium will be achieved. Thus obtaining the sets of $\boldsymbol{\mathcal{X}}_{mm}$ and $\boldsymbol{\mathcal{B}}_{mm}$ excitations that provide a constant amplitude to each scanned angle. The foregoing formulation above yields the results given in Equation (6.3.26) for the $\boldsymbol{\mathcal{B}}_{mm}$ set, optimized through repeatedly running the FMINSEARCH optimization.

$$\begin{bmatrix} \mathcal{B}_{mm_1} \\ \mathcal{B}_{mm_2} \\ \mathcal{B}_{mm_3} \\ \mathcal{B}_{mm_4} \end{bmatrix} = \begin{bmatrix} 0.68\underline{/0°} \\ 0.66\underline{/0°} \\ 0.7\underline{/0°} \\ 1\underline{/0°} \end{bmatrix}. \qquad (6.3.26)$$

Each iteration is set with a new set of initial values. The function forms a simplex close to the initial solution set, as discussed in [20], therefore the optimization problem is improved by choosing the initial set close to the solution set. The $\boldsymbol{\mathcal{B}}_{mm}$ set presented in Equation (6.3.26) yields the results where the $\mathbf{w}_{QMA}^{MGT}$ set is solved for maximum gain at broadside; Figure 6.15a depicts the 2-D embedded element gain pattern and Figure 6.15b compares the theoretical embedded element gain pattern to the simulated far-field array in CST using the embedded element pattern. The results show that when scanned to broadside
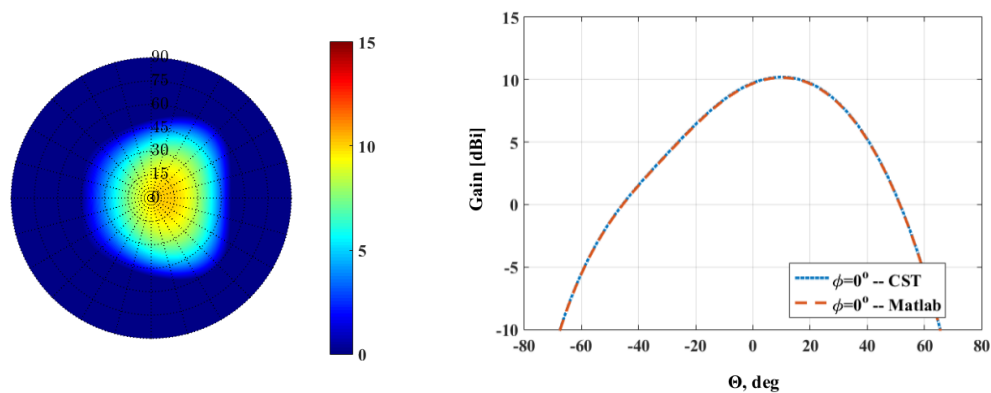
(a) $\theta = 0°$, $\phi = 0°$; a maximum of 10.2 dBi.

(b) Theoretical gain pattern is compared with CST simulation.

Figure 6.15: Gain pattern in $[dBi]$ for the optimized $\boldsymbol{\mathcal{B}}_{mm}$ multi-mode excitation weights and the $\mathbf{w}_{QMA}^{MGT}$ set complex beamforming weights for broadside.

the theoretically implemented and the simulated 2×2 array configuration compare well. The set is further investigated, as shown in Figure 6.16, with the desired angular directions of a constant θ at $45°$ and ϕ starts at $0°$ with $45°$ increments. The results show that higher gain values are obtained between the angular directions of $-90° < \phi < 90°$ at $\theta = 45°$. This is due to the radiation pattern produced by the $\boldsymbol{\mathcal{B}}_{mm}$ set for a single quad-mode antenna that has a higher gain towards the one side.

The maximum gain values over a hemispheric FoV coverage are depict in Figure 6.17 with a gain variation of 7.3 dBi.

The GA optimization is implemented here for the problem defined above, the solution set is given in Equation (6.3.27) for the optimized $\boldsymbol{\mathcal{X}}_{mm}$ set.

$$
\begin{bmatrix}
\mathcal{X}_{mm_1} \\
\mathcal{X}_{mm_2} \\
\mathcal{X}_{mm_3} \\
\mathcal{X}_{mm_4}
\end{bmatrix}
=
\begin{bmatrix}
0.6\underline{/8°} \\
0.6\underline{/-158°} \\
1\underline{/0°} \\
0.9\underline{/167°}
\end{bmatrix}
\tag{6.3.27}
$$

Figure 6.18a depicts the 2-D embedded element gain pattern when scanned towards broadside. The theoretical embedded element gain pattern corresponds to the simulated far-field array pattern in CST at broadside, as shown in Figure 6.18b. Furthermore, the embedded element gain pattern results obtained for the desired angular directions of a constant θ at $= 45°$ and ϕ starts at $0°$ with $45°$ increments, are shown in Figure 6.19.

Figure 6.20 depicts the maximum gain values of the embedded element pattern obtained for the quad-mode antenna array using the $\boldsymbol{\mathcal{X}}_{mm}$ excitation set; the figure shows a 2-D gain pattern and 1-D $\phi-$planes. A gain variation of 2.7 dBi is achieved.

The results show that the GA optimizer yields a more hemispheric beam pattern with a significantly smaller gain variation. This is due to its robustness and global iterative process.
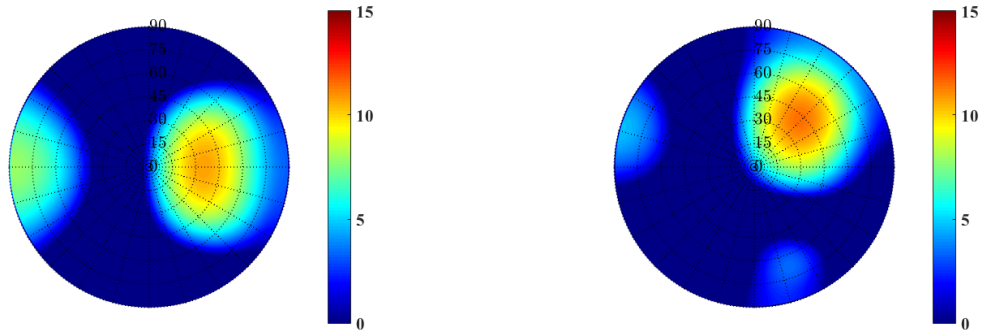
(a) $\theta = 45°$, $\phi = 0°$; maximum of 10.8 dBi.

(b) $\theta = 45°$, $\phi = 45°$; maximum of 11.5 dBi.
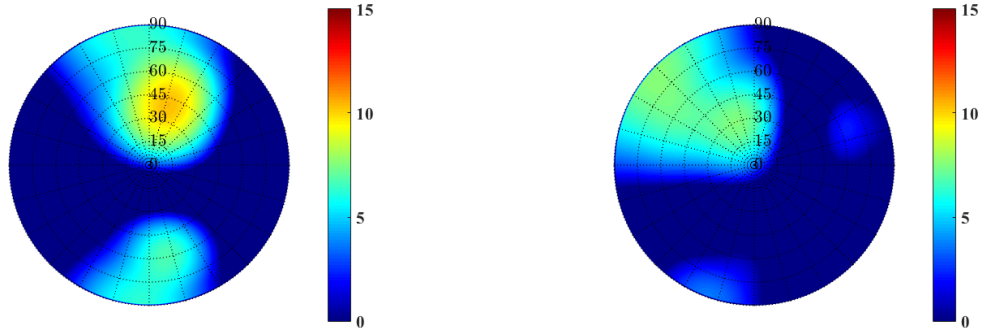
(c) $\theta = 45°$, $\phi = 90°$; maximum of 10.4 dBi.

(d) $\theta = 45°$, $\phi = 135°$; maximum of 7.6 dBi.
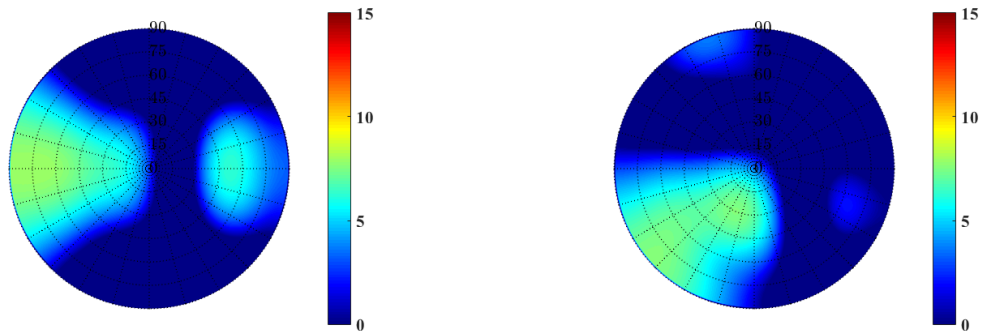
(e) $\theta = 45°$, $\phi = 180°$; maximum of 7.9 dBi.

(f) $\theta = 45°$, $\phi = 225°$; maximum of 7.6 dBi.
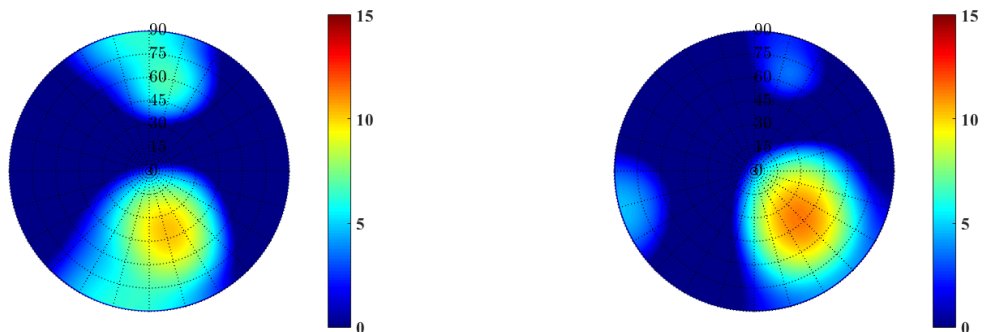
(g) $\theta = 45°$, $\phi = 270°$; maximum of 10.3 dBi.

(h) $\theta = 45°$, $\phi = 315°$; maximum of 11.4 dBi.

Figure 6.16: Gain pattern in $[dBi]$ for the optimized $\mathcal{B}_{mm}$ set and the $\mathbf{w}_{QMA}^{MGT}$ set.
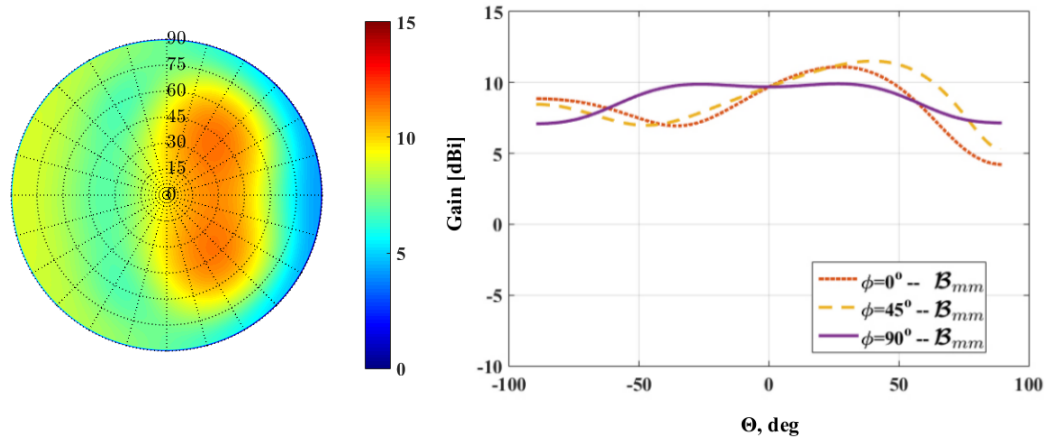
Figure 6.17: $\boldsymbol{\mathcal{B}}_{mm}$ set; maximum of 11.5 dBi and minimum of 4.2 dBi.
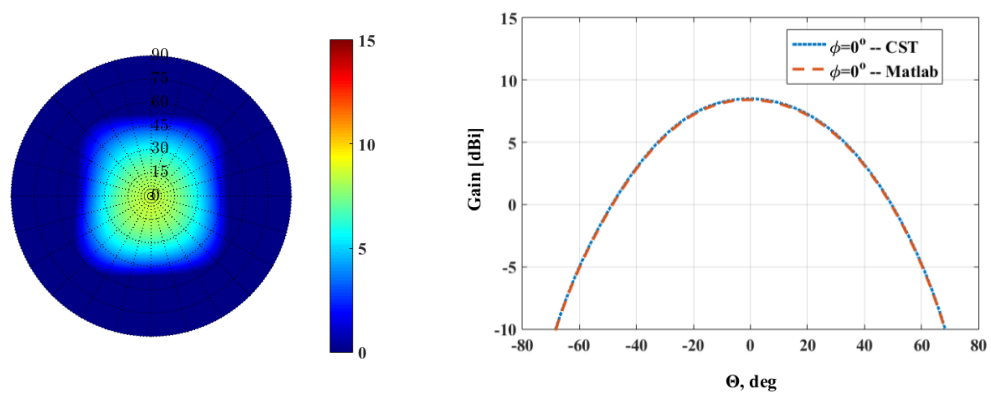
(a) $\theta = 0°$, $\phi = 0°$; maximum of 8.5 dBi.

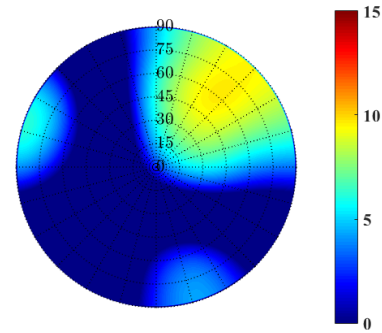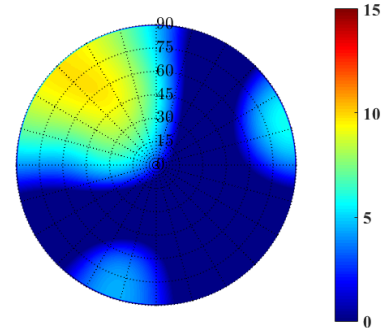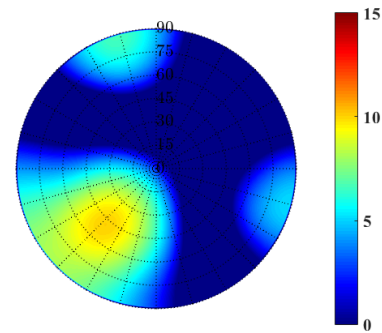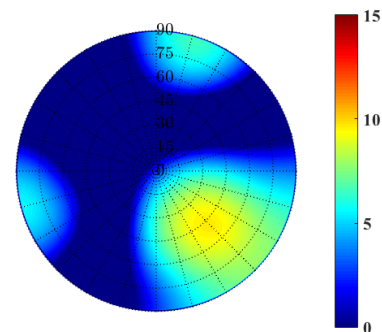(b) Theoretical gain pattern is compared with CST simulation.

Figure 6.18: Gain pattern in $[dBi]$ for the optimized $\boldsymbol{\mathcal{X}}_{mm}$ multi-mode excitation weights and the $\mathbf{w}_{QMA}^{MGT}$ set complex beamforming weights for broadside.

6.3.4 The Maximum-Gain Theorem Implemented for the $\boldsymbol{\Upsilon}_{mm}$, $\boldsymbol{\varrho}_{mm}$ and $\mathbf{w}_{QMA}^{MGT}$ Sets

The set of beamforming weighting functions $[\mathbf{w}_{QMA}^{MGT}]^H = [w_{QMA_1}^{MGT}]^*, \ldots, [w_{QMA_4}^{MGT}]$ is solved using the conjugate-field matching technique [6]. For clarity, Figure 6.21 represents the method using the multi-mode pattern $\boldsymbol{\Upsilon}_{mm}$ and $\boldsymbol{\varrho}_{mm}$ obtained in Chapter 4 and configuring it into a 2×2 quad-mode antenna array.

Each set of multi-mode excitation weights, $\boldsymbol{\Upsilon}_{mm}$ and $\boldsymbol{\varrho}_{mm}$, has an unique electric field pattern, given in Section 4.3, which can be expressed as $\mathbf{F}_{QMA_n}^{\boldsymbol{\Upsilon}}$ and $\mathbf{F}_{QMA_n}^{\boldsymbol{\varrho}}$, respectively. These are the field vectors: $\mathbf{F}_{QMA_1}^{\boldsymbol{\Upsilon},\boldsymbol{\varrho}}$ is used to represent the electric field distribution of the antenna positioned at $(0,0)$; $\mathbf{F}_{QMA_2}^{\boldsymbol{\Upsilon},\boldsymbol{\varrho}}$ represents the field vector of the antenna position $(0,d)$; $\mathbf{F}_{QMA_3}^{\boldsymbol{\Upsilon},\boldsymbol{\varrho}}$ represents the field vector of the antenna position $(d,0)$ and $\mathbf{F}_{QMA_4}^{\boldsymbol{\Upsilon},\boldsymbol{\varrho}}$ represents the field vector of the antenna position (d,d).

The complex excitation $[w_{QMA_1}^{MGT}]^*$ is applied to the quad-mode antenna positioned at the origin. The second antenna will be excited by $[w_{QMA_2}^{MGT}]^*$ which is situated at $(0,d)$. The third and fourth antenna will be excited with the $[w_{QMA_3}^{MGT}]^*$ and $[w_{QMA_4}^{MGT}]^*$ sets which are situated at $(d,0)$ and (d,d), respectively. The $[\mathbf{w}_{QMA}^{MGT}]^H = [w_{QMA_1}^{MGT}]^*, \ldots, [w_{QMA_4}^{MGT}]^*$ set is solved using the maximum-gain beamforming theorem, as discussed in Subsection 6.3.1
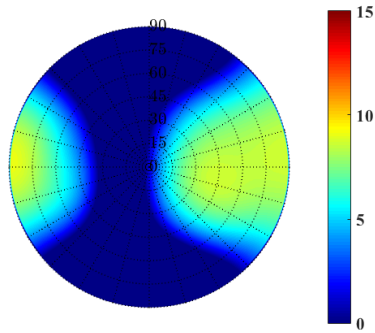
(a) $\theta = 45°$, $\phi = 0°$; maximum of 9.1 dBi.   (b) $\theta = 45°$, $\phi = 45°$; maximum of 9.7 dBi.
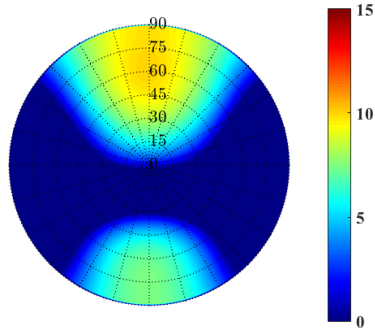
(c) $\theta = 45°$, $\phi = 90°$; maximum of 10 dBi.   (d) $\theta = 45°$, $\phi = 135°$; maximum of 9.8 dBi.
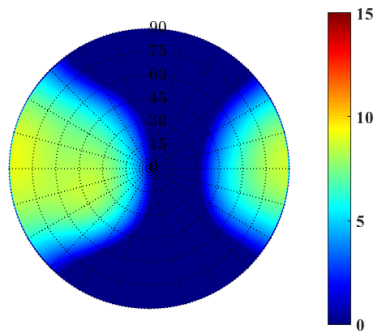
(e) $\theta = 45°$, $\phi = 180°$; maximum of 9.1 dBi.   (f) $\theta = 45°$, $\phi = 225°$; maximum of 10.1 dBi.
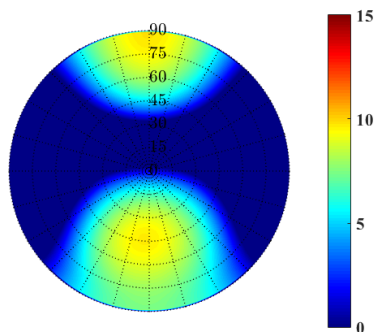
(g) $\theta = 45°$, $\phi = 270°$; maximum of 9.78 dBi.   (h) $\theta = 45°$, $\phi = 315°$; maximum of 9.67 dBi.

Figure 6.19: Gain pattern in $[dBi]$ for the optimized $\boldsymbol{\mathcal{X}}_{mm}$ set and the $\mathbf{w}_{QMA}^{MGT}$ set.
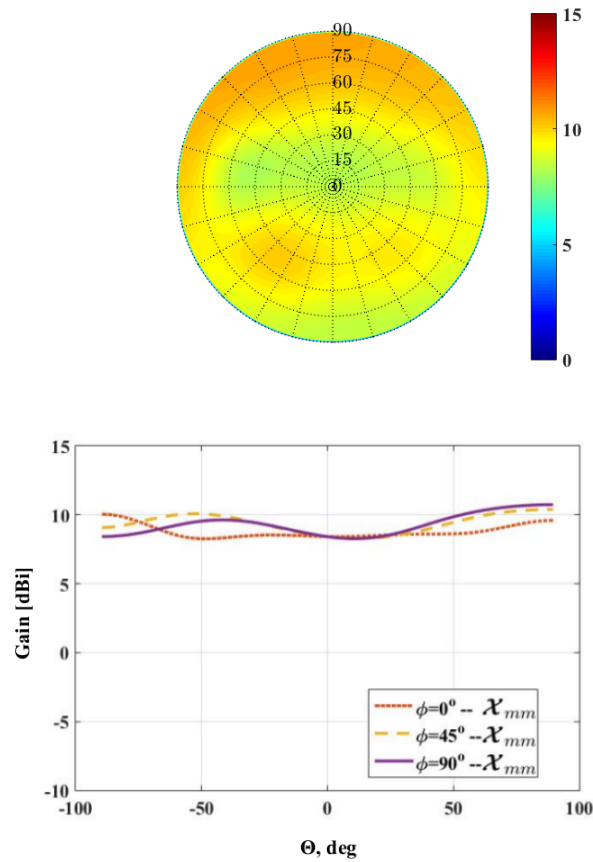
Figure 6.20: $\boldsymbol{\mathcal{X}}_{mm}$ set; maximum of 10.8 dBi and minimum 8.1 dBi.
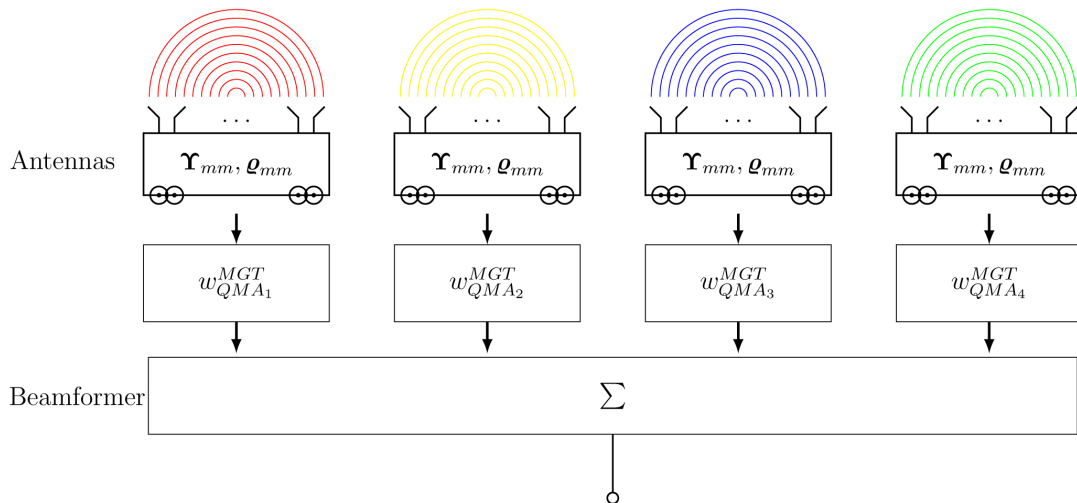

Figure 6.21: A representation of a 2×2 quad-mode antenna array optimization for the complex multi-mode $\boldsymbol{\Upsilon}_{mm}$, $\boldsymbol{\varrho}_{mm}$ excitation sets and four antennas excitation set $\mathbf{w}_{QMA}^{MGT}$.

for sixteen complex weights.

The array field vector $\mathbf{F}_T^{\boldsymbol{\Upsilon},\boldsymbol{\varrho}}$, which is the input vector to the beamformer, is a two-dimensional vector with four excitation element patterns. Equation (6.3.28) defines the far-field radiation pattern with a relative phase shift depending on the quad-mode an-

tenna's position vector as follows,

$$
\mathbf{F}_T^{\mathbf{\Upsilon},\boldsymbol{\varrho}} = \begin{bmatrix}
f_{QMA_1}^{\mathbf{\Upsilon},\boldsymbol{\varrho}} & \hat{\boldsymbol{\theta}} & & f_{QMA_1}^{\mathbf{\Upsilon},\boldsymbol{\varrho}} & & \hat{\boldsymbol{\phi}} \\
f_{QMA_2}^{\mathbf{\Upsilon},\boldsymbol{\varrho}} & e^{jk_0\frac{\lambda}{2}\beta_y}\ \hat{\boldsymbol{\theta}} & & f_{QMA_2}^{\mathbf{\Upsilon},\boldsymbol{\varrho}} & e^{jk_0\frac{\lambda}{2}\beta_y} & \hat{\boldsymbol{\phi}} \\
f_{QMA_3}^{\mathbf{\Upsilon},\boldsymbol{\varrho}} & e^{jk_0\frac{\lambda}{2}\beta_x}\ \hat{\boldsymbol{\theta}} & & f_{QMA_3}^{\mathbf{\Upsilon},\boldsymbol{\varrho}} & e^{jk_0\frac{\lambda}{2}\beta_x} & \hat{\boldsymbol{\phi}} \\
f_{QMA_4}^{\mathbf{\Upsilon},\boldsymbol{\varrho}} & e^{jk_0\frac{\lambda}{2}(\beta_y+\beta_x)}\ \hat{\boldsymbol{\theta}} & & f_{QMA_4}^{\mathbf{\Upsilon},\boldsymbol{\varrho}} & e^{jk_0\frac{\lambda}{2}(\beta_y+\beta_x)} & \hat{\boldsymbol{\phi}}
\end{bmatrix}, \tag{6.3.28}
$$

where the progressive phase delay is given in Equation (2.4.3) and the propagation constant in free space is given in Equation (2.2.2). The weighted array gain is given as,

$$
G^A = \frac{4\pi}{\eta} \left[\frac{\mathbf{w}_{QMA}^H \mathbf{F}_T^{\mathbf{\Upsilon},\boldsymbol{\varrho}} [\mathbf{F}_T^{\mathbf{\Upsilon},\boldsymbol{\varrho}}]^H \mathbf{w}_{QMA}^{MGT}}{[\mathbf{w}_{QMA}^{MGT}]^H \left[I - \mathbf{S}^A [\mathbf{S}^A]^H \right] \mathbf{w}_{QMA}^{MGT}} \right], \tag{6.3.29}
$$

where η is the free space impedance. The scattering matrix $\mathbf{S}^A$ for the ideal 2×2 array configuration, where mutual coupling effects have been neglected, is given by,

$$
\mathbf{S}^A = \begin{bmatrix}
\Gamma^{\mathbf{\Upsilon},\boldsymbol{\varrho}} & 0 & 0 & 0 \\
0 & \Gamma^{\mathbf{\Upsilon},\boldsymbol{\varrho}} & 0 & 0 \\
0 & 0 & \Gamma^{\mathbf{\Upsilon},\boldsymbol{\varrho}} & 0 \\
0 & 0 & 0 & \Gamma^{\mathbf{\Upsilon},\boldsymbol{\varrho}}
\end{bmatrix}, \tag{6.3.30}
$$

and $\Gamma^{\mathbf{\Upsilon},\boldsymbol{\varrho}}$ is the reflection coefficient obtained from CST full wave simulation of the $\mathbf{F}_{QMA_n}^{\mathbf{\Upsilon}}$ and $\mathbf{F}_{QMA_n}^{\boldsymbol{\varrho}}$ quad-mode antenna patterns and are given as $\Gamma^{\mathbf{\Upsilon}} = 0.0265\underline{/144^\circ}$ at 2 GHz and $\Gamma^{\boldsymbol{\varrho}} = 0.04267\underline{/104^\circ}$ at 2 GHz.

The weighted array gain in Equation (6.3.29) is maximized by solving the $[\mathbf{w}_{QMA}^{MGT}]^H$ set for the largest root of the eigenvector problem defined in the Equation (6.3.11).

The $\mathbf{\Upsilon}_{mm}$ set optimized in Chapter 4 is implemented in a quad-mode antenna array configuration and each antenna is optimized to steer the beam pattern to a maximum over the hemisphere. The normalized sets of complex beamforming weights $\mathbf{w}_{QMA}^{MGT}$ are solved for broadside and given in Equation (6.3.31). Figure 6.22 depicts the corresponding gain pattern for the normalized $\mathbf{w}_{QMA}^{MGT}$ set at broadside, $\theta = 0^\circ, \phi = 0^\circ$.

$$
\begin{bmatrix}
w_{QMA_1}^{MGT} \\
w_{QMA_2}^{MGT} \\
w_{QMA_3}^{MGT} \\
w_{QMA_4}^{MGT}
\end{bmatrix} = \begin{bmatrix}
1\underline{/0^\circ} \\
1\underline{/0^\circ} \\
1\underline{/0^\circ} \\
1\underline{/0^\circ}
\end{bmatrix}. \tag{6.3.31}
$$

Figure 6.23 compares the theoretical embedded element gain pattern obtained using the $\mathbf{w}_{QMA}^{MGT}$ set at broadside with the CST full wave simulated gain pattern, the solved solution compares well with the simulated gain pattern. From the results in Table (6.4) it can be concluded that the amplitudes of the complex weighting function are identical for each element. The relative progressive phase delay can be seen in Figure 6.24, for the steered angular directions of a constant θ at 45° and ϕ starts at 0° with 45° increments. The maximum gain values over a hemispheric FoV coverage for the quad-mode antenna array are depicted in Figure 6.25. The highest maximum value achieved is 11.4 dBi which is roughly between the angles of $35^\circ < \theta < 40^\circ$ and $280^\circ < \phi < 300^\circ$ as shown in Figure 6.25.

The $\boldsymbol{\varrho}_{mm}$ set optimized in Chapter 4 is implemented in a quad-mode antenna array configuration and each antenna is optimized to steer the beam pattern to a maximum over the hemisphere. Figure 6.26 depicts the corresponding gain pattern for the normalized $\mathbf{w}_{QMA}^{MGT}$ set, given in Equation (6.3.31), at broadside. The theoretically implemented array is compared with the CST full wave simulated gain pattern in Figure 6.27 at broadside. Figure 6.28 presents a selected set of the data, the results show that the implemented quad-mode antenna array pattern steers the beam's maximum radiation pattern to a desired angular direction of $\theta = 45°$ for various ϕ values. The maximum gain values over a hemispheric FoV coverage for the quad-mode antenna array are depicted in Figure 6.29. A approximately flat constant maximum gain is achieved over the hemispheric FoV coverage, as shown in Figure 6.29 with an overall gain variation of roughly 3.8 dBi. The figures show that by using the $\boldsymbol{\varrho}_{mm}$ set to excite each quad-mode antenna within the array configuration, a high gain value is achieved when scanned to various angles.
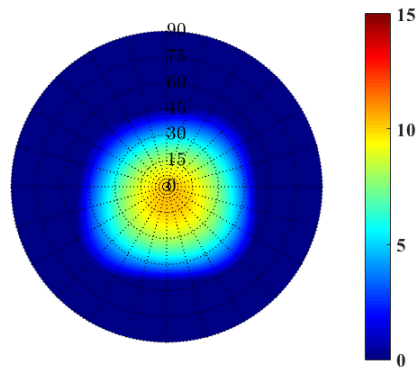
Figure 6.22: Gain pattern of the $\boldsymbol{\Upsilon}_{mm}$ excitation weights in $[dBi]$ at broadside; a maximum of 10.4 dBi.
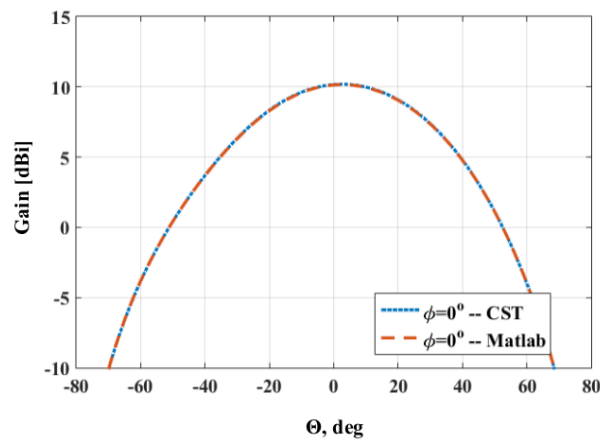
Figure 6.23: The 1-D gain pattern of the $\boldsymbol{\Upsilon}_{mm}$ excitation weights optimized for maximum at broadside; the theoretical pattern for the solved $\mathbf{w}_{QMA}^{MGT}$ set is compared with CST simulated patterns.

Table 6.4: Complex Weights Obtained from the Maximum-Gain Theorem

θ, ϕ	$45°, 0°$	$45°, 45°$	$45°, 90°$	$45°, 135°$	$45°, 180°$	$45°, 225°$	$45°, 270°$	$45°, 315°$
$w_{QMA_1}^{MGT}$	$1\underline{/0°}$	$1\underline{/0°}$	$1\underline{/0°}$	$1\underline{/0°}$	$1\underline{/0°}$	$1\underline{/0°}$	$1\underline{/0°}$	$1\underline{/0°}$
$w_{QMA_2}^{MGT}$	$1\underline{/0°}$	$1\underline{/-90°}$	$1\underline{/-127°}$	$1\underline{/-90°}$	$1\underline{/0°}$	$1\underline{/90°}$	$1\underline{/127°}$	$1\underline{/90°}$
$w_{QMA_3}^{MGT}$	$1\underline{/-127°}$	$1\underline{/-90°}$	$1\underline{/0°}$	$1\underline{/90°}$	$1\underline{/127°}$	$1\underline{/90°}$	$1\underline{/0°}$	$1\underline{/-90°}$
$w_{QMA_4}^{MGT}$	$1\underline{/-127°}$	$1\underline{/-180°}$	$1\underline{/-127°}$	$1\underline{/0°}$	$1\underline{/127°}$	$1\underline{/180°}$	$1\underline{/127°}$	$1\underline{/0°}$

6.3.5 Compare The Quad-Mode Antenna Multi-Mode Excitation Sets

The four optimized multi-mode networks are compared here. The maximum-gain theorem $w_{mm_1}^{MGT}, \ldots, w_{mm_{16}}^{MGT}$ set of weights is used here and denoted as $w_{mm_1}, \ldots, w_{mm_{16}}$. The results show that the sixteen multi-mode excitation weights $w_{mm_1}, \ldots, w_{mm_{16}}$ obtains the best set of maximum gain values over the hemisphere, as illustrated in Figure 6.30. This is due to the fact that all sixteen multi-mode excitation weights are modifiable and thus
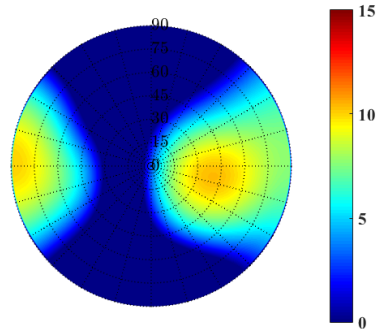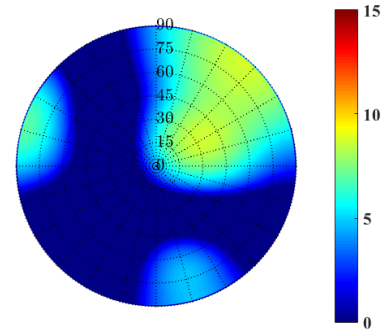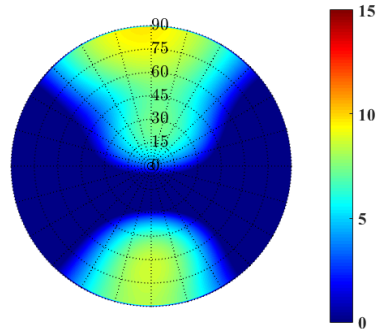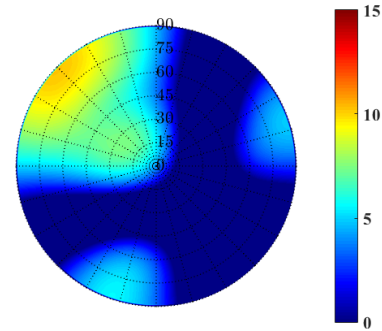
(a) $\theta = 45°$, $\phi = 0°$; maximum of 10.4 dBi.

(b) $\theta = 45°$, $\phi = 45°$; maximum of 8.7 dBi.

(c) $\theta = 45°$, $\phi = 90°$; maximum of 9.7 dBi.

(d) $\theta = 45°$, $\phi = 135°$; maximum of 10.2 dBi.
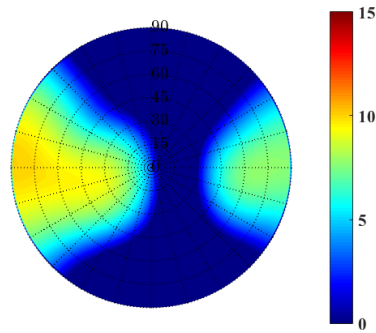
(e) $\theta = 45°$, $\phi = 180°$; maximum of 10.1 dBi.
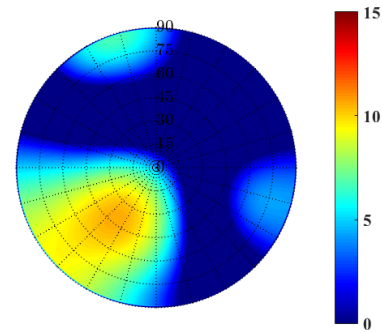
(f) $\theta = 45°$, $\phi = 225°$; maximum of 10.6 dBi.
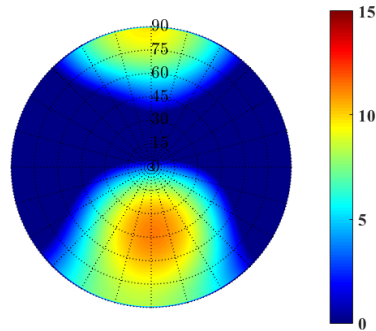
(g) $\theta = 45°$, $\phi = 270°$; maximum of 11.3 dBi.
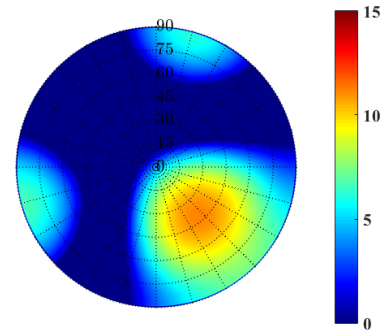
(h) $\theta = 45°$, $\phi = 315°$; maximum of 11.2 dBi.

Figure 6.24: Gain pattern in $[dBi]$ for the solved $\mathbf{w}_{QMA}^{MGT}$ set of the quad-mode antenna array, excited by $\mathbf{\Upsilon}_{mm}$ set.
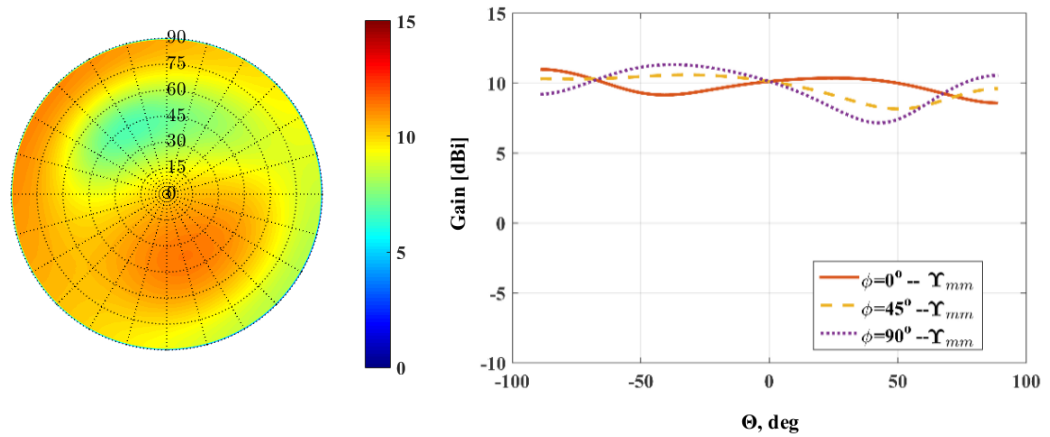
Figure 6.25: $\mathbf{\Upsilon}_{mm}$ set; a maximum of 11.4 dBi and minimum of 6.7 dBi.
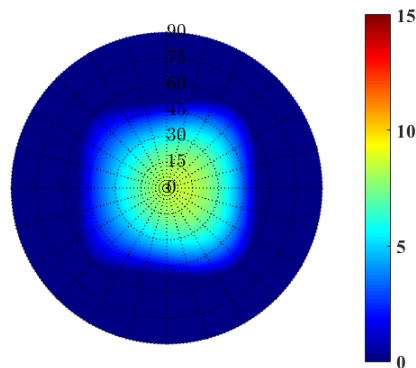
Figure 6.26: Gain pattern in $[dBi]$ for the quad-mode antenna array at broadside, excited by the $\boldsymbol{\varrho}_{mm}$ set and the $\mathbf{w}_{QMA}^{MGT}$; maximum of 8.6 dBi.
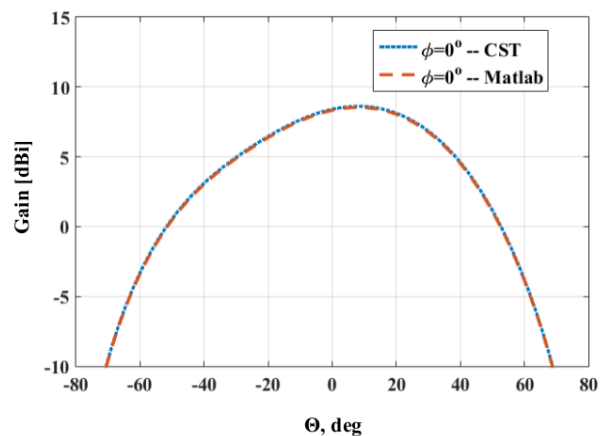

Figure 6.27: The 1-D gain pattern of the $\boldsymbol{\varrho}_{mm}$ excitation weights optimized for maximum at broadside; the theoretical pattern for the solved $\mathbf{w}_{QMA}^{MGT}$ set is compared with CST simulated patterns.
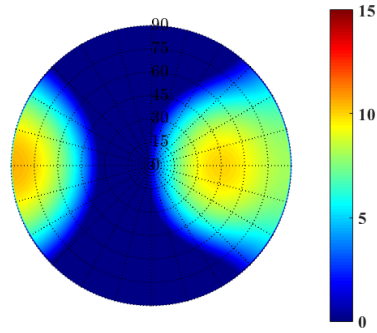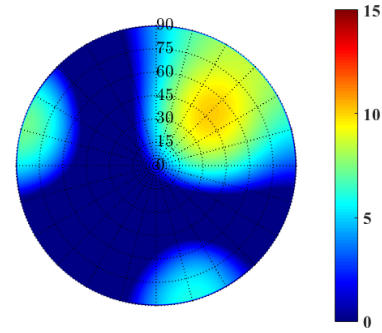
(a) $\theta = 45°$, $\phi = 0°$; maximum of 10.5 dBi.   (b) $\theta = 45°$, $\phi = 45°$; maximum of 10.1 dBi.
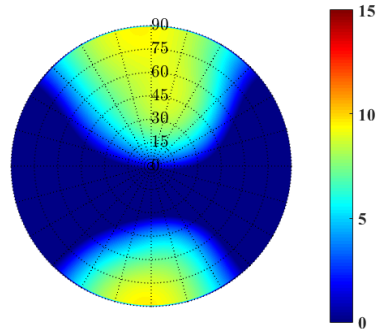
(c) $\theta = 45°$, $\phi = 90°$; maximum of 9.6 dBi.   (d) $\theta = 45°$, $\phi = 135°$; maximum of 10.3 dBi.
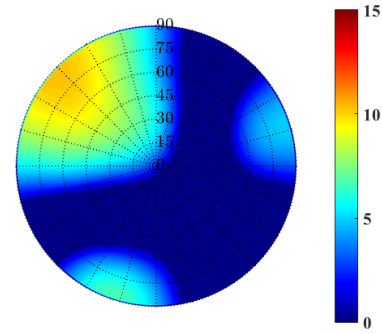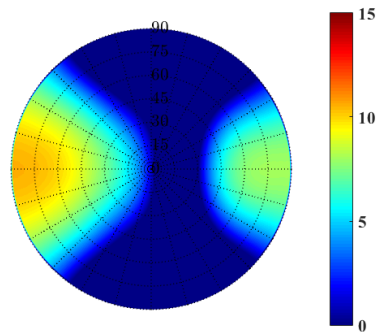
(e) $\theta = 45°$, $\phi = 180°$; maximum of 10.5 dBi.   (f) $\theta = 45°$, $\phi = 225°$; maximum of 10.4 dBi.
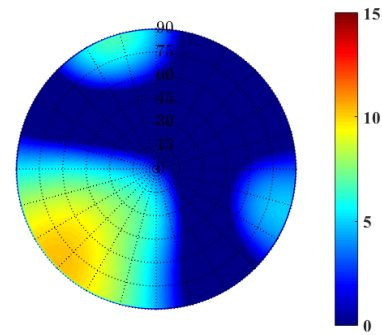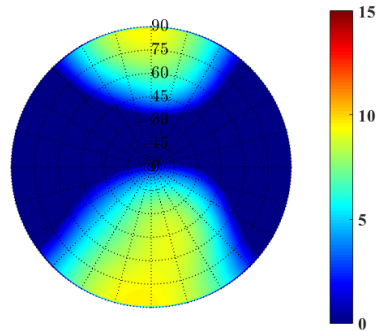
(g) $\theta = 45°$, $\phi = 270°$; maximum of 9.6 dBi.   (h) $\theta = 45°$, $\phi = 315°$; maximum of 10.2 dBi.
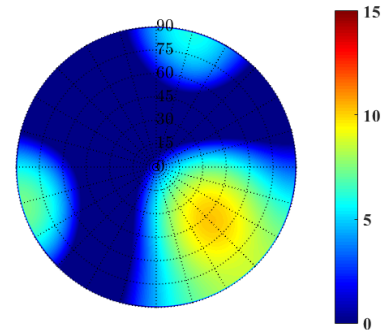
Figure 6.28: Gain pattern in $[dBi]$ for a 2×2 quad-mode antenna array, excited by the $\boldsymbol{\varrho}_{mm}$ set and the $\mathbf{w}_{QMA}^{MGT}$.
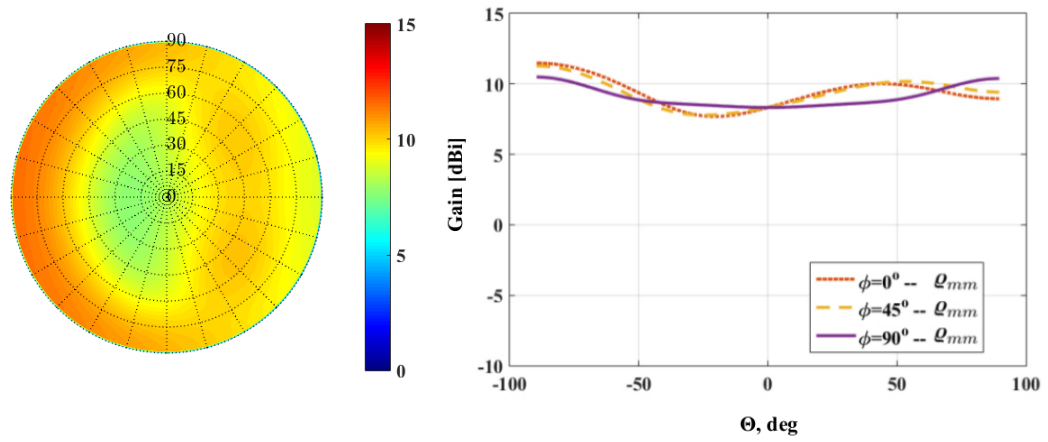
Figure 6.29: $\boldsymbol{\varrho}_{mm}$ set; maximum of 11.5 dBi and minimum 7.7 dBi.

the best achievable maximum gain values are seen for the set of $w_{mm_1}, \ldots, w_{mm_{16}}$. In Table (6.5) the lowest achieved maximum gain values and gain variations for each multi-mode set are given. A higher gain is achieved for the $\boldsymbol{\mathcal{B}}_{mm}$ and $\boldsymbol{\Upsilon}_{mm}$ set but it is also a more directive gain, therefore the overall hemispheric maximum gain is lower. By observing the maximum gain achieved for the $\boldsymbol{\varrho}_{mm}$ and $\boldsymbol{\mathcal{X}}_{mm}$ sets over the hemispheric FoV coverage a constant gain variation is depicted. The results show the $\boldsymbol{\mathcal{X}}_{mm}$ set achieves an approximately constant maximum gain value over the hemisphere, with a gain variation of 2.7 dBi, which makes it the optimum set of multi-mode excitations obtained.

Table 6.5: Four multi-mode sets compares; gain variation ΔG^A and lowest maximum gain G^A_{min}.

Multi-Mode set	G^A_{min}	ΔG^A
$\boldsymbol{\varrho}_{mm}$	7.7 dBi	3.8 dBi
$\boldsymbol{\mathcal{X}}_{mm}$	8.1 dBi	2.7 dBi
$\boldsymbol{\mathcal{B}}_{mm}$	4.2 dBi	7.3 dBi
$\boldsymbol{\Upsilon}_{mm}$	6.7 dBi	4.7 dBi
$w_{mm_1}, \ldots, w_{mm_{16}}$	11.3 dBi	2.3 dBi

Figure 6.30: The maximum gain over a hemispheric FoV coverage for each set of multi-modes.

(a) 3-D 2×2 quad-mode antenna array config-
uration drawn in CST.

(b) 1-D representation quad-mode antenna ar-
ray.

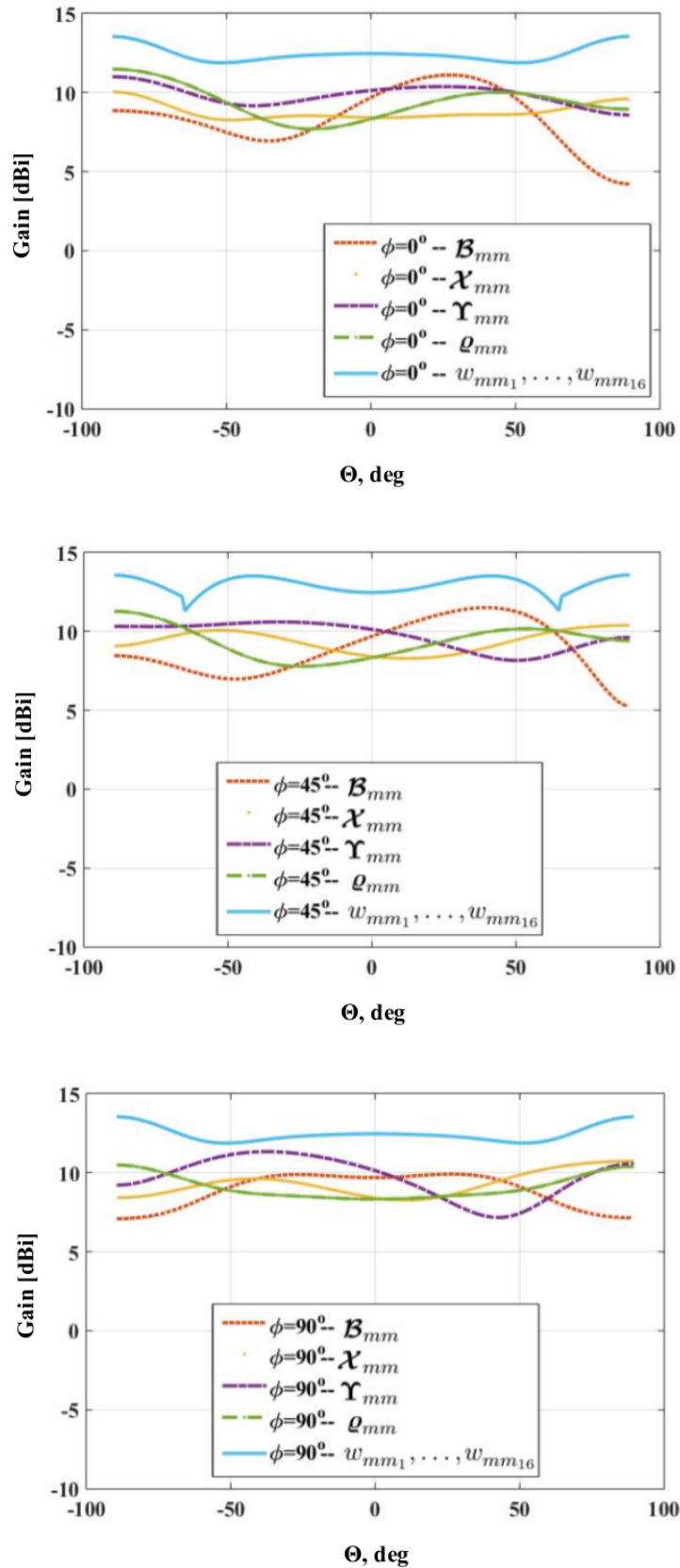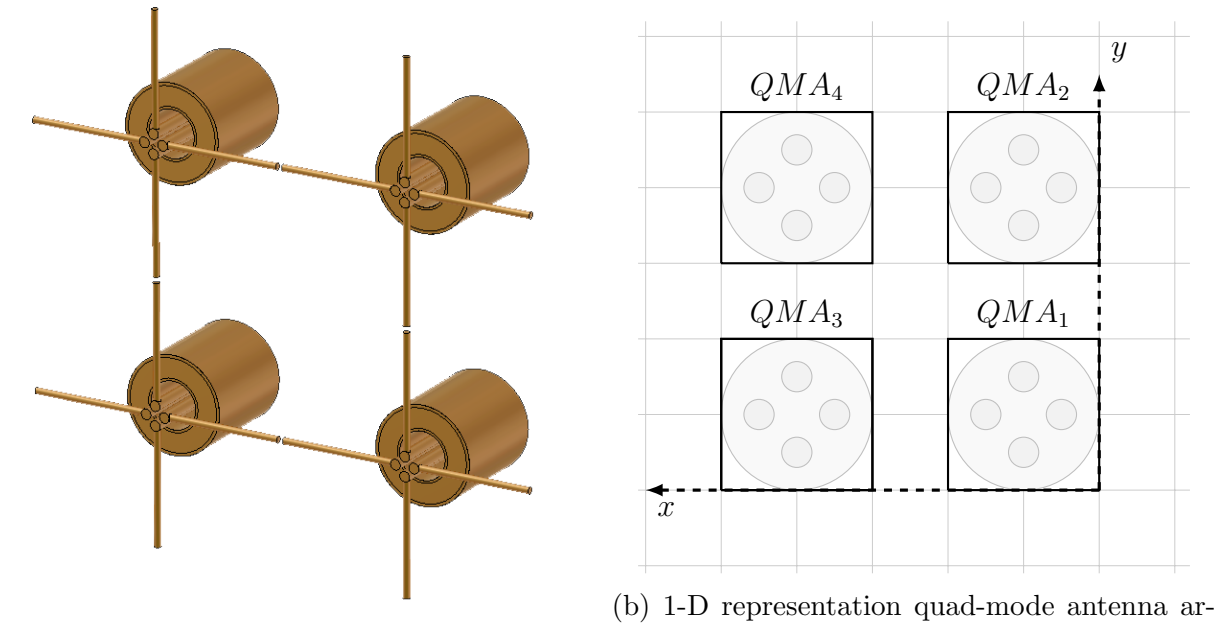Figure 6.31: A 2×2 quad-mode antenna array configuration.

6.4   Implementations of Various 2×2 Quad-mode Antenna Array

As previously mentioned, an ideal array neglects mutual coupling effects which degrades the radiation pattern of the array. These mutual coupling effects can be seen from the far-field patterns of a 2×2 quad-mode antenna array drawn in CST, as shown in Figure 6.31. This array is compared here with two mathematically implemented 2×2 quad-mode antenna arrays, where the isolated and embedded element patterns are used and mathematically shifted in MATLAB.

The actual array pattern far-field θ- and ϕ- components are extracted as $f_{mm_1}^{\theta,\phi}(\theta, \phi) \ldots f_{mm_{16}}^{\theta,\phi}(\theta, \phi)$. The quad-mode antenna array pattern is steered to a desired direction with an angular direction of θ and ϕ over a hemispheric FoV coverage. This is done by multiplying the extracted field vectors with the solved set of complex conjugate beamforming weighting functions $[\mathbf{w}_{mm}^{MGT}]^H = [w_{mm_1}^{MGT}]^*, \ldots, [w_{mm_{16}}^{MGT}]^*$, obtained in Subsection 6.3.1. Each quad-mode antenna in the array can be excited with a different set of multi-mode excitations that will allow a different radiation pattern for each antenna within the array. The power radiated per unit solid angle of the simulated quad-mode antenna array is calculated as follows,

$$P_{rad} = [\mathbf{w}_{mm}^{MGT}]^H [I - \mathbf{S}^A [\mathbf{S}^A]^H] \mathbf{w}_{mm}^{MGT}, \tag{6.4.1}$$

and the array scattering matrix $\mathbf{S}^A$ is extracted from the CST simulated quad-mode antenna array. The gain given in Equation (2.2.9) is used to calculate the quad-mode antenna array gain. Further, the radiation intensity of the array is given by,

$$U^A(\theta, \phi) = \frac{1}{\eta} \left[\left| \sum_{n=1}^{N} [w_{mm_n}^{MGT}]^* f_{mm_n}^{\theta}(\theta, \phi) \right|^2 + \left| \sum_{n=1}^{N} [w_{mm_n}^{MGT}]^* f_{mm_n}^{\phi}(\theta, \phi) \right|^2 \right], \tag{6.4.2}$$

where η is the free space impedance. The simulated 2×2 quad-mode antenna array patterns can be calculated as follows,

$$G^A(\theta, \phi) = 4\pi \frac{U^A(\theta, \phi)}{P_{rad}}. \tag{6.4.3}$$

The isolated and embedded quad-mode antenna elements are simulated using the CST far-field array function for a 2×2 array configuration and are weighted for a desired angular direction. In this case the array is steered to broadside $\theta_0 = 0°, \phi_0 = 0°$, and $\theta_0 = 45°, \phi_0 = 45°$.

The single quad-mode antenna's embedded element pattern is simulated in CST through the periodic boundary condition function and is extracted here as,

$$\mathbf{F}^E_{mm_n} = \begin{bmatrix} f^{\theta,\phi}_{mm_1}(\theta, \phi) \\ \vdots \\ f^{\theta,\phi}_{mm_4}(\theta, \phi) \end{bmatrix}. \tag{6.4.4}$$

Using the property of pattern multiplication, discussed in Section 2.4, the embedded element pattern is mathematically implemented in a 2×2 array grid as,

$$[\mathbf{F}_T]_n = \begin{bmatrix} f^E_{mm_1}\hat{\boldsymbol{\theta}} & f^E_{mm_1}\hat{\boldsymbol{\phi}} \\ \vdots & \vdots \\ f^E_{mm_4}\hat{\boldsymbol{\theta}} & f^E_{mm_4}\hat{\boldsymbol{\phi}} \\ f^E_{mm_1}e^{jk_0\frac{\lambda}{2}(\beta_y)}\hat{\boldsymbol{\theta}} & f^E_{mm_1}e^{jk_0\frac{\lambda}{2}(\beta_y)}\hat{\boldsymbol{\phi}} \\ \vdots & \vdots \\ f^E_{mm_4}e^{jk_0\frac{\lambda}{2}(\beta_y)}\hat{\boldsymbol{\theta}} & f^E_{mm_4}e^{jk_0\frac{\lambda}{2}(\beta_y)}\hat{\boldsymbol{\phi}} \\ f^E_{mm_1}e^{jk_0\frac{\lambda}{2}(\beta_x)}\hat{\boldsymbol{\theta}} & f^E_{mm_1}e^{jk_0\frac{\lambda}{2}(\beta_x)}\hat{\boldsymbol{\phi}} \\ \vdots & \vdots \\ f^E_{mm_4}e^{jk_0\frac{\lambda}{2}(\beta_x)}\hat{\boldsymbol{\theta}} & f^E_{mm_4}e^{jk_0\frac{\lambda}{2}(\beta_x)}\hat{\boldsymbol{\phi}} \\ f^E_{mm_1}e^{jk_0\frac{\lambda}{2}(\beta_y+\beta_x)}\hat{\boldsymbol{\theta}} & f^E_{mm_1}e^{jk_0\frac{\lambda}{2}(\beta_y+\beta_x)}\hat{\boldsymbol{\phi}} \\ \vdots & \vdots \\ f^E_{mm_4}e^{jk_0\frac{\lambda}{2}(\beta_y+\beta_x)}\hat{\boldsymbol{\theta}} & f^E_{mm_4}e^{jk_0\frac{\lambda}{2}(\beta_y+\beta_x)}\hat{\boldsymbol{\phi}} \end{bmatrix}. \tag{6.4.5}$$

The beam pattern is steered to a desired direction by summing all the embedded element patterns and multiplying it with the conjugate weighting function $\mathbf{w}^{MGT}_{mm}$ obtained in Subsection 6.3.1. The gain pattern of the mathematically implemented 2×2 quad-mode antenna array is calculated as,

$$G^A = \frac{4\pi}{\eta} \frac{\left| \sum_{n=1}^{16} [w^{MGT}_{mm_n}]^* [\mathbf{F}_T]_n \right|^2}{P_{rad}}, \tag{6.4.6}$$

where η is the free space impedance. Author in [9] shows that classic array theory can be applied to the embedded element pattern. The total radiated power of a lossless antenna element is $P_{rad} = P_{in}$, which is calculated as follows,

$$P_{rad} = [\mathbf{w}^{MGT}_{mm}]^H \big[I - \mathbf{S}^A [\mathbf{S}^A]^H \big] [\mathbf{w}^{MGT}_{mm}]. \tag{6.4.7}$$

The scattering parameters of the embedded element pattern is extracted from CST as $\mathbf{S}^E$ and if the array is considered to be large enough so that each antenna element sees the same neighbouring environment, an ideal S-matrix of an array is approximated in [9], and can be used here to calculate the S-matrix as,

$$
\mathbf{S}^A = \left[\begin{array}{cccc} [\mathbf{S}^E] & 0 & \ldots & 0 \\ 0 & [\mathbf{S}^E] & & \vdots \\ \vdots & & [\mathbf{S}^E] & 0 \\ 0 & \ldots & 0 & [\mathbf{S}^E] \end{array} \right] .
\tag{6.4.8}
$$

The embedded quad-mode antenna element pattern is implemented in an array configuration using CST far-field array functionality and steered. The array is simulated and compared to the mathematically calculated array, in Figure 6.32. The simulated and mathematically implemented array results compare well.

The isolated quad-mode antenna element array is mathematically calculated using the same procedure as discussed above. The gain of the isolated quad-mode antenna element array is obtained through Equation (6.4.6). The isolated quad-mode antenna element has a different scattering matrix which is extracted from CST and the isolated array radiated power is obtained. The results are depicted in Figure 6.33 where the mathematically implemented isolated element array is compared with CST's far-field array function. It can be concluded from the results that CST's far-field array function significantly rescales the array pattern multiplication property due to the strong mutual coupling effects that result between each element.

Figure 6.35 compares the three mathematically implemented quad-mode antenna arrays and the embedded element pattern proves to be a more accurate approximation of the actual quad-mode antenna array.

The simulated CST's far-field array for the isolated, embedded element patterns with the mathematically obtained quad-mode antenna array gain patterns are plotted in MATLAB and compared in Figure 6.34. The results show that the embedded element pattern array has lower gain values and is therefore a closer approximation to the actual element array. It is clear from the obtained results that the embedded element pattern gives a better approximation of an array configuration, therefore it is used in the beamforming strategies and optimization techniques. It is important to note that the embedded element pattern is the pattern of an antenna simulated in an infinite array scenario, therefore only an approximation of the actual array configuration can be obtained.
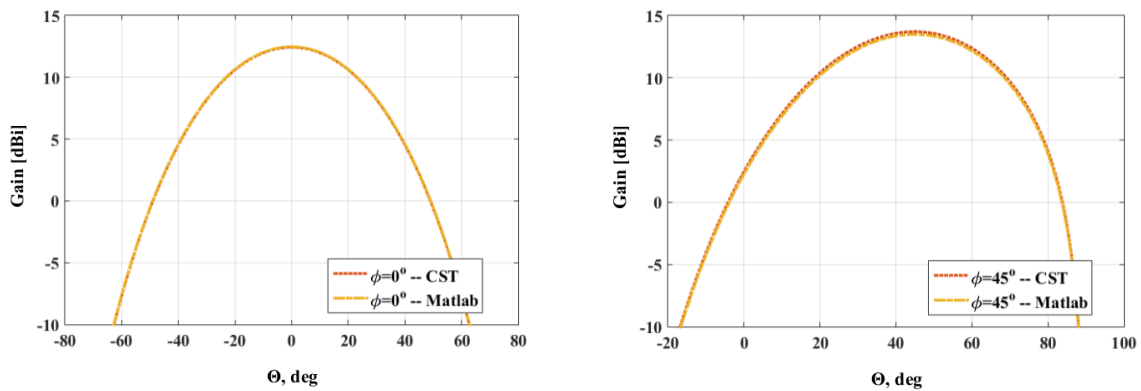
(a) Gain pattern steered broadside $\theta = 0°$.   (b) Gain pattern steered to $\theta = 45°$, $\phi = 45°$.

Figure 6.32: The gain pattern of the mathematically steered embedded element pattern compared with CST's far-field antenna array using the embedded element.
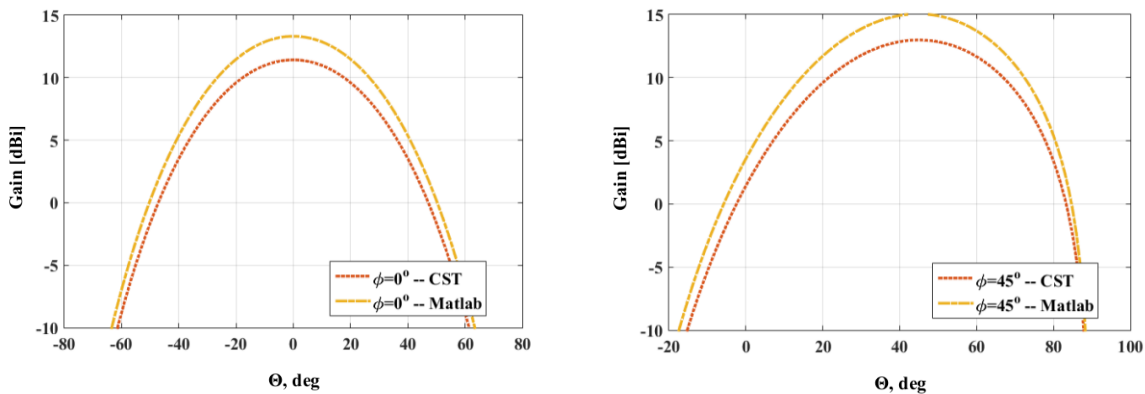
(a) Gain pattern steered broadside $\theta = 0°$.   (b) Gain pattern steered to $\theta = 45°$, $\phi = 45°$.

Figure 6.33: The gain pattern of the mathematically steered isolated element pattern compared with CST's far-field antenna array using the isolated element pattern.

(a) Gain pattern steered broadside $\theta = 0°$.   (b) Gain pattern steered to $\theta = 45°$, $\phi = 45°$.

Figure 6.34: Gain pattern of the actual quad-mode antenna array compared with the steered embedded and isolated element pattern from CST.
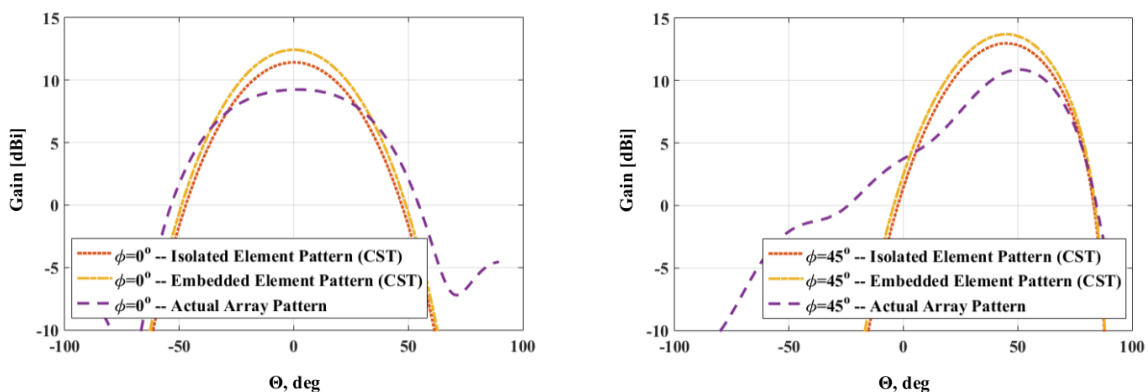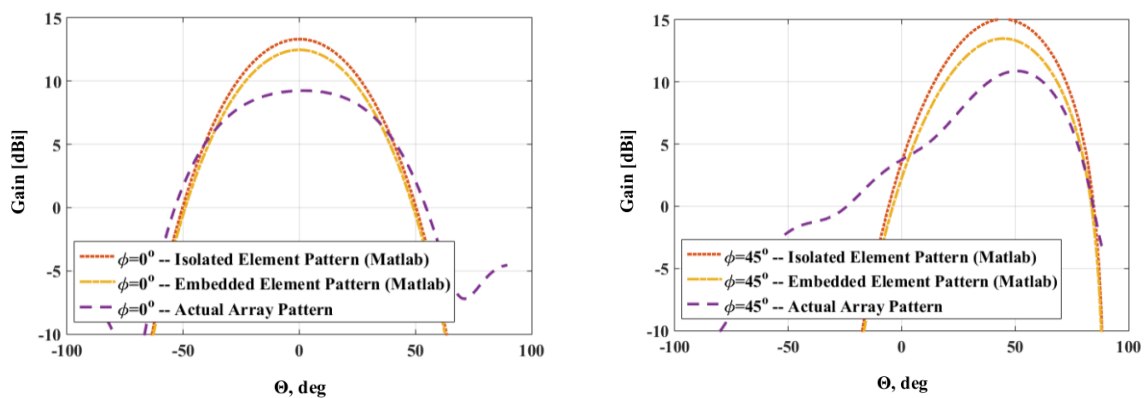
(a) Gain pattern steered broadside $\theta = 0°$. (b) Gain pattern steered to $\theta = 45°$, $\phi = 45°$.

Figure 6.35: Gain pattern of the actual quad-mode antenna array compared with the steered in MATLAB using the embedded and isolated element pattern.

6.5 Conclusion

In this chapter two separate planar arrays were designed and optimized for a maximum gain over a hemispheric FoV coverage. A 2×2 quarter-wavelength monopole array and a 2×2 quad-mode antenna array were implemented and the complex weighting vector to steer the array's beam pattern was established. This was done through optimization techniques and the maximum-gain beamforming theorem.

The monopole array was implemented for investigative purposes and the results confirmed that the proposed method was efficient and valid for synthesizing a quad-mode antenna array configuration for further research.

Throughout this chapter various multi-mode excitations sets and antenna excitation sets were investigated, compared, and the results were verified with the CST full wave far-field array simulation. Each solved and optimized set of multi-mode excitations was implemented in a planar array configuration and the beam pattern steered to maximum at each scanned angle over the hemisphere.

It was shown that the sixteen fundamental multi-mode excitations of the quad-mode antenna array yield a maximum gain of 13.6 dBi. The results also depict a minimum gain of 11.3 dBi and an overall gain variation of less than 2.3 dBi. This validates it as the best set of derived complex multi-mode excitations.

This chapter concludes by confirming that an optimal set of multi-mode excitations was obtained that allows for a hemispheric beam pattern. Placed in a planar array configuration, this set of multi-mode excitations obtains a good overall gain performance for a wide FoV coverage. The equivalent single-ended network model was also illustrated.

Chapter 7

Conclusion

As discussed in the introduction, a FoV specification of 60° from zenith is required for the SKA aperture array antennas. This led to the investigation of exciting the multi-mode excitation set for the quad-mode antenna in an efficient manner that allowed for a hemi-spheric FoV coverage, when placed in an array configuration.

Different optimization techniques and beamforming strategies were addressed throughout this thesis. The theoretical groundwork required to investigate these concepts were discussed.

Various optimization techniques, such as the GA and the Nelder-Mead simplex algorithm were discussed. The GA was implemented for the optimization of the quad-mode antenna beam pattern along with the FMINSEARCH solver in a MATLAB program. The optimization toolboxes in MATLAB were implemented for the purpose of this research. These optimization techniques were used throughout this thesis to obtain a set of multi-mode excitation weights for the quad-mode antenna. This set of multi-mode excitation weights was configured into a 2×2 array and through optimal beamforming implementations a hemispheric FoV coverage was obtained.

By means of effectively exciting the quad-mode antenna multi-mode response a unique radiation pattern was realized. The multi-mode response of the quad-mode antenna was fully characterized using the generalized expressions, derived in [3], to solve the single-ended mode S-parameters and the set multi-mode excitation weights.

A corporate feed network was designed with the set of single-ended mode excitation weights used at the output ports. The feed network was initially designed and simulated in ADS Agilent. The feed network was integrated into the quad-mode antenna design and simulated in CST Microwave Studio at 2 GHz. The gain patterns of the single-ended mode excitation weights and the integrated feed network were compared in MATLAB.

A 2×2 quad-mode antenna array was designed and implemented in MATLAB. When the isolated quad-mode antenna was simulated in CST's far-field array for a planar array configuration, a rescaling of the array factor was observed through comparing the results to the theoretical implemented array. Thus the periodic boundary condition in CST was used and the embedded element pattern was obtained. Optimization techniques were implemented to optimize the multi-mode excitation weights in an array configuration. The array's beam pattern was steered to maximum gain over the hemisphere by using the complex conjugate beamforming weighting functions. The sets of multi-mode excitation weights were optimized for maximizing the worst case maximum gain angle. The results showed that the best set of multi-mode excitation weights was achieved, through the GA optimization technique, with an overall gain variation of 2.7 dBi. A 2×2 quad-mode antenna array was drawn in CST and the simulated array was compared with the isolated

and embedded element pattern, using the far-field array in CST. The results showed that when steering the array in the far-field array in CST, the embedded element pattern gives the response closest to the actual array.

Placing the quad-mode antenna in an array configuration will not only give an improved hemispheric pattern but the antenna will also serve as a cost-effective element, due to its feed network configuration.

Appendices

Appendix A

Appendix

A.1   Quarter-Wavelength Monopole Antenna

This antenna exhibits an omnidirectional pattern, as illustrated by the 3-D radiation pattern in Figure A.1, and is often used as a reference antenna. Using the Equation given
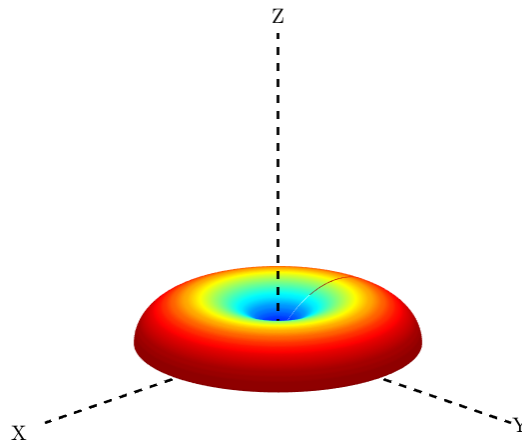

Figure A.1: The radiation pattern of a quarter-wavelength monopole antenna.

in (2.2.1) the electric far-field pattern of a quarter-wavelength monopole antenna is,

$$f^\theta(\theta, \phi) \simeq j\eta \frac{I_0 e^{-jkr}}{2\pi r} \left[\frac{\cos\left(\frac{\pi}{2}\cos\theta\right)}{\sin\theta} \right], \tag{A.1.1}$$

and the radiation intensity is,

$$U(\theta, \phi) = r^2 W_{av} \simeq \eta \frac{|I_0|^2}{8\pi^2} \sin^3\theta. \tag{A.1.2}$$

The total radiated power is obtained by integrating the radiation intensity over the entire hemisphere per solid angle $d\Omega$ of 4π. For an antenna isolated in free space and the wire of the antenna is defined to be much small than the length of the antenna then the radiation resistance for a quarter-wavelength monopole is $R_r = 36.5$. The total radiated power given in Equation (2.2.4) is used here for a quarter-wavelength monopole antenna and

is $P_{rad} = R_r/2 = 18.25$. The loss factor that accounts for the reflection mismatches of a quarter-wavelength monopole antenna is $e_r = 0.965$. The maximum realized gain is calculated from Equation (2.2.15) and obtained here at $\theta = 90°$ as,

$$\mathbf{G} = 4\pi \frac{U}{P_{rad}}. \tag{A.1.3}$$

List of References

[1] (2011) Lofar sweden. [Online]. Available: http://lofar-se.org/?page_id=49

[2] D. S. Prinsloo, P. Meyer, R. Maaskant, and M. V. Ivashina, "Irregular quad-mode antenna array: Field-of-view comparison with the swedish lofar station," in *2015 9th European Conference on Antennas and Propagation (EuCAP)*, May 2015, pp. 1–5.

[3] P. Meyer and D. S. Prinsloo, "Generalized multimode scattering parameter and antenna far-field conversions," *IEEE Transactions on Antennas and Propagation*, vol. 63, no. 11, pp. 4818–4826, Nov 2015.

[4] D. M. Pozar, *Microwave engineering; 4th ed.* Hoboken, NJ: Wiley, 2005. [Online]. Available: https://cds.cern.ch/record/882338

[5] D. S. Prinsloo, P. Meyer, M. V. Ivashina, and R. Maaskant, "A quad-mode antenna for accurate polarimetric measurements over an ultra-wide field-of-view," in *The 8th European Conference on Antennas and Propagation (EuCAP 2014)*, April 2014, pp. 3260–3263.

[6] M. V. Ivashina, O. Iupikov, R. Maaskant, W. A. van Cappellen, and T. Oosterloo, "An optimal beamforming strategy for wide-field surveys with phased-array-fed reflector antennas." in *IEEE Transactions on Antennas and Propagation*, vol. 59, no. 6, December 2010, pp. 1864–1875.

[7] C. A. Balanis, *Antenna Theory: Analysis and Design, 3rd Edition*, 3rd ed. Wiley-Interscience, Apr. 2005.

[8] "Standard definitions of terms for antennas," *IEEE Std 145-1993*, pp. 1–32, July 1993.

[9] D. M. Pozar, "The active element pattern," *IEEE Transactions on Antennas and Propagation*, vol. 42, no. 8, pp. 1176–1178, Aug 1994.

[10] A. Huynh, M. Karlsson, and S. Gong, *Mixed-Mode S-Parameters and Conversion Techniques.* INTECH Open Access Publisher, 2010. [Online]. Available: https://books.google.co.za/books?id=3F3-oAEACAAJ

[11] D. Bockelman and W. Eisenstadt, "Combined differential and common-mode scattering parameters: theory and simulation," *IEEE Transactions on Microwave Theory and Techniques*, vol. 43, no. 7, pp. 1530 – 1539, 1995. [Online]. Available: http://ieeexplore.ieee.org/search/srchabstract.jsp?tp=&arnumber=392911

[12] K. Vaz and M. Caggiano, "Measurement technique for the extraction of differential s-parameters from single-ended s-parameters," in *27th International Spring Seminar on*

Electronics Technology: Meeting the Challenges of Electronics Technology Progress, 2004., vol. 2, May 2004, pp. 313–317 vol.2.

[13] A. Bhattacharyya, *Phased Array Antennas: Floquet Analysis, Synthesis, BFNs and Active Array Systems*, ser. Wiley Series in Microwave and Optical Engineering. Wiley, 2006. [Online]. Available: https://books.google.co.za/books?id=nHKsLie6vN0C

[14] D. Cheng and F. Tseng, "Gain optimization for arbitrary antenna arrays," *IEEE Transactions on Antennas and Propagation*, vol. 13, no. 6, pp. 973–974, November 1965.

[15] R. Malhotra, N. Singh, and Y. Singh, "Genetic algorithms: Concepts, design for optimization of process controllers," *Computer and Information Science*, vol. 4, no. 2, p. 39, 2011.

[16] C. R. Houck, J. Joines, and M. G. Kay, "A genetic algorithm for function optimization: a matlab implementation," *NCSU-IE TR*, vol. 95, no. 09, 1995.

[17] Z. Michalewicz, "Gas: What are they?" in *Genetic algorithms+ data structures= evolution programs*. Springer, 1994, pp. 13–30.

[18] F. Herrera, M. Lozano, and J. Verdegay, "Tackling real-coded genetic algorithms: Operators and tools for behavioural analysis," *Artificial Intelligence Review*, vol. 12, no. 4, pp. 265–319, 1998. [Online]. Available: http://dx.doi.org/10.1023/A:1006504901164

[19] J. A. Nelder and R. Mead, "A simplex method for function minimization," *The computer journal*, vol. 7, no. 4, pp. 308–313, 1965.

[20] J. C. Lagarias, J. A. Reeds, M. H. Wright, and P. E. Wright, "Convergence properties of the nelder-mead simplex method in low dimensions," *SIAM Journal of Optimization*, vol. 9, pp. 112–147, 1998.

[21] C. Kilgus, "Multielement, fractional turn helices," *IEEE Transactions on Antennas and Propagation*, vol. 16, no. 4, pp. 499–500, Jul 1968.

[22] K. Kurokawa, "Power waves and the scattering matrix," *IEEE Transactions on Microwave Theory and Techniques*, vol. 13, no. 2, pp. 194–202, Mar 1965.

[23] T. H. Kjeldsen, "John von neumann's conception of the minimax theorem: A journey through different mathematical contexts," 2001.